

HARDWARE-IN-THE-LOOP SIMULATIONS AND CONTROL
DESIGNS FOR A VERTICAL AXIS WIND TURBINE

by
Uğur Sancar

Submitted to the Graduate School of Engineering and Natural Sciences
in partial fulfillment of the requirements for the degree of
Master of Science

Sabanci University

August 2015

HARDWARE-IN-THE-LOOP SIMULATIONS AND CONTROL DESIGNS FOR
A VERTICAL AXIS WIND TURBINE

APPROVED BY:

Prof. Dr. Serhat Yeşilyurt
(Thesis Advisor)

Assoc. Prof. Dr. Ahmet Onat
(Thesis Co-advisor)

Assoc. Prof. Dr. Ayhan Bozkurt

Prof. Dr. ErKay Savaş

Assoc. Prof. Dr. Osman Kaan Erol

DATE OF APPROVAL:

© Uğur Sancar 2015
All Rights Reserved

HARDWARE-IN-THE-LOOP SIMULATIONS AND CONTROL DESIGNS FOR A VERTICAL AXIS WIND TURBINE

UĞUR SANCAR

Mechatronics Engineering, Master's Thesis, August 2015

Thesis Advisor: Prof. Dr. Serhat Yeşilyurt

Thesis Co-advisor: Assoc. Prof. Dr. Ahmet Onat

Keywords: Hardware in the loop, maximum power point tracking, vertical axis wind turbine, inertia emulation, control.

Abstract

Control designs play an important role in wind energy conversion systems to achieve high efficiency and performance. In this study, hardware-in-the-loop simulations (HILS) are carried out to design control algorithms for small vertical axis wind turbines (VAWT).

In the HILS, the wind torque is calculated from the power coefficient of an experimental VAWT and applied to a motor that drives the generator in the VAWT simulator, which mimics the dynamics of the real VAWT rotor. To deal with the disturbance torques in the VAWT simulator, a virtual plant was introduced to obtain an error between the speeds in HIL system and the plant. This error is used to generate a disturbance torque compensation signal by a proportional-integral (PI) controller. The VAWT simulator successfully mimics the dynamics of the VAWT under various wind speed conditions and provides a realistic framework for control designs.

A maximum-power-point-tracking (MPPT) and a proposed simple non-linear control are presented for the control of the VAWT. The control algorithms were tested in the HILS under step up-down, sinusoidal and realistic wind conditions. The output power results are compared with each other and the numerically estimated optimum values.

The effects of the permanent-magnet synchronous generator (PMSG) parameters on the system efficiency were investigated, and a performance comparison in numerical simulation was made between the present PMSG and two other generators available in the market.

DİKEY EKSENLİ BİR RÜZGAR TÜRBİNİ İÇİN DÖNGÜDE DONANIM SİMÜLASYONLARI VE KONTROL TASARIMLARI

UĞUR SANCAR

Mekatronik Mühendisliği, Yüksek Lisans Tezi, Ağustos 2015

Tez Danışmanı: Prof. Dr. Serhat Yeşilyurt

Tez Yardımcı-danışmanı: Doç. Dr. Ahmet Onat

Ahahtar kelimeler: Atalet momenti emülasyonu, dikey eksenli rüzgar türbini, döngüde donanım simülasyonları, kontrol, maksimum güç noktası takibi.

Özet

Rüzgar enerjisi dönüşümü sistemlerinde kontrol tasarımları yüksek performansa ve verimliliğe ulaşmada önemli bir rol oynar. Bu çalışmada, küçük ölçekli dikey eksenli rüzgar türbini için kontrol algoritmaları tasarlamak amacıyla döngüde donanım simülasyonları (DDS) icra edilmiştir.

DDSde, rüzgar torku deneysel bir dikey eksenli rüzgar türbininin güç katsayılarından hesaplanarak, gerçek dikey eksenli rüzgar türbini sisteminin dinamiklerini benzeten simülatöründeki jeneratörü süren motora uygulanmıştır. Simülatördeki parazit torkların üstesinden gelmek adına, gerçek sistemin hızındaki hatayı elde edebilmek için sanal bir sistem ortaya konulmuştur. Bu hata, bir oransal-integral denetleyici tarafından, parazit torkları kompanze sinyali oluşturmak için kullanılır. Dikey eksenli rüzgar türbini simülatörü, değişik rüzgar hızlarında başarılı bir şekilde gerçek türbinin dinamiklerini benzetiyor ve kontrol tasarımları için gerçekçi bir sistem sunuyor.

Rüzgar türbininin kontrolü için bir maksimum güç noktası izleyici ve önerilen basit bir lineer olmayan denetleyici ortaya konulmuştur. Kontrol algoritmaları DDSde değişken basamak, sinuzoidal ve gerçekçi rüzgar hızı koşulları altında test edilmiştir. Çıkış güçleri kendi aralarında ve sayısal olarak hesaplanan ideal durum değerleriyle karşılaştırılmıştır.

Sabit mıknatıslı senkron jeneratör (SMSJ) parametrelerinin sistemin verimliliği üzerindeki etkisi incelenmiş ve kullanılan SMSJ ile piyasada bulundan iki adet diğer jeneratörlerin parametreleri kullanılarak bir performans karşılaştırılması yapılmıştır.

Acknowledgements

I would like to express my gratitude to my advisor Prof. Dr. Serhat Yeşilyurt for his valuable guidance and support through my studies. I am honored to be granted the chance to work with and to learn from him towards this important milestone in my life. I sincerely thank my thesis co-advisor Assoc. Prof. Dr. Ahmet Onat, not for only his immense contributions to my thesis, but also for having guided me through my academic life by helping me focus on my goals and stay motivated.

Lastly, I would like to state my appreciation and best regards to my thesis jury members Assoc. Prof. Dr. Osman Kaan Erol, Assoc. Prof. Dr. Ayhan Bozkurt and Prof. Dr. Erkey Savaş for sparing their valuable time to evaluate my thesis and helping me to make it better with their precious feedbacks.

TABLE OF CONTENTS

Acknowledgements	v
List of Figures	xii
List of Tables	xiv
Nomenclature	xv
1 Introduction	1
1.1 Motivation and objective	4
1.1.1 Outline of the thesis	5
2 Background	7
2.1 Vertical axis wind turbine system	7
2.1.1 Operating regions	9
2.2 Hardware in the loop	10
2.2.1 HIL simulations for wind turbines	11
2.3 Control of wind turbines	13
3 Model	17
3.1 Vertical axis wind turbine	17
3.2 Electromechanical model: generator and rectifier	19
3.2.1 The simplified dc model	27
4 VAWT Simulator and HILS	29
4.1 VAWT simulator layout	29
4.2 HIL components	31
4.2.1 Hardware components	31
4.2.1.1 Computer	31
4.2.1.2 dSpace	32
4.2.1.3 Motor drive	32
4.2.1.4 Motor	32
4.2.1.5 Gearbox	32

4.2.1.6	Generator	33
4.2.1.7	ac/dc converter	33
4.2.1.8	Electronic load	33
4.2.2	Software programs	33
4.2.2.1	OPD explorer	33
4.2.2.2	dSpace software	34
4.2.3	Software implementation	34
4.2.3.1	Wind speed generator	34
4.2.3.2	VAWT model	35
4.2.3.3	Software - Hardware (SW - HW) interface	35
4.2.3.4	Write/Read motor	35
4.2.3.5	Control block	35
4.2.3.6	Write/Read E-load	35
4.3	Model validation and parameter identification	37
4.3.1	Number of pole pairs in PMSG	37
4.3.2	Equivalent moment of inertia estimation	38
4.3.3	Friction torque	40
4.3.4	PMSG and rectifier model parameters validation	40
4.3.4.1	Validation of non-ideal PMSG-rectifier model	42
4.3.4.2	Validation of simplified dc model	44
4.3.4.3	Torque constant of PMSG	45
4.4	Inertia emulation	47
4.4.1	VAWT dynamic equations	47
4.4.2	VAWT simulator dynamic equations	47
5	Control	52
5.1	Introduction	52
5.2	Control methods	55
5.2.1	Maximum power point tracking (MPPT)	56
5.2.2	Simple non-linear control	57
6	Results	60
6.1	Maximum power point tracking	60
6.1.1	Parametric study	61
6.1.2	HIL simulation results for MPPT	63
6.1.2.1	Step-response	64
6.1.2.2	Sinusoidal response	65
6.1.2.3	Response to realistic wind data	66
6.2	Simple nonlinear control	67
6.2.1	Parametric study	68

6.2.2	HIL simulation results for simple non-linear control	70
6.2.2.1	Step response	71
6.2.2.2	Sinusoidal response	72
6.2.2.3	Response to realistic wind data	73
6.3	Comparison of the control methods	74
6.4	Effects of the generator parameters on the performance	76
6.4.1	Ideal generator parameters	78
6.4.2	Performance comparison	80
7	Conclusion and future works	84

LIST OF FIGURES

1.1	Components of a wind energy conversion system.	1
1.2	Different rotor configurations for wind turbines.	2
1.3	Power coefficient C_p with respect to the TSR for different designs [5].	3
1.4	Block diagram of the studied system.	5
2.1	Swept area of the VAWT.	7
2.2	TSR, λ , - $C_p(\lambda)$ curve of the studied VAWT. The maximum value of the power coefficient, $C_{p,max}$, is obtained at optimum TSR, λ_{opt}	9
2.3	Actual wind turbine and emulated wind turbine generator system.	12
2.4	Principal control subsystems of a wind energy conversion system. [23]	13
2.5	Possible directions that can be determined in MPPT process.	15
3.1	Aerodynamic power with respect to rotor rotational speed for different wind speeds; 12,10,8 and 5 m/s.	18
3.2	Representation of an ideal PMSG-rectifier model that is connected to a DC current load.	20
3.3	Ac and dc waveforms of the ideal PMSG-rectifier model shown in 3.2	22
3.4	Ac waveforms of the idea PMSG model. Notice that v_{an} is divided by 5 in the plot for visual convenience.	23
3.5	Frequency spectrum of the phase current I_a that is given in 3.4.	24
3.6	Representation of a non-ideal PMSG-rectifier model that is connected to a DC current load.	26
3.7	ac and dc waveforms of PMSG-rectifier the non-ideal model shown in 3.6 and their frequency spectrum. The results of the ideal PMSG-rectifier model results are shown in the plots for comparison.	26
3.8	PMSG-rectifier and its simplified dc model. E_{LN} is electromotive force (EMF), L_s is phase inductance, R_s is the phase resistance of the PMSG, I_{dc} and V_{dc} are the average values of the dc current and voltage, respectively; E_{sdc} , L_{dc} , R_{dc} represents the correspondence values between the 3-phase ac model and the equivalent dc model.	28
4.1	(a) Representation of VAWT system in real world, (b) VAWT simulator.	30

4.2	VAWT simulator components: 1- Host PC, 2- dSpace connector panel, 3- motor drive, 4- PMSM, 5- Gearbox, 6- PMSG, 7- Programmable dc load.	31
4.3	General schema of the HIL simulation.	31
4.4	Input ratings and operating contour of electronic load Agilent N3306A. [48]	33
4.5	Main simulation file created in Simulink.	34
4.6	Character to ASCII transferred data.	36
4.7	Content of the Write/Read E-load subsystem.	36
4.8	Number of bytes output of the transmitter and receiver blocks are plotted with the pulse signal.	37
4.9	PMSG line voltage measurement under 31.83 rad/s mechanical speed.	38
4.10	Motor torque and angular position with respect to time.	39
4.11	Schematic of motor-gear box-generator drive train in VAWT simulator. $J_{m,motor}$ is the motor-shaft-only inertia, J_{gear} is the gear box equivalent inertia, J_{gen} is the generator inertia and Γ is the gear box ratio.	40
4.12	Friction torque with respect to motor speed.	41
4.13	Measured open circuit line voltage of PMSG under $\omega_{gen} = 31.83rad/s$.	42
4.14	line voltage and phase current of the model simulation (left) and Test 2.1 (right). The PMSG runs at $\omega_{gen} = 31.83 rad/s$ and 3 A is drawn by dc load.	43
4.15	Frequency spectrum of the signals that are plotted in Figure 4.14 . .	43
4.16	DC voltages with respect to the load current under different speed of PMSG. Solid lines represent the numerically calculated values by using DC equivalent model, the circles show the obtained test results and each color represents the correspondence working speed of the PMSG.	45
4.17	Estimated generator torque values with respect to the dc load current.	46
4.18	Block diagram of the VAWT dynamics, HIL System and reference motor torque calculation.	48
4.19	Model following controller with a PI based disturbance compensator structure in the HIL system.	49
4.20	Content of the SW-HW interface subsystem.	50
4.21	The contents of PI type, T_dist compensator block.	50
4.22	The comparison of HIL and numerical simulations rotational speed responses with 8 m/s step up and down speed. The initial speed of the VAWT rotor was set to 2 rad/s.	51

5.1	Wind power and resultant torque for 8 m/s wind speed at steady state. Left and right y-axis represent the wind power and torque respectively	53
5.2	Corresponding dc load current and voltage under 8 m/s wind speed at steady state. Left and right y-axis represent the dc load current and voltage respectively.	54
5.3	Wind power P_{wind} and electrical output power P_{dc} with respect to the rotor speed for 8 m/s wind speed.	54
5.4	Wind power P_{wind} and electrical output power P_{dc} with respect to the rotational speed for three different wind speeds. $P_{wind,opt}$ and $P_{dc,opt}$ are the functions of wind speed that gives the maximum value of the wind and electrical output power respectively.	55
5.5	The output power (P_{dc}) with respect to dc voltage for 6, 9, 11 m/s wind speeds in steady-state.	56
5.6	Flow chart of the MPPT algorithm.	57
6.1	Applied wind velocity profile for parametric study of the MPPT. First ten seconds the wind speed is 5 m/s, then it steps up to 8 m/s, 11 m/s and down to 6 m/s in every 30 seconds respectively.	61
6.2	Output power results of experiment mppt.6, 7 and 8. The power and the current values are depicted with respect to the time over a shorter time in bottom left and right plots respectively.	62
6.3	Applied wind velocity for testing the MPPT algorithm in HIL simulation.	63
6.4	HIL simulation results for the step up and down wind velocity.	65
6.5	HIL simulation results for the sinusoidal wind velocity.	66
6.6	HIL simulation results for the realistic wind velocity. Note that the wind velocity starts from 0 m/s.	67
6.7	The output power curves with respect to the dc load voltage.	68
6.8	Output power results of experiment snc 1,2, and 6.	69
6.9	Representative power curve illustration and simple non-linear control rule equation for explanation of the output power oscillations due to the estimated voltage and power with a margin of error ϵ	70
6.10	HIL simulation results for the step up and down wind velocity.	71
6.11	HIL simulation results for the sinusoidal wind velocity.	73
6.12	HIL simulation results for the realistic wind velocity. Note that the wind velocity starts from 0 m/s.	74

6.13	Comparison of the MPPT and simple non-linear control (snc) results. The output power the step, sinusoidal and realistic wind profile are at the left-hand side from top to bottom respectively. The corresponding energy outputs are at the right side of each plot.	75
6.14	Simplified dc model with neglected phase inductance in generator, diode overlapping currents and threshold voltage in rectifier. Only the phase resistance is included.	76
6.15	The wind power and torque, dc power and current of the VAWT system with only R_{dc} regarded dc model for 8 m/s wind speed. The left hand side plots represent the wind power (P_{wind}), output power under normal condition (P_{dc}) and when the back-emf constant is doubled ($P_{dc,2}$).The right hand side plots represent the wind torque (P_{win}), dc current under normal condition (I_{dc}) and when the back-emf constant is doubled ($I_{dc,2}$).	77
6.16	The wind power (P_{wind}), output power under normal condition (P_{dc}) and when the back-emf constant is doubled ($P_{dc,2}$).	77
6.17	Average losses and losses at the rated power are at the left and right hand sides of the figure respectively. The solid lines represent the total losses, the dashed lines represents the iron losses and the dotted lines represents the copper losses [59].	79
6.18	4-pole PM machine (left) and 20-pole PM machine (right) [60]	80
6.19	The wind power and torque, dc power and current of the VAWT system with the parameters of present, Alxion-1 and Alxion-2 generators. 82	82

LIST OF TABLES

3.1	The studied VAWT parameters.	17
3.2	The coefficient values used in C_p model.	18
3.3	Operating regions, maximum available aerodynamic power ($P_{wind,max}$) at rotor speed (ω_r) with torque (T_{wind}) values for wind speeds from 3 to 12 m/s.	19
3.4	PMSG and simplified dc model variables.	28
4.1	Femsan 5F100810001 motor parameters.	32
4.2	Validation test numbers and their contents for non-ideal PMSG-rectifier model	42
4.3	Line voltage and phase current THD% results of experiment and sim- ulation. To calculate the deviations, experimental results are selected as base point.	44
4.4	Obtained dc load voltage from the real PMSG-rectifier, non-ideal PMSG-rectifier simulation model and numerical model. Deviation % column shows the percentage deviations of numerically calculated voltage to experimentally measured ones.	44
4.5	Estimated and measured parameters of the PMSG and rectifier. . . .	46
4.6	Parameters of the PI-controller that is used to generate the distur- bance torque compensator.	51
6.1	Influence of the control unit sampling time and current step size to energy output in HIL simulation in which mppt control unit operates.	61
6.2	Applied wind velocity values and durations for the MPPT algorithm testing in the HIL simulation.	64
6.3	Influences of the minimum and maximum voltage threshold values in simple non-linear control to the total energy obtained.	68
6.4	The total obtained energy output for step up and down, sinusoidal and realistic wind profile.	75
6.5	Varied parameters of 6 different generator design [59]	79
6.6	Alxion generator, 145STK2M parameters [66].	81

6.7 Transformed Alxion parameters and present generator parameters
that are used in the simplified dc model for performance compari-
son. (For transformation details, see Table 4.5 and 3.4). 81

Nomenclature

Acronym	Description
WECS	Wind energy conversion system
HIL	Hardware-in-the loop
HILS	Hardware-in-the loop simulations
VAWT	Vertical axis wind turbine
HAWT	Horizontal axis wind turbine
PMSM	Permanent magnet synchronous motor
PMSG	Permanent magnet synchronous generator
RMS	Root-mean-square
MPPT	Maximum power point tracking
LPF	Low pass filter
DO	Disturbance observer

Subscripts	Description
dc	Direct current
ac	Alternative current
LL	Line-to-line
LN	Line-to-neutral
opt	Optimum
ref	Reference
max	Maximum
min	Minimum

Symbol	Description	Unit
A_{swept}	Swept area of wind turbine	m^2
B	Friction coefficient	Nm/rad
C_p	The coefficient of wind turbine aerodynamic power	—
e	error	—
$e_a(t)$	Instantaneous line back-emf voltage in phase a	V
$e_b(t)$	Instantaneous line back-emf voltage in phase b	V
$e_c(t)$	Instantaneous line back-emf voltage in phase c	V
E_{LN}	RMS back-emf voltage	V
f_e	The electrical frequency of generator	Hz
I_{dc}	dc current	A
I_{dis}	Distortion components of RMS phase current	A
I_L	The RMS value of the phase current	A
I_{L1}	The RMS value of the phase current fundamental component	A
I_{Lh}	harmonic component at the h harmonic frequency	A
i_{dis}	Distortion components of instantaneous phase current	A
$i_a(t)$	instantaneous current of the phase a	A
$i_b(t)$	instantaneous current of the phase b	A
$i_b(t)$	instantaneous current of the phase b	A
$i_L(t)$	instantaneous phase current	A
$i_{L1}(t)$	The fundamental component of the phase current	A
$i_{Lh}(t)$	harmonic component at the h harmonic frequency	A
J_{gen}	Generator inertia	kgm^2
$J_{m,rotor}$	Motor inertia	kgm^2
J_m	The equivalent inertia at the motor shaft	kgm^2
J_r	Equivalent wind turbine rotor inertia	kgm^2
K_e	back-emf constant	—
K_i	Integral gain	—
K_p	Proportional gain	—
K_T	Torque constant	Nm/A
K_t	Torque constant for simplified dc model	Nm/A

Symbol	Description	Unit
L	The length of blade	m
L_s	Phase nductance	H
p	Number of pole pairs	—
P_{ac}	Active power	W
pf	Power factor	—
Q_m	The rotor position of th motor	rad
R	The radius of VAWT	m
R_s	Phase resistance	Ω
S_{ac}	Apparent power	VA
T_{gen}	Generator torque	Nm
T_{hf}	Friction torque in the HIL simulation system	Nm
T_{rf}	Friction torque at wind turbine rotor	Nm
T_{wind}	Wind torque on wind turbine rotor	Nm
T_m	Motor torque	Nm
THD	Total harmonic distortions	—
U_{wind}	Wind speed	m/s
$v_a(t)$	The instantaneous voltage of phase-a	V
$v_b(t)$	The instantaneous voltage of phase-b	V
$v_c(t)$	The instantaneous voltage of phase-c	V
V_{dc}	dc voltage	V
V_{LL}	RMS line voltage	V
V_{LN}	RMS phase voltage	V
V_{th}	The on-stage voltage of diode	V
Γ	Gear box ratio	—
λ	Tip speed ratio	—
ω_{rotor}	Wind turbine angular rotor speed	rad/s
ω_e	Generator electrical angular frequency	rad/s
ω_{gen}	The mechanical angular speed of generator	rad/s
ϕ_s	flux	Vs/rad
ρ	Air density	kg/m^{-3}

Chapter 1

Introduction

Renewable energy systems are very popular due to increasing energy demand in the developing world, the climate-change threat and diminishing reserves of fossil fuels. Among the renewable energy sources, the wind energy technology is one of the most promising technologies.

The history of use of wind power dates back to 5000 years ago for sailing ships. More recently, in the 1700s and 1800s, wind power was used to grind grains and pump water in Europe. According to [1], the first wind turbine was developed by Charles Brush in Cleveland, Ohio in 1888 for the purpose of the electric generation. On the other hand, according to [2], the first systematic development to utilise wind power for electric generation took place in Denmark in 1891 by professor Poul La Cour, who was encouraged by the Danish government to search for ways of supplying electricity in rural areas. Today, large wind turbines are routinely installed and the wind turbine industry is growing. From 1980s to now, the decreasing cost of wind-generated electricity, which is now less than 3-4 cents/kWh, makes wind energy the least expensive renewable source and competitive with coal, and natural gas-fired plants, [3], [4].

A state-of-art of the wind energy conversion system (WECS) is illustrated in Figure 1.1. The wind energy conversion system converts the kinetic energy of the wind

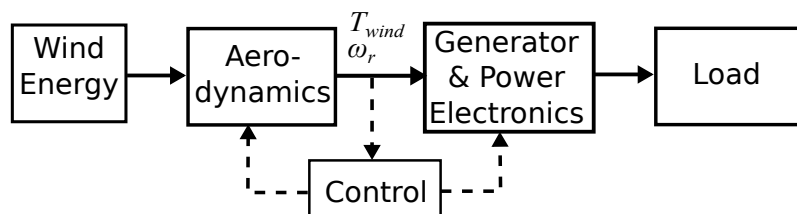


Figure 1.1: Components of a wind energy conversion system.

into mechanical energy by wind turbine aerodynamics, and the mechanical power which is the product of torque, T_{wind} , and angular rotor speed, ω_r , is transmitted by the drive-train to the generator where the energy is converted into the electricity.

The drive-train may include a gearbox, or the generator is directly driven by the rotor shaft. The control unit adjusts the operating point of load or aerodynamics such that aerodynamic components operates at maximum efficiency; it is important for the safety of the system as well.

With respect to the axis of rotation, two distinctly different configurations exist; the horizontal-axis wind turbines (HAWT) and the vertical-axis wind turbines (VAWT). Widespread use of the wind energy is enabled in part by the horizontal axis wind turbines even though they were invented later than vertical axis wind turbines. Some examples of VAWTs and a HAWT are shown in Figure 1.2 [2].

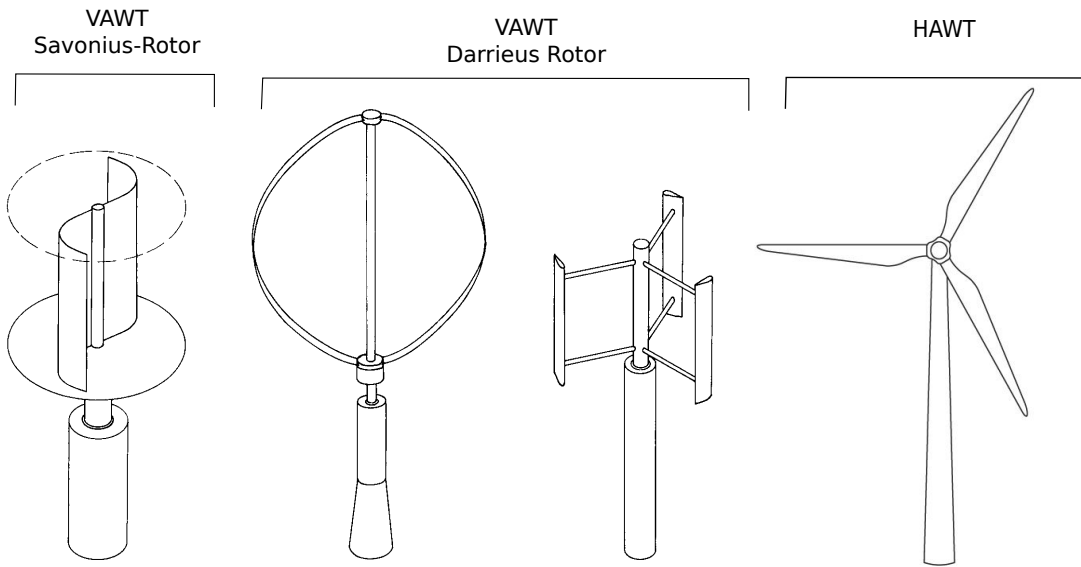


Figure 1.2: Different rotor configurations for wind turbines.

Wind turbine power production depends on the interaction between the rotor and the wind speed. The power extracted by the blades can be calculated by Equation 1.1 as commonly expressed in literature [1], [2], [4].

$$P_{wind} = \frac{1}{2} C_p \rho A_{swept} U_{wind}^3 \quad [W] \quad (1.1)$$

where ρ is air density, A_{swept} is swept area of the turbine and U_{wind} is wind speed. The portion of the wind energy that is converted into the kinetic energy of the rotor can be characterized with the power coefficient C_p , which, in essence, represents the "aerodynamic efficiency" of the turbine. The C_p depends on the angular velocity of the rotor and the wind velocity, and it is often expressed as a function of the tip-speed-ratio (TSR) which is defined as the ratio of the rotor's out-most tip speed to the upstream wind speed. The characteristic of the C_p is affected by many parameters, such as the aerodynamic design, number of rotor blades and more [2].

In Figure 1.3, various rotor configurations and their C_p curves are depicted.

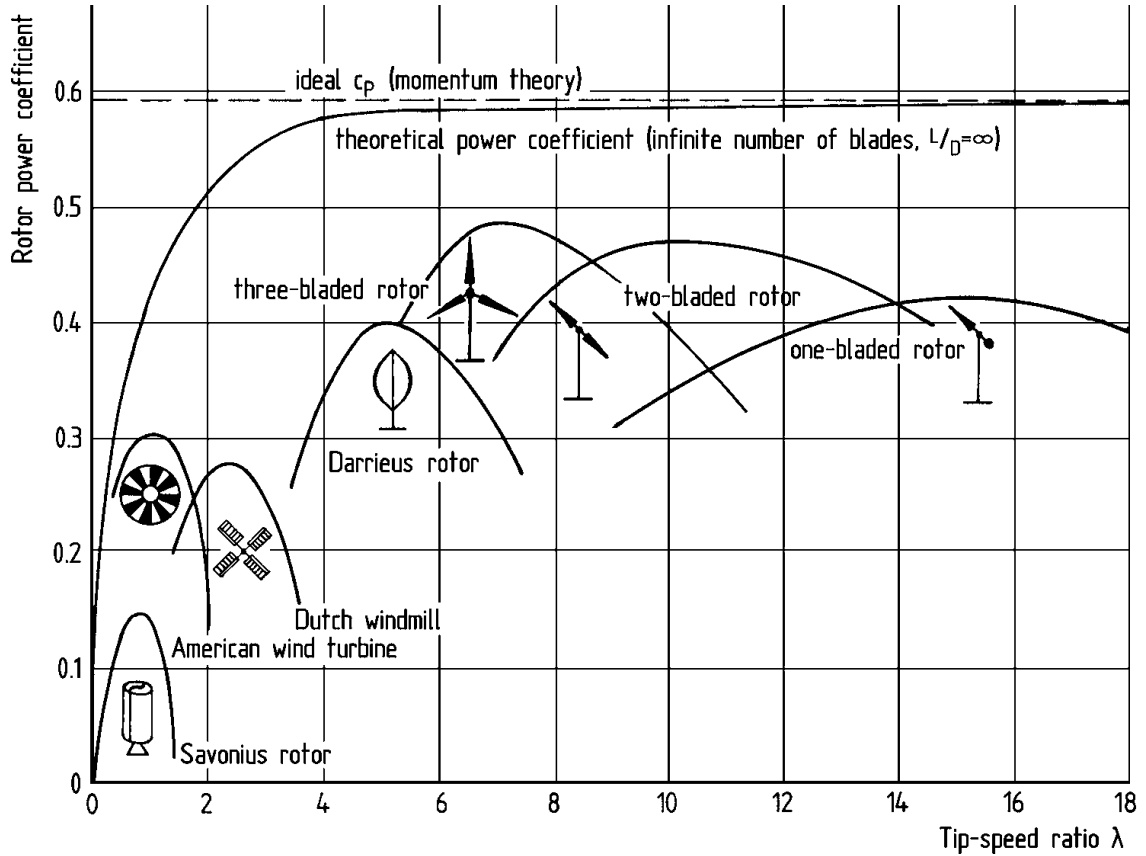


Figure 1.3: Power coefficient C_p with respect to the TSR for different designs [5].

For a particular wind velocity, the turbine should be driven at the optimal rotor speed to obtain optimal C_p or aerodynamic configuration. The wind power system is controlled to match the rotor speed to generate power equal to, or as close as possible to the maximum power, $P_{wind,max}$. The maximum C_p of HAWT designs is around 0.5, and this is one of the reasons that HAWTs represent the overwhelming majority of WECS used today.

In terms of operation speed, WECS can be classified as fixed speed and variable speed. For fixed-speed WECS, the wind turbine rotor speed is governed, regardless of the wind speed, by the grid frequency since the generator is directly connected to the grid. This type of WECS has a simple and inexpensive electrical system because they do not require a frequency conversion system. On the other hand, fixed speed operation can not capture the highest possible energy from the wind under various wind speed conditions. However, the variable-speed WECS is able to maintain the optimal TSR value in which the maximum available power occurs. Thereby, the variable-speed WECS are most used in today's WECS where the variable speed operation is actualized by incorporation of power electronics interface and pitch control. In WECS, fluctuations in wind speed are transmitted into mechanical

torque and it causes electrical fluctuations at generator output, but decoupling the generator prevents this electrical fluctuation effect into grid in variable-speed WECS thanks to power electronics converters.

Power generation wise, the current status of wind power utilization is divided into two categories; grid-connected wind power generation and standalone systems. Most of the present wind power plants, which are grid connected systems, employ HAWTs because of their higher efficiencies under certain wind conditions. On the other hand, VAWTs can outperform HAWTs in severe wind climates with high turbulence, fluctuations, and high directional variations. For example, they are omni-directional and have a vertical shaft which makes the structure much simpler by allowing the installation of the generator and other related system components on the ground, instead of locating them at the top of the tower. Moreover, VAWTs are slower and generate lower levels of noise than HAWTs; therefore, a small-scale VAWT can be installed in urban areas as a standalone system, e.g. on a mast or top of a building, where it would be advantageous over a HAWT due to the wind characteristics, [6], [4], [7].

Consequently, there is a remarkable potential for improving different aspects of the VAWTs as an alternative renewable source for rural areas and micro grids. Moreover, the electrical power conversion and control is at the core of how a wind turbine performs, operates and interacts with the load, hence there is a need to explore VAWTs operation and control. Numerical simulations are one way for testing the performance of power electronic components and control designs in controlled experiments under realistic conditions. However, hardware-in-the-loop (HIL) simulations have numerous advantages over numerical-only simulations. They allow controlled experiments with actual power electronic components. Moreover, the effects of electrical and mechanical limitations, sensor accuracy, the sampling period of control unit, thermal effects and other disturbances are observed directly in HIL simulations.

1.1 Motivation and objective

In this thesis, a VAWT model is studied as a portable generator that satisfies the need of electrical energy in rural areas and standalone systems. A block diagram of the system is presented in Figure 1.4. Previously, a VAWT has been designed and manufactured in mechatronics department of Sabanci University under the project name " *A prototype development for portable power generation with vertical axis wind turbines (VAWT) for communication towers.*" Consequently, this work aims to develop a framework for testing the electromechanical and power electronics components of the VAWT system, and evaluating the control algorithms. The modelled

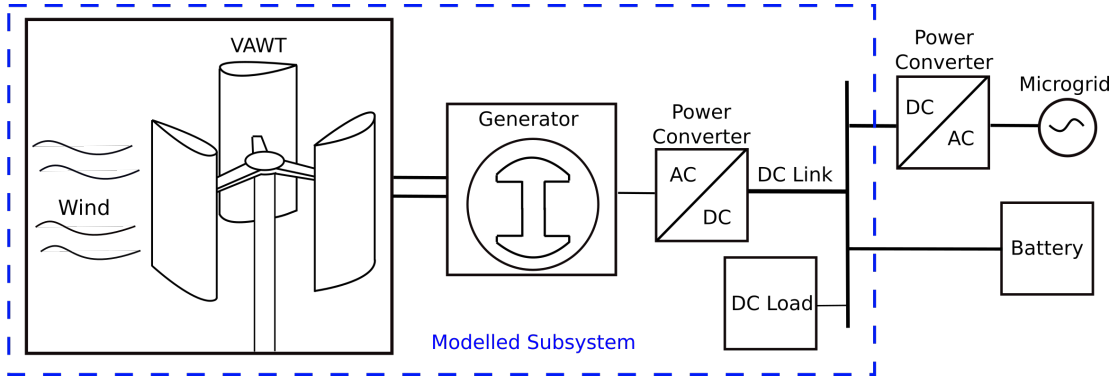


Figure 1.4: Block diagram of the studied system.

subsystem is specified by the blue dashed lines in Figure 1.4. The mechanical power output of the aerodynamic components were simulated and fed to the physically implemented generator, power converter and dc load by a motor that was used as an actuator representing the mechanical power source in VAWT simulator.

The VAWT allows variable speed without a blade pitch mechanism as commonly observed in large scale wind turbines. Instead, a power electronics converter adjusts the load for the wind variation, hence higher power output is obtained. The load control strategies can be implemented in the VAWT simulator to evaluate their performances. Several control algorithms have been described in literature [4]. Since our purpose is to control our low cost VAWT system, the control unit should be simple and has low cost too.

In order to ensure the fidelity of the VAWT simulator, its static and dynamic characteristics must be the same as the characteristics of the real system. Above mentioned objective of this thesis seeks answer to the questions below:

- How to develop a VAWT simulator that mimics the actual system accurately?
- How to mimic the dynamics of the VAWT in the HIL simulator?
- How to operate the system at its maximum power point by implementing a simple and low cost control algorithm which is at least competitive with the ones that are used in literature?
- What are the effects of the generator parameters on the performance, and what kind of generator is ideal for the VAWT system?

1.1.1 Outline of the thesis

The rest of the thesis is organized as follows:

- Chapter 2 gives a brief background information on VAWTs, hardware in the loop simulations and control of wind turbines.

- In Chapter 3, a model of the VAWT, electromechanical model containing the generator and 3-phase diode-rectifier and its simplified dc equivalent model are presented.
- In Chapter 4, the VAWT simulator, its components and features are presented. Following, the software implementation and simulation blocks are introduced. Furthermore, the generator parameter identification and simplified dc model validation are also presented in this chapter. Lastly, the proposed inertia emulation method is explained.
- Chapter 5 describes control methods applied in the HIL simulation. The estimation of the optimal dc output power, which attains different values than the aerodynamic power, calculations are also presented here.
- Chapter 6 is consists of the HIL simulation results for the step up-down, sinusoidal and realistic wind profiles. Before the presentation of the results, the parametric studies which are carried out for tuning the controller parameters and their results are presented. Furthermore, performances of both methods are compared. Then, the effects of the generator parameters on the performance is discussed, and the ideal generator parameters are covered. Lastly, by using the simplified dc model, a numerical calculation based performance comparison are done between the VAWT systems with the present generator and two other generators found from the market.
- In Chapter 7, the conclusion and future works proposal are presented.

Chapter 2

Background

This chapter presents, an overview of the aerodynamics of the VAWT in Section 2.1. Types of generators, direct-drive topology and working ranges of VAWT system are also covered in Section 2.1. Furthermore, in Sections 2.2 and 2.3, hardware-in-the-loop simulators and the control strategies of the wind turbines are reviewed.

2.1 Vertical axis wind turbine system

The maximum available power from the wind is subject to Betz Limit, that is equal to $16/27$ [1]. This Betz Limit is the maximum theoretical value of the power coefficient C_p which is used in Equation 1.1.

The swept area, A_{swept} , for the VAWT given in Figure 2.1 is calculated from Equation 2.1.

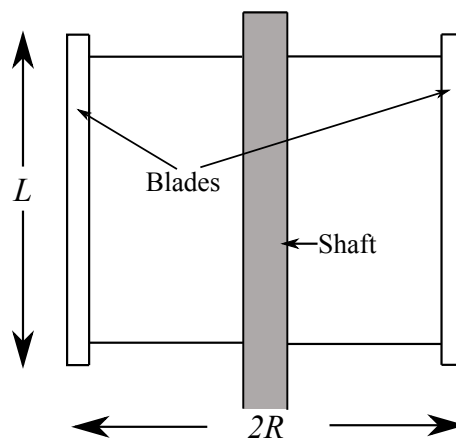


Figure 2.1: Swept area of the VAWT.

$$A_{swept} = 2RL \quad [m^2] \quad (2.1)$$

Hereby, the available wind power of a VAWT of radius R and length L is given by

Equation 2.2

$$P_{wind} = C_p(\lambda)\rho LRU_{wind}^3 \quad [W] \quad (2.2)$$

where ρ is air density, U_{wind} is wind speed, $C_p(\lambda)$ is power coefficient, which is a function of the tip speed ratio, λ , that is given by Equation 2.3.

$$\lambda = \frac{\omega_r R}{U_{wind}} \quad [-] \quad (2.3)$$

where ω_r is rotor angular velocity. In this study, a $\lambda - C_p(\lambda)$ curve that is obtained from computational fluid dynamics simulations is employed and the curve is given in Figure 2.2.

In the VAWT system, the aerodynamic power is transferred through the VAWT rotor to generator rotor by the drive train. In other words, the drive train realizes the mechanical power transmission. Besides, it can be responsible of matching the speed level of the VAWT rotor to generator. VAWTs operate at tens of radians per second, while conventional generators are most commonly designed for high rated speeds. In many applications, step-up gearboxes are used to transfer the mechanical energy from low speed to high speed, i.e generator rated speed range. However, implementation of a gearbox in the drive train causes noise and mechanical losses. Moreover, it introduces additional cost and requires maintenance. On the other hand, direct drive (gear-less)generators are more preferred especially for stand-alone VAWT used in urban or rural areas. The main disadvantage of the direct-drive VAWT is the need for a generator that is designed for low-speed and high-torque applications unlike conventional generators. Since the machine size and power losses depend on the rated torque, low-speed and high-torque generators are substantially heavy and less efficient. Yet, these deficiencies can be overcome by designing the generator for direct drive application, i.e with a large diameter and small pole pitch [4].

The transmitted mechanical power through the drive train is converted into electrical power by an alternating current (ac) generator or a direct current (dc) generator. dc generators are not widely used for wind turbine applications due to high maintenance requirement of brushes and the commutator. WECSs recently employ ac and brushless generators, which include induction (asynchronous) generators and synchronous generators. Theoretically, all ac machine stators could have the same three-phase windings while their rotors have to be different. For synchronous machines, the magnetic flux can be supplied by an external excitation dc current given to rotor windings or by permanent magnets on the rotor. For induction machines, voltage is induced in the rotor windings (short-circuited bars) and current flows

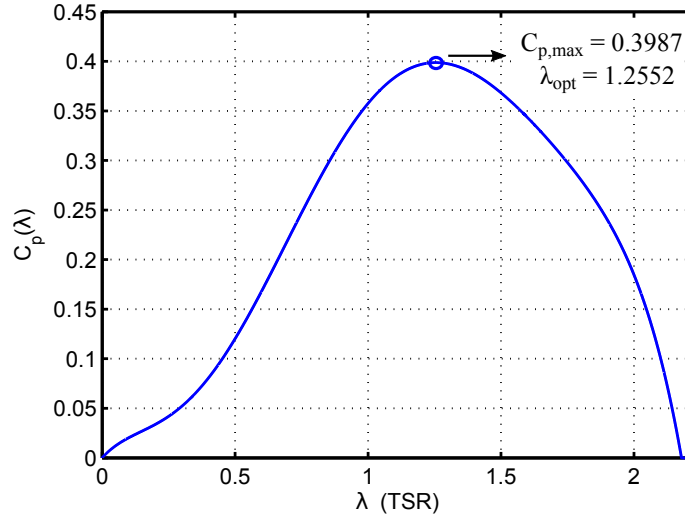


Figure 2.2: TSR, λ , - $C_p(\lambda)$ curve of the studied VAWT. The maximum value of the power coefficient, $C_{p,max}$, is obtained at optimum TSR, λ_{opt} .

in the rotor. Electromagnetically interacted rotor current and flux produce torque on the rotor or vice versa. Induction generators are the work horses of industry as they are commonly used for constant speed application because the rotor speed depends on the electrical load. Furthermore, the induction generators consume reactive power which causes the power factor to be less than the unity especially in small power scale induction machines. For variable-speed VAWT applications, permanent magnet synchronous machines (PMSGs) are preferred since the magnetizing current is not part of the external current, and they have wide range of operational speed which is independent of the load. Furthermore, their power factors are close to unity and efficiencies are higher than dc and induction generators; i.e the closer the power factor converges to unity, the more active power can be delivered. Moreover, PMSGs have the highest torque density compared to the externally exciting synchronous, induction and DC generators. On the other hand, PMSGs have high cost and magnets can be partially or completely demagnetized under high temperature. In this study, a permanent magnet synchronous generator (PMSG) is used.

2.1.1 Operating regions

In general, the operation characteristics of wind turbines can be divided into 4 regions.

- Region 1 is where the wind speed is less than cut-in speed. Until the cut-in speed, the captured power is not sufficient to compensate losses, and consequently generate a sufficient power. Thereby, the turbine is parked in this region.
- Region 2 is where the wind speed is higher than cut-in speed but less than the

rated speed. In this region, main objective is to keep the operating point of the WECS at its maximum power point.

- Region 3 is where the wind speed is higher than the rated speed but lower than the cut-out speed. For the sake of safety, the speed or torque can be limited. In cases the speed and torque values are not so high that they pose a safety threat, the objective can also be keeping the operating point of the WECS at its maximum power point in small scale wind turbines.
- Region 4 is where the wind speed is above the cut-out wind speed. It is not possible to safely operate the wind turbine due to mechanical restrictions.

2.2 Hardware in the loop

HILS are commonly used in vehicle development, however their first use documented for flight simulations in 1936 [9]. Especially the actuators in the vehicle system, suspensions and bodies are tested and developed with the help of HILS [9]. After the development of vehicle traction and braking systems and development of digital control, HILS gain further role in the vehicle technology [10] where the actuators and environmental effects are hard to incorporate in a numerical model [9]. Another area where HILS are widely used is the missile guidance methods [11, 12]. Furthermore, high fidelity HILS are also used in space technology, for example in [13], NASA developed a HILS for a remotely piloted highly maneuverable aircraft technology. Nowadays, HILS are widely used and gained their importance in the fields of power engineering, robotics, naval, space, control technologies and so on.

Hardware-in-the-loop simulations (HILS) have numerous advantages over numerical only simulations in testing the performance of components and control designs in controlled experiments under realistic conditions. Including a part of the real hardware in a simulation loop during the development phase can improve the optimality of the design. The advantages of HILS can be summaries as follows [9, 14, 15]:

- A real process can be carried out in the laboratory by partially moving the hardware and software, and it can be easily interfered by user or designer.
- Hardware and software can be tested under extreme conditions. E.g, under high or low temperatures, high electromagnetic interference, mechanical shocks and disruptive environment.
- The effects of the sensor accuracies and failures are observed.
- Experiments can be repeated.

- Save time and money on the development, test, validating phases of designs.
- Minimize the risks of realizing an error in a very final phase of the test on the field.
- In WECS which consists of mechanic (turbine and drive train), electrical (power electronics and load), electromagnetic (electrical machine) and control subsystems, HILS approach is an effective tool that is used in development of a component or entire system and productisation [16]. Therefore, the dynamics and transient effects are taken into account during the development of products from design phase through the prototype to the end product phase.

Different types of HILS can be classified into 3 types in [14]:

- The first one is the signal level HILS in which only the control system, namely the controller board, is used as a hardware in the simulation loop. Others such as power electronics and mechanical components are modeled and simulated in real-time.
- The second one is the power level HILS in which the controller board and the power electronics components, i.e converters, are used as hardwares in the simulation loop. Other possible components such as mechanical, electromechanical ones (electrical machines) and loads (e.g battery, grid) are numerically simulated.
- The third one is the mechanical level HILS in which the control unit, electrical machine and power electronics are tested while the mechanical components are simulated.

Consequently, according to the classification by [14], this study falls into the mechanical level HILS since, except the mechanical component (the VAWT rotor), electromechanical, power electronics, electrical load and control components are used in the simulation loop.

2.2.1 HIL simulations for wind turbines

There are many publications that report modeling a wind turbine numerically and provide the torque output via a motor that is considered as an actuator in the HILS [17, 18, 19, 20, 21, 22]. A common purpose in all these studies is being able to replicate the dynamic behavior of the wind turbine by a motor that is assigned as being responsible of the mechanical power source which is transmitted to the load in the WECS through the electromechanical and power electronics components. Since the inertia of the motor and drive train in the VAWT simulator are different than

the real wind turbine inertia, applying the wind torque directly in HILS leads to observing discrepancy at the angular acceleration as well as the rotational speed. Thus, essential calculations for emulating the actual inertia and mimicking the real turbine dynamics are done in HILS. This emulation calculations are tackled in [18, 19, 20, 21, 22] based on the method that can be described herein-below by Figure 2.3. The dynamics of two systems in Figure 2.3 are expressed in Equations 2.4 and 2.5.

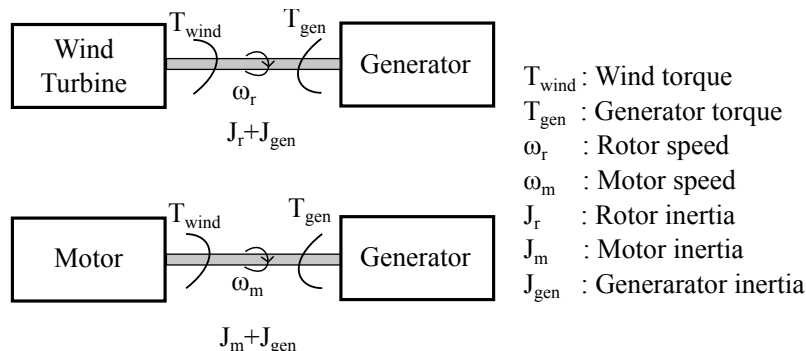


Figure 2.3: Actual wind turbine and emulated wind turbine generator system.

$$T_{wind} = (J_r + J_{gen})\dot{\omega}_r + T_{gen} \quad (2.4)$$

$$T_m = (J_m + J_{gen})\dot{\omega}_m + T_{gen} \quad (2.5)$$

If the reference motor torque is calculated in such a way as $T_m = T_{wind} - (J_r - J_m)\dot{\omega}_m$, and T_m is substituted in Equation 2.5, we obtain the following:

$$T_{wind} = (J_r + J_{gen})\dot{\omega}_m + T_{gen} \quad (2.6)$$

Notice the similarity between Equation 2.4 and 2.6. Obviously, dynamics of the motor-generator system matches to the dynamics of the wind turbine-generator system when $\omega_r = \omega_m$.

For an accurate estimation of the derivative of the motor speed ($\dot{\omega}_m$), a low-pass filter (LPF) may be necessary to eliminate the measurement noise [18, 20, 21]. However, filtering the speed for its derivative introduces delays which impede accurate mimicking of the VAWT system and successful implementation of the control algorithm. In order to alleviate the difficulties associated with delays, one can propose a closed-loop observer to calculate the derivative of the angular velocity and reject the noise as in [19]. An alternative method is developed to eliminate the calculations of the derivatives and presented in Section 4.4.

2.3 Control of wind turbines

Control design plays an important role in wind energy conversion systems to achieve high efficiency and performance, and it is essential for the safety of the system as well. There are numerous objectives of the control algorithm [23, 24], which are arranged into 3 topics.

- *Power regulation and energy maximization:* Below the rated or cut-out speed, maximum energy production is the goal.
- *Load mitigation and speed regulation:* This objective aims to protect the turbine by limiting the excessive mechanical forces and speeds.
- *Power quality:* Ensuring that the generated power quality matches the inter-connection standards.

Control of wind turbines is divided into 3 subsystems in [23] see Figure 2.4.

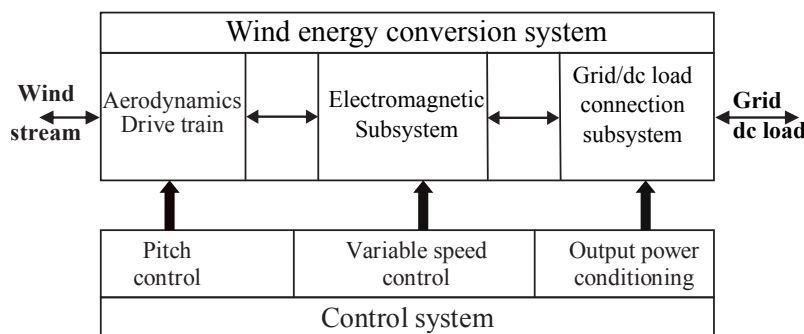


Figure 2.4: Principal control subsystems of a wind energy conversion system. [23]

In aerodynamic control, the angle of attack of the blades is varied to control the aerodynamic forces, and thus the amount of aerodynamic power generated by the wind turbine. This type of control can be viewed as power limiting or optimizing. Under the nominal conditions, the angle of attack does not change. When the wind speed attains higher value than the specified nominal speed, the angle of attack is passively or actively adjusted in order to keep the generated power at the nominal value. In passive stall control, the blades are designed in such a way that the angle of attack is changed when the wind speed exceeds the nominal value due to the turbulence forces on the blade surfaces. Thus, the rotational speed of the wind turbine does not increase and the power is regulated. Although passive stall control does not require a mechanism that is responsible of manipulating the angle of attack, a special blade design is needed. Moreover, in active stall control, a control mechanism adjusts the orientation of the blades in order to keep the power level at the nominal value. Lastly, the pitch control strategy which is similar to the active-stall control, controls the blades with an adjustable pitch mechanism. However,

the purpose is not only to limit the power above the nominal wind speed, but to optimize the operating point to maximize the power output.

In variable speed control, the goal is to capture the maximum power available from the wind by controlling the generator torque to keep the optimum operating speed at the desired level. In other words, tip speed ratio is remained at its optimal value (λ_{opt}), e.g see Figure 2.2. If the C_p curve of the wind turbine is known and the wind speed is measured, the reference speed is determined from Equation 2.3. In this concept, various control laws can be applied, e.g linear (PID) control, model predictive control and sliding mode control [23]. A difficulty of these methods is dealing with the induced wind speed deviations due to the turbulence, and it leads to predicting faulty optimal operating points and use them as a reference. Furthermore, they are based on the knowledge of the wind turbine characteristics which are hard to obtain with accurately and may vary as components age. Moreover, an accurate anemometer is required and it is costly. Therefore, they are not preferred for small scale wind energy conversion systems [25].

Another control method in variable speed control is the maximum power point tracking (MPPT) strategy. In [26], MPPT algorithms for small scale wind turbines are reviewed and grouped into two categories. The first group contains the methods based on knowledge of turbine parameters, and the second group contains the methods based on iterative search.

In the first group, the optimum power characteristic of the WECS with respect to rotational speed are used [27, 28], and previously specified power-speed characteristics are stored in a memory or approximated by a function, e.g curve fitting. Once the relation between the optimum operating speed and generated power is obtained, the system can be controlled by measuring either the rotational speed or power. Another way to generate optimum power point reference with known system parameters is measuring the wind speed [29, 30]. If the power coefficient curve ($\lambda - C_p(\lambda)$, see Figure 2.2) of the wind turbine is known, the optimum operating point can be directly calculated from Equation 2.3. Algorithms that are summarized above can find the optimum operating point. On the other hand, accurate model of the system must be determined to generate a reference value that keeps the system operation at the optimum. The aerodynamic power characteristics can be determined by a wind tunnel test which is not practical and can be costly. Furthermore, atmospheric conditions and aging cause altering of the system characteristics. In the method where the wind speed is measured, the data needs to be rapidly acquired in order to respond sudden changes in the wind and avoid undesired oscillations. Installing the anemometer near-by a wind turbine causes different forces on the anemometer due to the wake rotation. Lastly, the use of an anemometer increases the cost of overall system and the overall performance of the WECS becomes over-dependent

on information from the anemometer.

In the second group of MPPT algorithms, optimum operating point is iteratively searched, and it is generally called in literature as perturb and observe (P&O) control or hill-climbing control [25]. The advantage of the iterative approach is that the modelling errors are eliminated. Although the various kinds of MPPT techniques were proposed in literature, they are a modification of the following idea [26, 31]:

- For a given wind speed, power changes with the rotor velocity and there is only one rotational speed value where the power attains its maximum value. At that point, the derivative of the power with respect to velocity is zero, $\frac{dP}{d\omega} = 0$.

In P&O method, the direction for the maximum power point is determined by sampling and comparing the change of the power with respect to the speed ($\frac{\Delta P}{\Delta \omega}$) periodically as represented in Figure 2.5. Another MPPT method in literature is the incremental inductance method (INC) (or incremental MPPT), which is presented in [31] [32], and they have the same objective of finding the operating point where $\frac{dP}{d\omega} = 0$. However, in INC, the previous and instantaneous relation of output current and voltage are used rather than power and rotational speed. A MPPT algorithm based on this method is presented in Subsection 5.2.1 in detail.

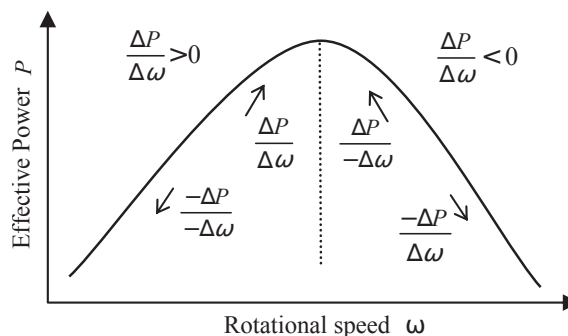


Figure 2.5: Possible directions that can be determined in MPPT process.

The MPPT algorithms based on P&O and INC methods have high reliability and can be simply implemented on WECS since there is no need to measure the wind speed and control algorithm does not require the turbine characteristics. However, these algorithms detect the direction of the maximum power point and generates a reference signal that has a fixed step size. The main disadvantage of the constant step size of the basic MPPT algorithm is the presence of fluctuations around the optimum operating point. Moreover, the response of the output power to the wind speed change can be extremely slow especially for turbines with a large inertia. There are various works in literature which offer modifications to the MPPT algorithm to minimize the oscillations around the optimum operating point with an adaptive iteration approach [33, 34, 32]. These methods can be used in the MPPT algorithm

for the small scale wind turbine systems but these optimizations are complex and eliminate the merit of the MPPT: the simplicity. The reliability, simplicity and low cost are essentials especially for the small standalone wind turbine systems located in the rural areas. Furthermore, the response of the system to wind speed change are fast since the small scale wind turbines has relatively low inertia. Therefore, the simple implementation of the MPPT algorithms are common for small scale wind turbines [33].

Chapter 3

Model

In this chapter, the mathematical model of the VAWT system given in Figure 1.4 is presented. First of all, the dynamic model of the VAWT is given in Section 3.1. Then, the PMSG and rectifier model are represented in Section 3.2.

3.1 Vertical axis wind turbine

The model parameters of the studied VAWT are listed in Table 3.1.

Parameter	Description	Value	Unit
J_r	Moment of inertia of the rotor	2	$kg - m^2$
R	Radius of the rotor	0.5	m
L	Length of a blade	1	$1m$
B	Friction coefficient	0.02	Ns/rad
ρ	Air density	1.2	kg/m^3

Table 3.1: The studied VAWT parameters.

In order to calculate the wind torque on to the VAWT rotor, Equation 2.2 and the angular velocity of the rotor (ω_r) are used as in Equation 3.1.

$$T_{wind} = \frac{P_{wind}}{\omega_r} = \frac{C_p(\lambda)\rho LRU_{wind}^3}{\omega_r} \quad [Nm] \quad (3.1)$$

The $C_p(\lambda)$ curve used in this study is depicted in Figure 2.2. $C_p(\lambda)$ is a function of TSR (λ), and approximated by a 6th order polynomial in Equation 3.2; the coefficients of the polynomial are listed in Table 3.2.

$$C_p(\lambda) = p_1\lambda^6 + p_2\lambda^5 + p_3\lambda^4 + p_4\lambda^3 + p_5\lambda^2 + p_6\lambda \quad [-] \quad (3.2)$$

Using the model parameters and the C_p curve, four different cases are calculated with 4 different wind velocities as depicted with respect to the rotor angular speed in

Coefficient	Value
p_1	-0.3015
p_2	1.9004
p_3	-4.3520
p_4	4.1121
p_5	-1.2969
p_6	0.2954

Table 3.2: The coefficient values used in C_p model.

Figure 3.1. The peak point of these power curves are listed in Table 3.3. Moreover, the maximum generated power ($P_{wind,max}$) and corresponding rotor speed (ω_r) and wind torque (T_{wind}) for wind velocities between 3 to 12 m/s were calculated and they are listed in Table 3.3 which can be useful to specify the operating regions described in Subsection 2.1.1.

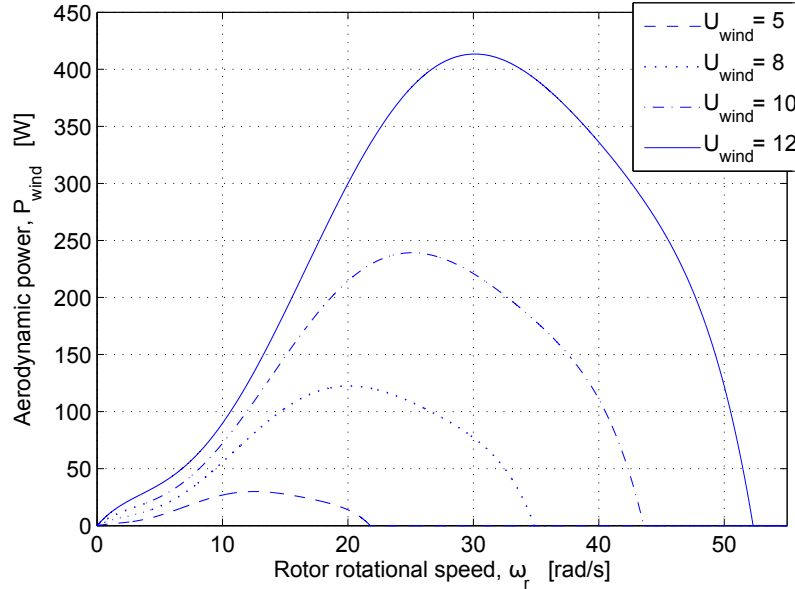


Figure 3.1: Aerodynamic power with respect to rotor rotational speed for different wind speeds; 12,10,8 and 5 m/s.

The operating regions are specified by considering the rotor speed and wind torque values at maximum aerodynamic power points for different wind speeds given in Table 3.3. Firstly, $U_{wind} = 4\text{m/s}$ was selected as cut-in speed since the maximum available power is not sufficient to operate the overall system against the frictional and copper losses below this speed. Secondly, the rated wind speed was selected as 8 m/s optimistically compared to the average wind speed data in Istanbul region given in [35] as 6.5 - 7 m/s. The cut-out speed was selected as 12 m/s, because the torque value attains over 13 Nm at this wind speed, and the torque value is considered relatively high for this VAWT system since the system may be not operate mechanically in safe over this torque value. Moreover, the generator may suffer due to the high copper losses and overheating in such a high-torque and low-speed

Operating region	U_{wind} [m/s]	$P_{wind,max}$ [W]	ω_r [rad/s]	T_{wind} [Nm]
Region-1	3	6.46	7.53	0.86
	4 (cut-in)	15.31	10.04	1.52
Region-2	5	29.90	12.55	2.38
	6	51.68	15.06	3.43
	7	82.06	17.57	4.67
	8 (rated)	122.50	20.08	6.10
Region-3	9	174.41	22.59	7.72
	10	239.24	25.10	9.53
	11	318.43	27.61	11.53
Region-4	12 (cut-out)	413.41	30.12	13.72

Table 3.3: Operating regions, maximum available aerodynamic power ($P_{wind,max}$) at rotor speed (ω_r) with torque (T_{wind}) values for wind speeds from 3 to 12 m/s.

operating region.

After discussing the operating regions of the wind turbine, equation of motion for the rotor is given by:

$$J_r \frac{d\omega_r}{dt} = T_{wind} - T_{gen} - T_{rf} \quad [Nm] \quad (3.3)$$

where J_r is the equivalent inertia of the rotor, T_{gen} is the generator torque on the rotor, T_{rf} is the friction torque, which is assumed to be proportional to ω_r by a coefficient B as follows:

$$T_{rf} = B\omega_r \quad [Nm] \quad (3.4)$$

3.2 Electromechanical model: generator and rectifier

In this section, the model of a PMSG with a passive bridge rectifier is presented. Firstly, an ideal model is studied and its representation is given in Figure 3.2. The ideal model is only useful for illustrative purposes and very basic calculations. In this case, the PMSG is considered as an ideal three-phase voltage source feeding a dc current through a passive diode rectifier.

The notation of the symbols to denote circuit quantities is summarised as follows:

- Instantaneous values of quantities vary with respect to time are denoted by italic lower case letters. For example $v_{an}(t)$ is the voltage difference between the node-a and neutral point, and $i_a(t)$ is the phase-a instantaneous current. As a further example $v_{ab}(t)$ is the voltage difference between the line-a and line-b, i.e it is line-to-line instantaneous voltage.

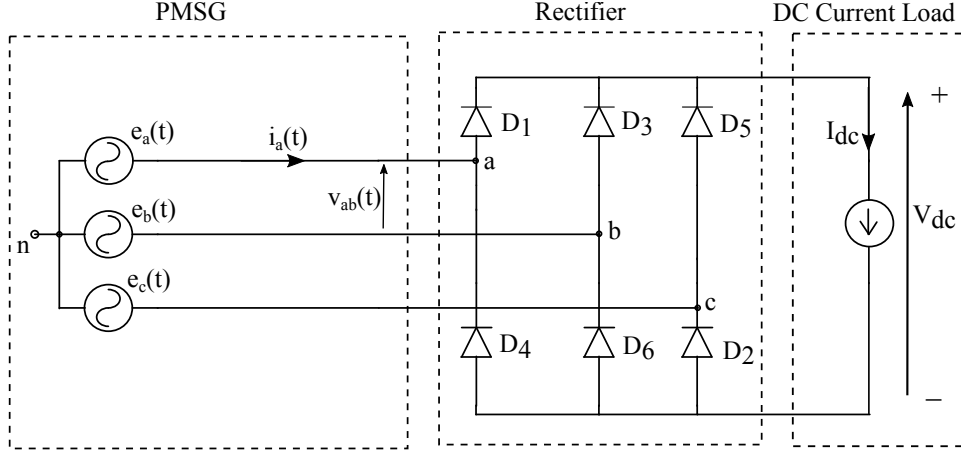


Figure 3.2: Representation of an ideal PMSG-rectifier model that is connected to a DC current load.

- The dc values or the RMS (effective) values of ac are indicated by italic upper case (capital) letters. For example, V_{dc} is the dc load voltage.
- In three phase circuits, the RMS value of the phase currents are denoted by I_L .
- In three phase circuits, the RMS values of line-to-neutral voltages are called "phase voltage" and denoted by V_{LN} .
- In three phase circuits, the effective (RMS) value of line-to-line voltages are called as "line voltage" and denoted by V_{LL} .

Based on the notation described above, instantaneous back-emf voltages can be expressed as follows:

$$e_a(t) = \sqrt{2}E_{LN} \sin(\omega_e t) \quad [V] \quad (3.5)$$

$$e_b(t) = \sqrt{2}E_{LN} \sin(\omega_e t - 2\pi/3) \quad [V] \quad (3.6)$$

$$e_c(t) = \sqrt{2}E_{LN} \sin(\omega_e t + 2\pi/3) \quad [V] \quad (3.7)$$

The electrical angular frequency is represented by ω_e . Notice that there are $2\pi/3$ radians (or 120°) phase shifts between the sinusoidal voltages whose RMS values (E_{LN}) are the same.

The instantaneous phase voltages are represented by $v_{an}(t), v_{bn}(t), v_{cn}(t)$ and their RMS voltages are equal and denoted by V_{LN} . As a result, they are given in

Equations 3.8-3.10.

$$v_a(t) = \sqrt{2}V_{LN} \sin(\omega_e t) \quad [V] \quad (3.8)$$

$$v_b(t) = \sqrt{2}V_{LN} \sin(\omega_e t - 2\pi/3) \quad [V] \quad (3.9)$$

$$v_c(t) = \sqrt{2}V_{LN} \sin(\omega_e t + 2\pi/3) \quad [V] \quad (3.10)$$

It is possible to see the line (line-to-line) voltage notations instead of phase (line-to-neutral) voltages in some sources. The relation between the line-to-line and line-to-neutral RMS voltages is given by

$$V_{LL} = \sqrt{3}V_{LN} \quad (3.11)$$

For ideal PMSG, the torque constant K_T and back emf constant K_e are defined to couple electric circuit with mechanical torque and speed as they are given in Equations 3.12 and 3.13. The torque constant is the ratio of electromagnetic torque created at the rotor to the phase current of the PMSG; the back-emf constant is the ratio of back-emf voltage generated in winding to the rotor speed of the PMSG [36].

$$E_{LN} = K_e \omega_{gen} \quad [V] \quad (3.12)$$

$$T_{gen} = K_T I_L \quad [A] \quad (3.13)$$

where E_{LN} is the RMS back-emf voltage, K_e is the back-emf constant, ω_{gen} is the PMSG mechanical rotational angular speed, T_{gen} is the electromagnetic torque created at the rotor of PMSG, K_T is the torque constant, I_L is the RMS phase current. Note that there is a linear relation between the mechanical angular speed ω_{gen} and electrical angular frequency ω_e as it is given in 3.14.

$$\omega_e = p\omega_{gen} \quad [rad/s] \quad (3.14)$$

where p is the number of pole pairs in the PMSG. Equation 3.14 describes that the electrical frequency of the PMSG is proportional to number of pole pairs since the stator windings face with the all poles during one mechanical turn and creates a full period of the sinusoidal voltage signal for each pole pair.

Notice that the ideal PMSG-rectifier in Figure 3.2 has no line inductance and resistances. Moreover, diodes are assumed as they are ideal and have no voltage drop and internal resistance. This ideal structure of the PMSG-rectifier model is good enough to understand the operating principles. According to standard textbook by Mohan [37], the diode with the highest potential at its anode conducts while the other two diodes are reverse biased in the top group of the diodes (D_1, D_2, D_3) in Figure 3.2. In the opposite way, the diode with the lowest potential at its cathode

conducts while other two diodes are reverse biased in the bottom ground of the diodes (D_2, D_4, D_6). Figure 3.3 shows the waveforms of phase voltages (v_{a-b-c}), phase current (i_a), dc voltage (V_{dc}) and dc current (I_{dc}) in the ideal PMSG-rectifier model.

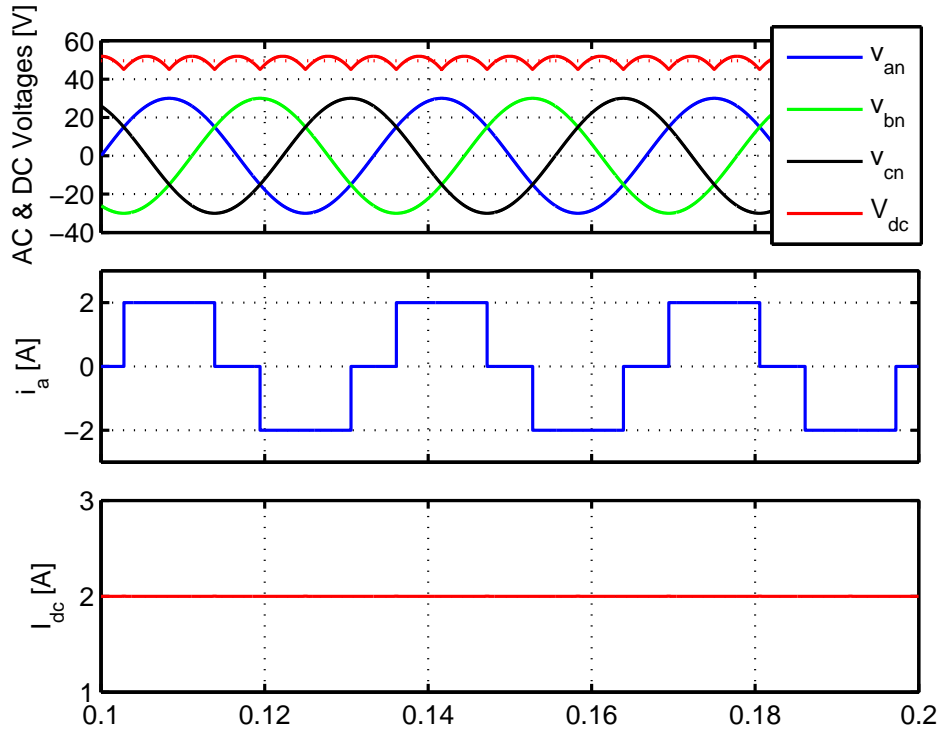


Figure 3.3: Ac and dc waveforms of the ideal PMSG-rectifier model shown in 3.2

As it can be seen from Figure 3.3, the instantaneous phase current i_a has a quasi-square waveform. Note that the other phase currents have the same amplitude and are 120° phase shifted, and removed the figure for visual clarity. To calculate the active power, the quasi-square waveform of the phase current can be expressed as sinusoidal components by means of Fourier analysis. If the quasi-square waveform is written as the summation of sinusoidal functions, the component with the lowest frequency is the "fundamental component" and its frequency is the "fundamental frequency." The frequencies of other components are integer multiples of the fundamental frequency, and those components are called "harmonics." As a result, the phase current i_a is the sum of its Fourier components as follows:

$$i_L(t) = i_{L1}(t) + \sum_{h \neq 1} i_{Lh}(t) \quad [A] \quad (3.15)$$

where i_{L1} is the fundamental component, and i_{Lh} is the harmonic component at the harmonic frequency. In addition to the instantaneous values, the relationship between the RMS value of the phase current I_L , RMS values of the fundamental

and harmonic components is expressed in Equation 3.16.

$$I_L = \left(I_{L1}^2 + \sum_{h \neq 1} I_{Lh}^2 \right)^{1/2} \quad (3.16)$$

The fundamental component of the line current i_L , qualitative waveforms of the phase voltage v_a , phase current i_a and first harmonic of phase current i_{a1} are depicted in Figure 3.4. Furthermore, the frequency spectrum of the phase current I_a that is depicted in Figure 3.4, is shown in Figure 3.5.

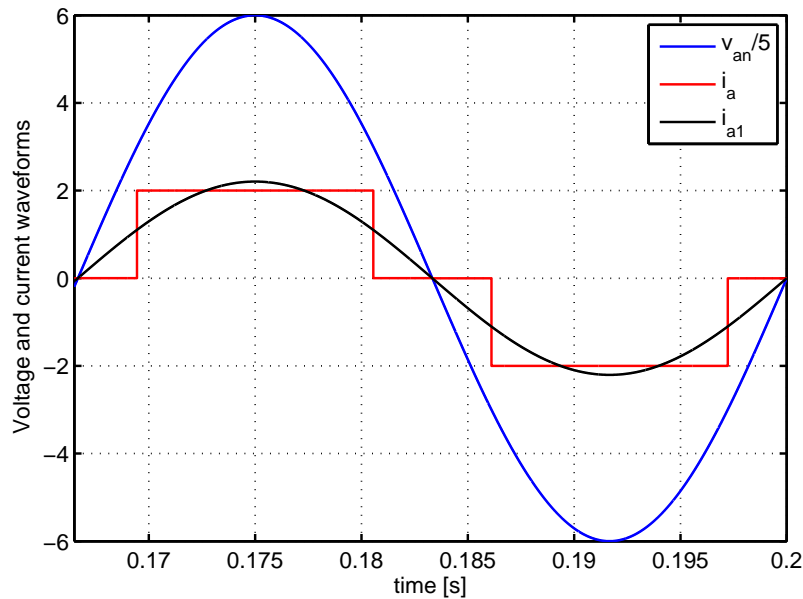


Figure 3.4: Ac waveforms of the idea PMSG model. Notice that v_{an} is divided by 5 in the plot for visual convenience.

Except the fundamental component, components of the current at harmonic frequencies have no contribution to the active (real) power P_{ac} drawn from the voltage source [37]. In principle, the more are the harmonic components of an ac signal, the more is its deviation from the sinusoidal form, and the less is the active power (P_{ac}). The amount of the current that makes the current far from being sinusoidal is called the distortion component i_{dis} , and it is used to calculate a quality factor called total harmonic distortion (THD). Later, the use of THD will be expressed on active power calculations, but first the calculations of distortion

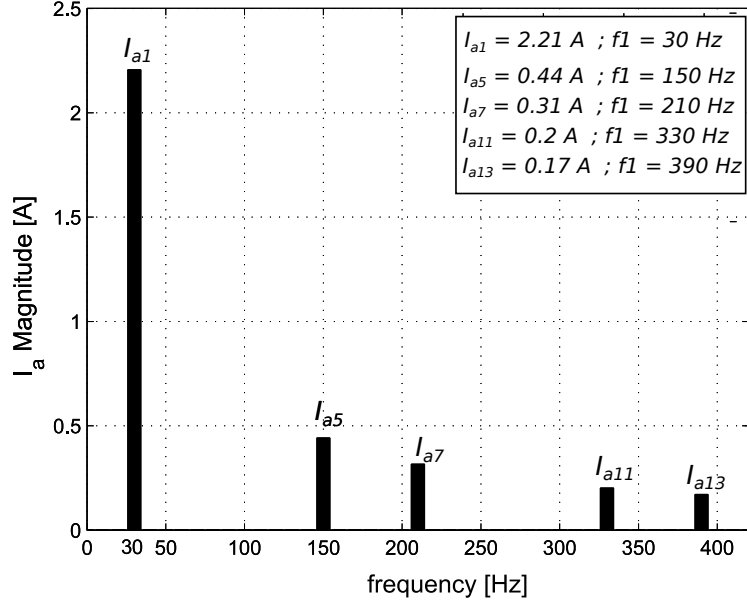


Figure 3.5: Frequency spectrum of the phase current I_a that is given in 3.4.

components both instantaneous, RMS and THD are given by Equations 3.17-3.19.

$$i_{dis} = i_L(t) - i_{L1}(t) = \sum_{h \neq 1} i_{Lh}(t) \quad [A] \quad (3.17)$$

$$I_{dis} = (I_L^2 - I_{L1}^2)^{1/2} = \left(\sum_{h \neq 1} I_{Lh}^2 \right)^{1/2} \quad [A] \quad (3.18)$$

$$\%THD = 100 \frac{I_{dis}}{I_{L1}} \quad [-] \quad (3.19)$$

The apparent power S_{ac} is a product of the RMS phase voltage V_{LN} and the current I_L as it is given in Equation 3.20. Note that in a 3-phase system, each phase has a contribution to the power, and hence the product of V_{LN} and I_L is multiplied by 3 [38], [39].

$$S_{ac} = 3V_{LN}I_L \quad [VA] \quad (3.20)$$

The fundamental component of the RMS phase current I_{a1} is in-phase with the RMS phase voltage V_{LN} and only the fundamental component of the phase current has contribution to the active power [37], [39]. Thereby, the RMS active power supplied by PMSG to the rectifier and its load is expressed by:

$$P_{ac} = 3V_{LN}I_{L1} = \sqrt{3}V_{LL}I_{L1} \quad [W] \quad (3.21)$$

Note that I_{L1} and V_{LN} are in-phase as it can be seen in Figure 3.4. By definition,

the power factor (pf) is given by:

$$pf = \frac{P_{ac}}{S_{ac}} = \frac{I_{L1}}{I_L} \quad [-] \quad (3.22)$$

For the ideal PMSG-rectifier, from Equation 3.19 and 3.22, the power factor can be also expressed by:

$$pf = \frac{1}{\sqrt{1 + THD^2}} \quad [-] \quad (3.23)$$

PMSG-rectifier circuit is simulated by using MATLAB/Simulink and an additional power electronic simulation software PSIM to calculate the THD of the 3-phase circuit that feeds the rectifier and the load. The obtained results for THD from the simulation is 0.3108 or 31.08 % and it is exactly the same value as calculated in [40]. Once the THD is known, the power factor pf is calculated as:

$$pf = \frac{1}{\sqrt{1 + 0.3108^2}} = 0.955 \quad [-] \quad (3.24)$$

The obtained pf value is the same as in the other reference sources [39], [37]. Therefore, the created simulation infrastructure can be considered as it can give reliable results for non-ideal PMSG-rectifier model simulations too. The actual power is 95.5%, rather than 100%, even with an ideal PMSG-rectifier since the line current is quasi-square and not sinusoidal.

Finally, dc quantities can be calculated by using ac quantities, and they are given by [37]:

$$V_{dc} = \frac{3}{\pi} \sqrt{2} V_{LL} = \frac{3}{\pi} \sqrt{6} V_{LN} \quad [V] \quad (3.25)$$

$$I_L = \sqrt{\frac{2}{3}} I_{dc} \quad [A] \quad (3.26)$$

$$I_{L1} = \frac{\sqrt{6}}{\pi} I_{dc} \quad [A] \quad (3.27)$$

Once the ideal model is studied, THD, pf , the relation between the ac and dc values are revised to obtain a non-ideal model of the PMSG-rectifier. The non-ideal model is not straightforward because neither PMSG nor the DC load has zero line impedance. Moreover, the diodes operate with threshold voltage and they are not ideal either. In PMSG, the resistance and inductance of stator windings need to be modeled in series with the ideal voltage sources as it represented in Figure 3.6. Moreover, a capacitor is added into the model to decrease the ripples in the dc voltage.

The phase inductance (L_s) makes the current commutations in the diodes of

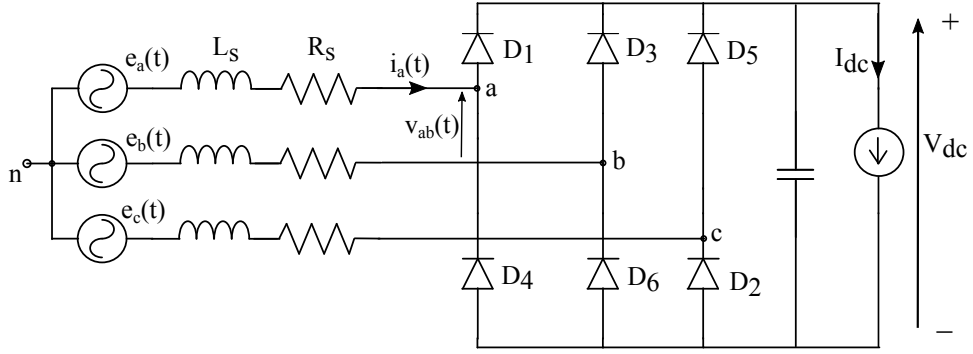


Figure 3.6: Representation of a non-ideal PMSG-rectifier model that is connected to a DC current load.

the rectifier are not instantaneous. These diode commutations cause distortions on voltage waveform.

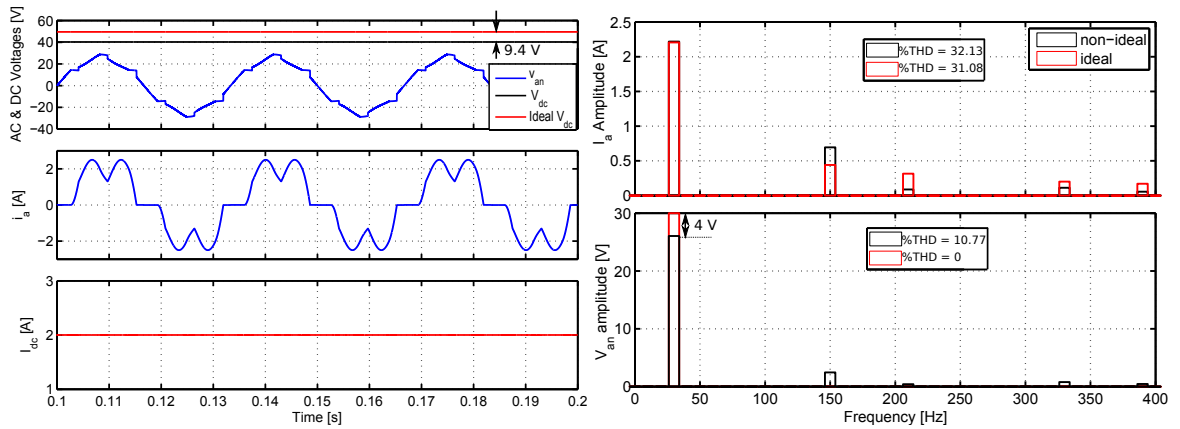


Figure 3.7: ac and dc waveforms of PMSG-rectifier the non-ideal model shown in 3.6 and their frequency spectrum. The results of the ideal PMSG-rectifier model results are shown in the plots for comparison.

In Figure 3.6, the plots at the left side show the ac and dc voltages and currents over a time period. The left-top plot shows the voltage of the "a" phase (v_{an}) and dc voltage (V_{dc}). Additionally, the average dc voltage in the ideal PMSG-rectifier is shown for comparison. Notice that there is 9.4 V voltage drop at dc voltage level in the non-ideal case compared to the ideal-case. In the left-bottom plot, the current of the phase "a" is shown. Lastly, in the left-middle plot, the dc current is shown. On the other hand, the frequency spectrum of the ac signals, i.e phase voltage and current, are shown in the right-hand-side plots. The right-top and bottom plots show the frequency spectra of the current and voltage of the "a" phase respectively. In order to compare these results with the ideal case, the ideal PMSG-rectifier model phase-a current and voltage signals frequency spectra are also given in the plots at right side. The most significant difference is the drops in the fundamental frequency of the phase voltage which is decreased by 13.3 %, i.e 4 V. Notice that the THD does

not significantly changed for phase current in the non-ideal model. However, the THD is increased from 0 to 10.77 % for the phase voltage, and resultant dc voltage is decreased from 49.62 to 40.25 V by 18.88 %.

In the literature, several works concerning the active rectification and the comparison of different converter topologies in terms of the resultant THD are presented [41], [42], [43],[44]. A meticulous analysis of the losses in the PMSG (such as the copper, core, and stray losses) and in the converter due to the THD can be conducted by developing a complex model with high accuracy. However, since the main focus of this study is not the harmonic mitigation and the modeling of the losses, such an approach is forgone and instead, a simpler model that includes the main principles of the PMSG-rectifier structure is used.

3.2.1 The simplified dc model

In the PMSG-rectifier structure, output voltage is proportional to the rotor speed of the generator [33]. The highest output voltage prevails when the load current is zero, and the voltage output decreases as the current increases. To determine how much the voltage drops for a given current and the generator speed, the PMSG and the rectifier are modelled by a transformation from the 3-phase model to an equivalent dc machine model by ignoring fast dynamics. In [45] and [46], a simplified dc equivalent model is proposed for PMSG-rectifier structure which is also adopted in this study by obtaining a relation between the 3-phase ac RMS values and dc potentials. The PMSG-rectifier model and the simplified equivalent dc model are shown in Figure 3.8.

In the simplified dc model, voltage drops can be calculated by using the speed of the generator and current drawn by the dc load. In addition to the resistive voltage drop, armature reaction in the generator and overlapping currents in the rectifier during commutation intervals are also taken into account for the voltage drop calculations in the simplified dc model. R_{over} term is added to the model to represent the average voltage drop due to the current commutation in the 3-phase passive diode bridge rectifier. This voltage drop from the current commutation is also explained in detail in [37]. The resistance R_{over} is calculated by the following [45], [46].

$$R_{over} = \frac{3L_s p \omega_{gen}}{\pi} \quad [\Omega] \quad (3.28)$$

where ω_{gen} is the angular rotational speed of the generator, i.e VAWT rotor speed, p is the number of the pole pairs in the PMSG. Additionally, diode threshold voltage V_{th} (on state voltage of the diode) is taken into account in voltage drop calculations. For positive values of V_{dc} , ω_{gen} and I_{dc} , resultant dc voltage V_{dc} can be calculated

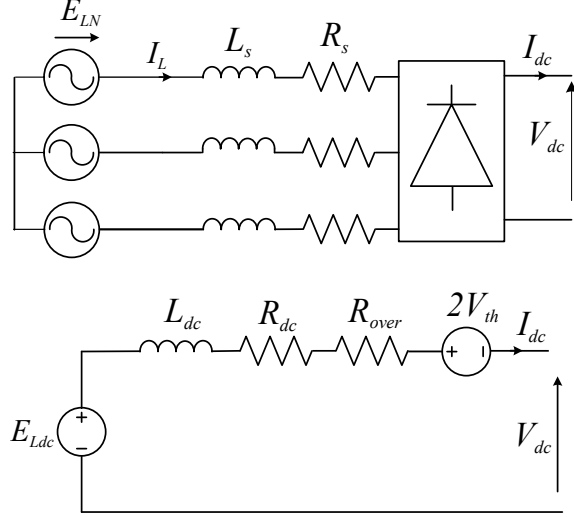


Figure 3.8: PMSG-rectifier and its simplified dc model. E_{LN} is electromotive force (EMF), L_s is phase inductance, R_s is the phase resistance of the PMSG, I_{dc} and V_{dc} are the average values of the dc current and voltage, respectively; E_{sdc} , L_{dc} , R_{dc} represents the correspondence values between the 3-phase ac model and the equivalent dc model.

from the following expression where the simplified dc model variables and their calculations are provided in Table 3.4.

$$V_{dc} = \sqrt{E_{sdc}^2 - (p\omega_{gen}L_{dc}I_{dc})^2} - (R_{dc} + R_{over})I_{dc} - 2V_{th} \quad [V] \quad (3.29)$$

Variable	PMSG	Dc Model
Flux	ϕ_s	$\phi_{dc} = 3\sqrt{6}\phi_s/\pi$
Back-emf	$E_{LN} = \phi_s p \omega_{gen}$	$E_{Ldc} = 3\sqrt{6}E_{LN}/\pi$
Inductance	L_s	$L_{dc} = 18L_s/\pi^2$
Resistance	R_s	$R_{dc} = 18R_s/\pi^2$

Table 3.4: PMSG and simplified dc model variables.

In summary, an ideal and a non-ideal PMSG-rectifier are modelled and simulated in this chapter. The dc voltage can be compared with the result of non-ideal PMSG-rectifier simulation which was implemented Matlab/Simulink and PSIM software programs. This verification study is done in Subsection 4.3.4.1 and results are given with the real PMSG-rectifier test results for comparison between the calculations, simulated and measured results.

Chapter 4

VAWT Simulator and HILS

This chapter presents the development of a VAWT simulator and HILS which consists of hardware and software. The numerical model of the VAWT is embedded into the software part, whereas the real PMSG, electric converter and the dc load are introduced into the simulation loop as the hardware components. The layout of the VAWT simulator is presented in the following section. Then, the components of the VAWT simulator are studied. Furthermore, the working principle of the system, communication of the hardware components and all related work that is done during development process are discussed in detail in this chapter. In Section 3.2, the developed PMSG-rectifier model validation is presented.

4.1 VAWT simulator layout

A schematic representation of the real VAWT and the VAWT simulator are shown in Figure 4.1. The HIL system consists of a permanent magnet synchronous motor (PMSM), a motor drive and a gear box to reduce the velocity of the motor that mimics the wind-driven rotor under arbitrary wind conditions. The permanent magnet synchronous generator (PMSG), which is also intended for use in the experimental VAWT system that is being developed in Sabanci University, and a programmable electronic load as the power sink are employed in the HIL system. As an interface between software (MATLAB/Simulink) and hardware, a dSpace controller card is used. In the VAWT system in Figure 4.1-(a), the wind torque (T_{wind}) is generated on the VAWT rotor while the rotor friction and generator torques, T_{rf} and T_{gen} , work against the wind torque. The equivalent inertia of the VAWT rotor and rotor rotational speed are represented by J_r and ω_r respectively. On the other hand, in Figure 4.1-(b) the physical variables such as speed, torque and inertia are clarified as follows:

- At the generator side of the gear box, i.e low speed side, the generator speed

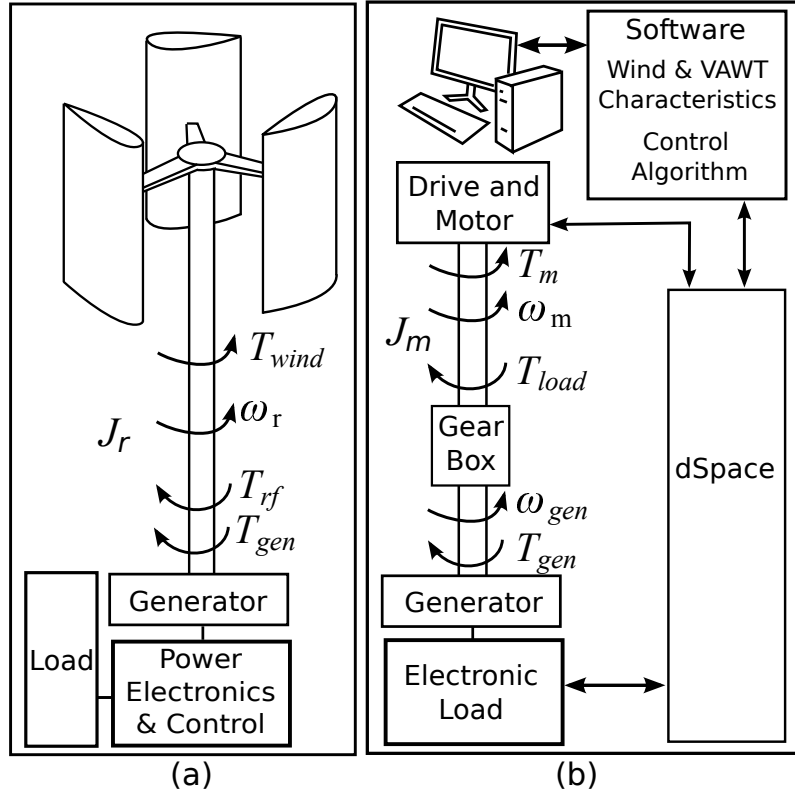


Figure 4.1: (a) Representation of VAWT system in real world, (b) VAWT simulator.

and torque are represented by ω_{gen} and T_{gen} respectively.

- At the motor side of the gear box, i.e high speed side, motor speed and torque are represented by ω_m and T_m . The equivalent inertia at the motor side of the gear box is represented by J_m . Lastly, T_{load} represents the total load torque at the motor shaft. This load torque can be calculated by Equation 4.1. Apart from that, the rotational speed of the generator, ω_{gen} , is linked to the motor speed by Equation 4.2.

$$T_{load} = \frac{T_{gen}}{\Gamma} + T_{hf} \quad [Nm] \quad (4.1)$$

$$\omega_{gen} = \frac{\omega_m}{\Gamma} \quad [rad/s] \quad (4.2)$$

where T_{gen} is the torque of the generator, Γ is the gear ratio and T_{hf} is the friction torque, which corresponds to the friction in all components of VAWT simulator drive train including the gear box, generator and the motor.

The actual photo of the VAWT simulator is in Figure 4.2.

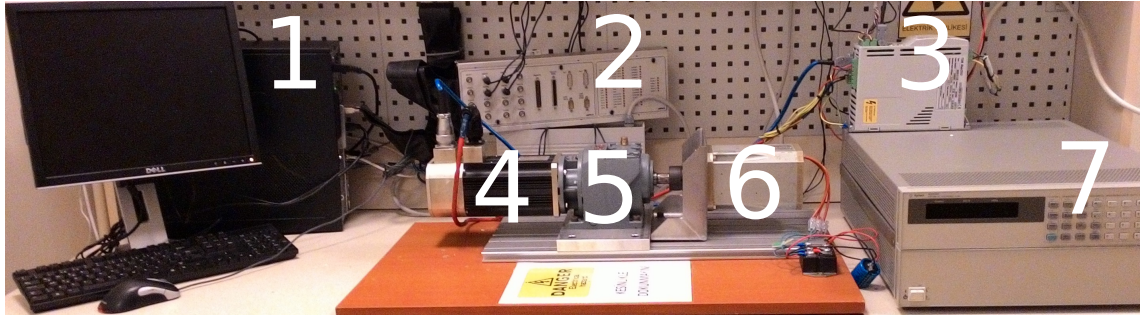


Figure 4.2: VAWT simulator components: 1- Host PC, 2- dSpace connector panel, 3- motor drive, 4- PMSM, 5- Gearbox, 6- PMSG, 7- Programmable dc load.

4.2 HIL components

Before discussing the VAWT simulator components, a conceptual schematic diagram of the HILS is depicted in Figure 4.3. Next, the intended use of each component, i.e software programs and hardware devices, and their communication principles are explained by referring to the general schema of the HIL simulation in Figure 4.3.

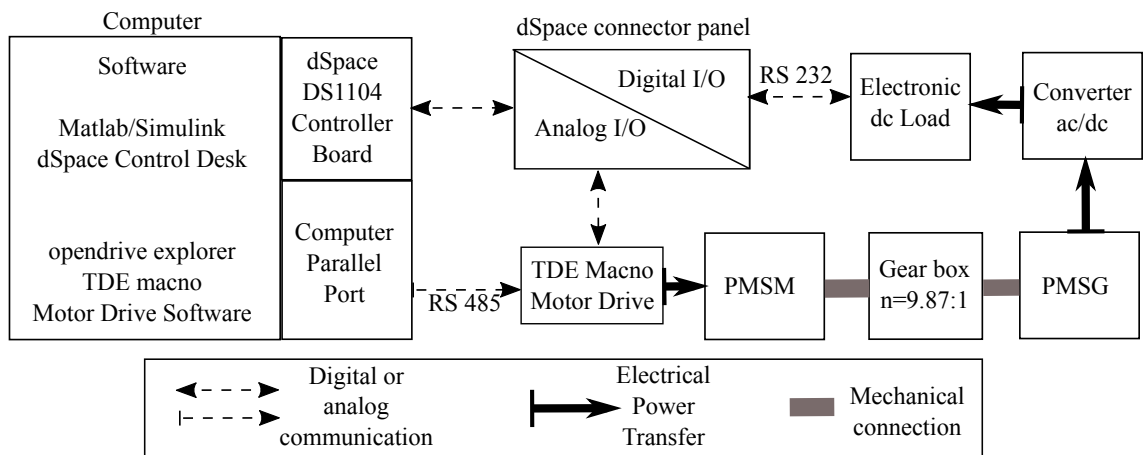


Figure 4.3: General schema of the HIL simulation.

4.2.1 Hardware components

4.2.1.1 Computer

A PC is used as a host computer for the dSpace application, and to run the required software programs. The host computer is a generic PC with Windows-7 32 bit operating system, quad-core Intel processor at 2.5GHz and 4 GB RAM. The dSpace controller board is connected to the host PC and communicates with the dSpace controller panel. Apart from that, the parameters of the motor drive are set in drive's software in the host PC and embedded into the drive through RS 485 communication standard.

4.2.1.2 dSpace

In order to implement a real time control loop, a dSpace DS1104 R&D controller board with the connector panel CP1105 are used. Once the motor drive parameters are initialized by the host PC, it can be controlled by analogue signals via dSpace connector panel. Furthermore, the electronic load is controlled with digital signals from the dSpace connector panel by using RS-232 communication standard.

4.2.1.3 Motor drive

In order to mimic the dynamics of the VAWT system, the torque of the PMSM is controlled by a motor drive: Mini OPD EXP 400V, with 6.8 A RMS rated current. The drive can be pre-programmed via RS 485 modbus communication port by the host PC to initialize parameters related with the motor used in the application. The drive can take speed or position feedback depending on the feedback (resolver, encoder and hall sensor etc) board, and the drive in this application has a resolver feedback board. The speed and torque of the motor can also be controlled and monitored by analogue I/O ports.

4.2.1.4 Motor

The PMSM (Femsan 5F100810001) is used as an actuator in the VAWT simulator to produce the required torque at the generator rotor. The motor parameters given by the manufacturer are tabulated in Table 4.1.

Parameters	Values/ types
Nominal torque	2.72 Nm
Nominal current	6.8 A
Nominal speed	4000 rpm
Nominal power	1139 W
Voltage constant	25.5 V/krpm
Torque constant	0.4 Nm/A
Poles	8
Speed sensor	Resolver - 15 Pins
Rotor inertia, $J_{m,rotor}$	$4.4 \times 10^{-4} kgm^2$

Table 4.1: Femsan 5F100810001 motor parameters.

4.2.1.5 Gearbox

A gearbox (Yilmaz Reduktor MN002–B07) is used to reduce the speed and increase the torque on the generator since the motor nominal operating point has higher speed and lower torque than the VAWT operation point. The speed reduction ratio of the gear box is 9.87.

4.2.1.6 Generator

The parameters of the PMSG are experimentally obtained in Section 4.3.

4.2.1.7 ac/dc converter

A 3-phase diode bridge rectifier IXYS VUO160-12NO7 is used to convert 3 phase ac output of the PMSG to dc. The rectifier's reverse blocking voltage is 1200 V and the maximum output current is 175 A. The equivalent model for forward voltage drop calculation is given in its data sheet [47]; the threshold voltage is 0.77 V and the slope resistance is 2.2 $m\Omega$.

4.2.1.8 Electronic load

Agilent N3306A is a programmable electronic load which is used in the VAWT simulator as a power sink. The operating contour and inputs ratings are specified in [48] and depicted in Figure 4.4. The electronic load works with SCPI (Standart Com-

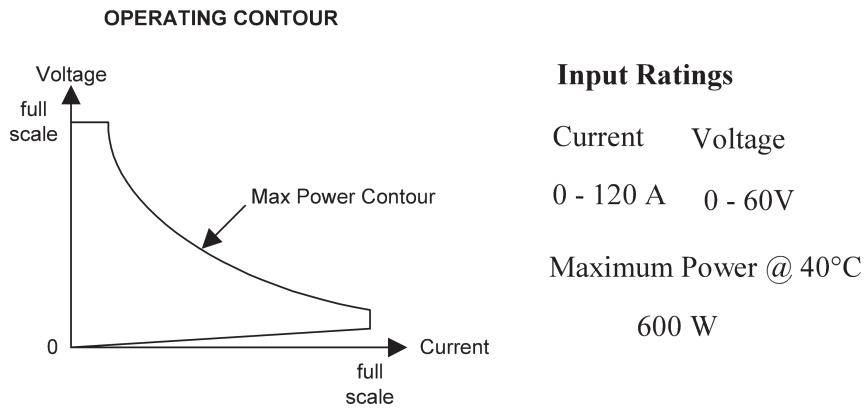


Figure 4.4: Input ratings and operating contour of electronic load Agilent N3306A. [48]

mands for Programmable Instruments) programming language, and the instrument functions are controlled over the RS-232 interface.

4.2.2 Software programs

In this subsection, the purpose and working principles of the software programs are discussed, and each of them are represented under a title.

4.2.2.1 OPD explorer

OPD explorer is a software that configures and operates the Mini OPD EXP motor drive. OPD explorer allows serial communication with the drive and an RS-485 adapter connected to the usb port of the host PC is used for the communication.

4.2.2.2 dSpace software

In the VAWT simulator, dSpace "real time interface" (RTI) is used. The software has serial and analogue communication block libraries. These blocks enable the use of the dSpace connector panel properly for communication with the motor drive and electronic load. The RTI is able to transform the model developed in Simulink environment to a C code.

ControlDesk is the user-interface of the real-time simulation that is running in the dSpace DS1104 board. It enables downloading of applications into the DS1104 and monitor the experiments. The variables can be plotted or control signals can be changed while the real-time simulation is running.

4.2.3 Software implementation

The designed simulation in Simulink consists of six main blocks and the general diagram of the simulation blocks is given in Figure 4.5. The content of each block

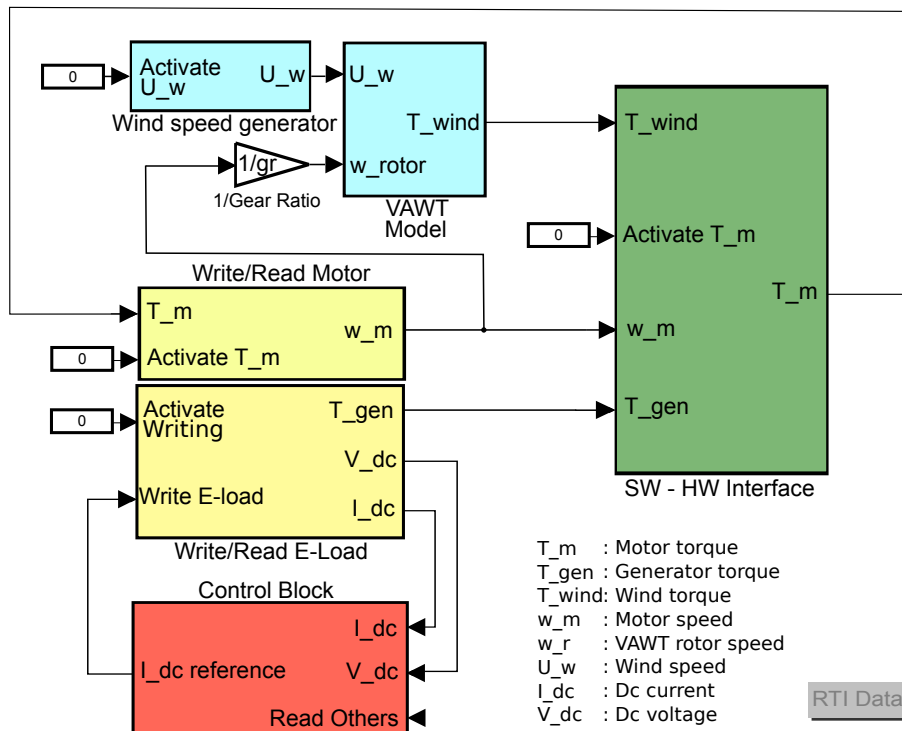


Figure 4.5: Main simulation file created in Simulink.

is summarized individually with the block name as the title in this subsection.

4.2.3.1 Wind speed generator

This block includes the wind speed model which can be arbitrarily set by the user or embedded as previously recorded real wind data. The block output feeds the

VAWT numerical model block.

4.2.3.2 VAWT model

This block includes the VAWT aerodynamic model which is given in Section 3.1. The wind speed and rotor speed inputs are used to calculate the TSR, and hence C_p by Equation 3.2. Once the power coefficient C_p is obtained, the wind torque (T_{wind}) is calculated by Equation 3.1.

4.2.3.3 Software - Hardware (SW - HW) interface

Consider the real VAWT system; the wind torque acts on the VAWT rotor as well as on the direct-driven generator. In the VAWT simulator, motor is the actuator, thus the motor torque must be the same as the torque generated by the actual VAWT. In this regard, SW-HW Interface block is used for inertia emulation, VAWT simulator drive-train friction calculation, and disturbance torque compensation to calculate the necessary motor torque. The development of the inertia emulation calculation is described in Section 4.4.

4.2.3.4 Write/Read motor

This subsystem contains the routines of dSpace analogue input/output communication. Analogue channels on the dSpace connector panel and analog inputs and outputs in the motor drive are set to work between 0 and 10 V. The motor torque data, which is in the range of 0 to 6.8 Nm, are mapped linearly into the range of 0-10 V and fed to the motor drive. The same mapping also applied for reading the motor speed and torque information. For example, 10-V reading at the speed reading terminal of the motor drive means the motor operates at its maximum rated speed, i.e 4000 rpm, while 5 V means the motor operates at 50 % of its rated speed, i.e 2000 rpm.

4.2.3.5 Control block

The control unit adjusts generator torque to operate the system at maximum efficiency. It ensures that the turbine is driven at the optimal rotor speed for a particular wind velocity. The developed control algorithms are presented in Chapter 5.

4.2.3.6 Write/Read E-load

The programmable electronic load communicates with the dSpace controller card by a serial communication protocol. The dSpace RTI add-on blocks were used to carry out the protocol. The serial setup is used to set the global parameters such as baud

rate, data bits, stop bits and parity bits. In the block, UART parameters and RS-232 routines can be configured properly to assure the data transmission/reception with the E-load. The data is transmitted and received in ASCII form. The E-load uses SCPI programming language over the RS-232 interface. For example, to draw 2.4 A by the load, the character mode in Figure 4.6 must be translated into the ASCII form to execute the command. Additionally, CR/LF (Carriage Return/Line Feed) ASCII characters needs to be added at the and of the sending data.

SCPI Lang : C U R R ^{space} 0 2 . 4 0 CR LF
 Ascii Form : [67 85 82 82 32 48 50 46 52 48 13 10]

Figure 4.6: Character to ASCII transferred data.

Although MATLAB has a function to transform strings into ASCII arrays, this function cannot be used in dSpace since the code cannot be compiled with character format. Therefore, a communication routine is developed to pack the intended commands and query data into the arrays and send it to dSpace transmission block. Moreover, after sending the query signal, the received ASCII data is interpreted to obtain present voltage and current values. All of these are handled in the Write/Read E-load subsystem that is given in Figure 4.7.

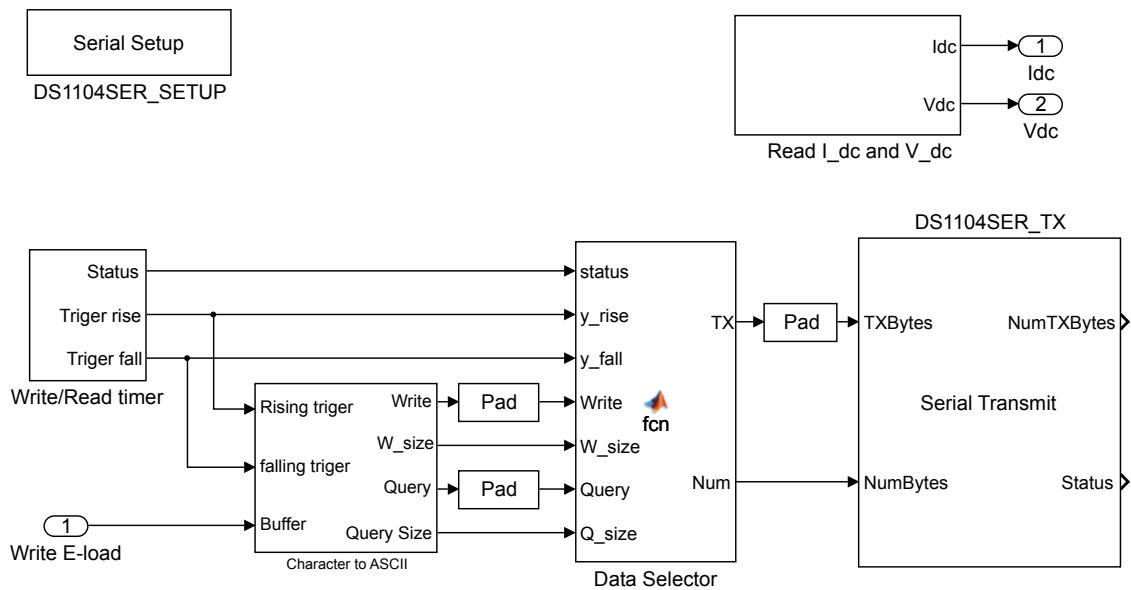


Figure 4.7: Content of the Write/Read E-load subsystem.

A timer block is developed to reserve time slots for writing the intended current value, query data and received current and voltage data in the serial communication line. This block is a pulse generator which has an adjustable period and duty cycle. Data is converted to ASCII form in the **Character to ASCII** code block, and the array size is supplemented to required sizes by **Pad** block. The data selector channels

the current and query data into the dSpace serial transmission block (DS1104SER_TX) depending on the timer status. Reserved times for sending current and query data, and receiving the incoming data are depicted in Figure 4.8. The 12-byte current data are transmitted when a rising edge of the pulse signal is detected, and the 18-byte query data is transmitted when the falling edge is detected. Once the query data is delivered, the feedback data is awaited during the low state of pulse signal, and proceed by `Read I_dc` and `V_dc` block during a predefined reserved time. Notice that the current and voltage feedback informations are delivered from E-load to the dSpace connector panel partially at two different times. First 10 bytes of current data arrives, and then voltage data arrives in a 13 byte array. This process continues sequentially in every 0.1 second, which is the period of the pulse signal.

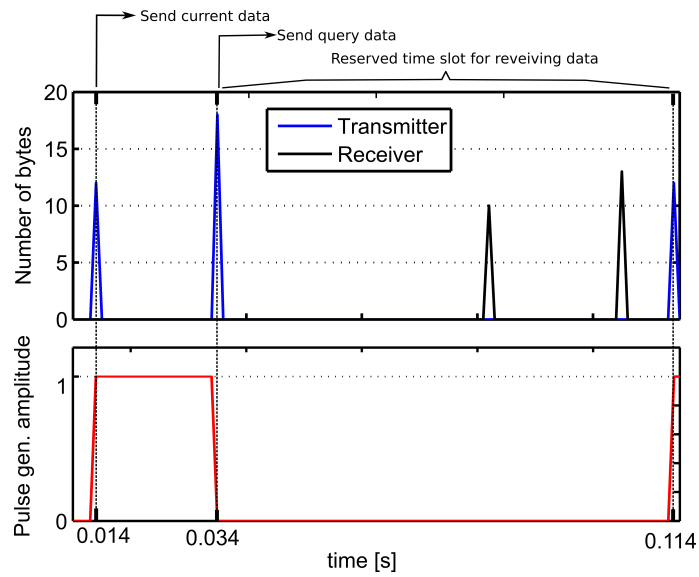


Figure 4.8: Number of bytes output of the transmitter and receiver blocks are plotted with the pulse signal.

4.3 Model validation and parameter identification

4.3.1 Number of pole pairs in PMSG

The generator pole pairs represent the number of north and south magnets around the rotor. The number of pole pairs can be found by measuring the mechanical and electrical frequency, with the help of Equation 3.14. To find the number of the pole pairs, the motor was spun at constant 3000 rpm (314.16 rad/s) which results the speed of 31.83 rad/s at the generator side of the gear box. So, while the generator was operating at that speed, its line voltage and frequency were measured. The measurement result was saved by an oscilloscope (*Agilent Technologies Infiniivision DSO-X 3014A Digital Oscilloscope*) and depicted in Figure 4.9. The number of pole

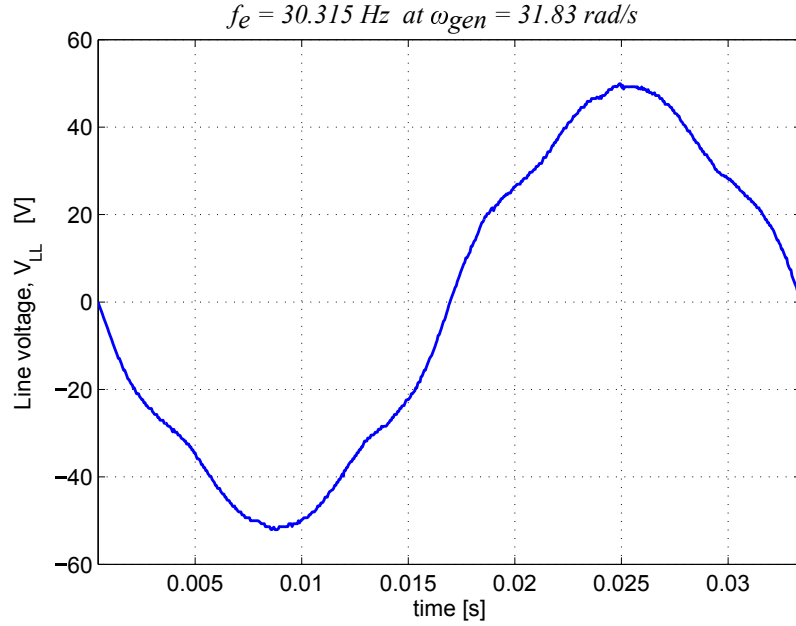


Figure 4.9: PMSG line voltage measurement under 31.83 rad/s mechanical speed.

pairs, p , was calculated from Equation 4.3 as 5.98. Note that the number of poles must be an integer. Thus, the PMSG has 12 poles, 6-pole pairs on its rotor.

$$p = \frac{\omega_e}{\omega_{gen}} = \frac{2\pi f_e}{\omega_{gen}} \quad [-] \quad (4.3)$$

4.3.2 Equivalent moment of inertia estimation

The equivalent inertia of the drive train in the VAWT simulator (motor, gearbox and generator) needs to be estimated since this value is used in calculations for real VAWT inertia emulation. For that purpose, a sinusoidal torque reference was applied to the motor while its position was measured.

Under the assumption that a motor spinning with no mechanical load and friction is negligible, the equation of motion for such a system can be written as follows:

$$T_m = J_m \ddot{Q}_m \quad (4.4)$$

where T_m is the motor torque, Q_m is the rotor position and J_m is the equivalent inertia at the motor shaft. If a sinusoidal torque, $T_m = A \sin(\omega_m t)$, is applied to the motor and initial conditions are zero, Equation 4.4 can be solved for the rotor position, Q_m , as follows:

$$Q_m = -\frac{A}{J_m \omega_e^2} \sin(\omega_m t) = \frac{A}{J_m \omega_e^2} \sin(\omega_m t - \pi) \quad [rad] \quad (4.5)$$

So, position follows the sinusoidal torque input with a sinusoidal function that os-

cillates with the same frequency but has π radians phase difference. The equivalent inertia J_m affects only the amplitude of the sinusoidal that is expressed in Equation 4.5. Thereby, from the amplitudes of torque and position functions which are sinusoidal, equivalent inertia (J_m) can be obtained from:

$$J_m = \frac{|T_m|}{|Q_m|\omega_e^2} \quad [kg.m^2] \quad (4.6)$$

Applied sinusoidal torque and the resultant angular position are plotted in Figure 4.10. Since the real system contains other torque disturbances, the phase difference

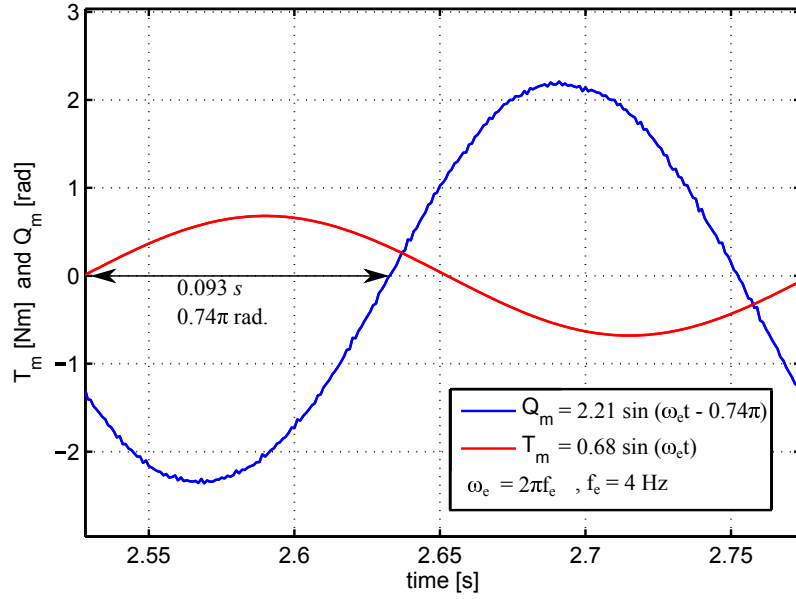


Figure 4.10: Motor torque and angular position with respect to time.

between T_m and Q_m is not π , but 0.74π . However the phase difference does not have an effect and the amplitudes of the T_m and Q_m can be used to obtain an estimate for the J_m as follows:

$$J_m = \frac{0.68}{2.21(2\pi f_e)^2} = 4.88 \times 10^{-4} \quad [kgm^2] \quad (4.7)$$

The estimated J_m value is 4.88×10^{-4} and this value is close to the value of the rotor inertia of the motor supplied by the manufacturer; $J_{m,rotor} = 4.4 \times 10^{-4}$ (see Table 4.1). Moreover, the equivalent inertia at the motor side of the gear box, J_m , of a drive train that is depicted in Figure 4.11, can be calculated by Equation 4.8. Notice that inertias at the high torque side of the gear box are divided by gear-box-ratio square in equivalent inertia calculation in Equation 4.8. Remember that the gear ratio of the gear box in VAWT simulator is 9.87, accordingly the motor's rotor inertia value is the major factor in equivalent inertia calculation.

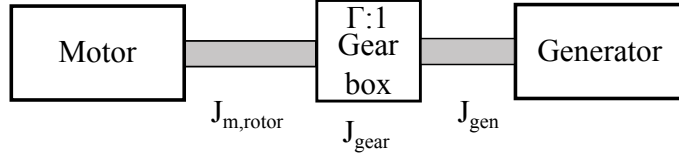


Figure 4.11: Schematic of motor-gear box-generator drive train in VAWT simulator. $J_{m,motor}$ is the motor-shaft-only inertia, J_{gear} is the gear box equivalent inertia, J_{gen} is the generator inertia and Γ is the gear box ratio.

$$J_m = J_{m,rotor} + \frac{1}{\Gamma^2}(J_{gear} + J_{gen}) \quad [kgm^2] \quad (4.8)$$

4.3.3 Friction torque

The friction torque of the drive train in VAWT simulator is estimated by running the motor in the absence of a load at different speeds and by measuring the current drawn. The product of the values of the current and the torque constant of the motor is used to estimate the friction torque. However the non-linear structure of the gear box causes obtaining different values for the friction torque with small deviations under the same spinning speed. Test data was gathered by running the motor at low speed and by increasing the speed gradually up to the maximum speed of the motor. Then, this procedure was repeated by starting the test at high speed and decreasing it gradually until the motor stops. Moreover, these tests were repeated after running the experiment at high speed under high torque sufficiently long time to see the results under different temperatures. The measured speed-torque data and the fitting curve that is found by least-square regression method are presented in Figure 4.12.

Fitting curve function is expressed by the following:

$$T_{hf}(\omega_m) = -1.418 \times 10^{-6}\omega_m^2 + 1.327 \times 10^{-3}\omega_m + 0.175 \quad [nm] \quad (4.9)$$

Equation 4.9 is used as friction model for inertia emulation calculations which is presented in Section 4.4.

4.3.4 PMSG and rectifier model parameters validation

In this subsection, model parameters are discussed for the non-ideal PMSG-rectifier model, which is described in Section 3.2sec. Firstly, the line resistance and inductance of the PMSG is measured by a RLC meter (UNI-T UT603): the line resistance is obtained as $R_s = 1.6 \Omega$ and the inductance as $L_s = 4.6 \text{ mH}$. Secondly, a test is made to gather data for back-emf parameter, which is given by the following expres-

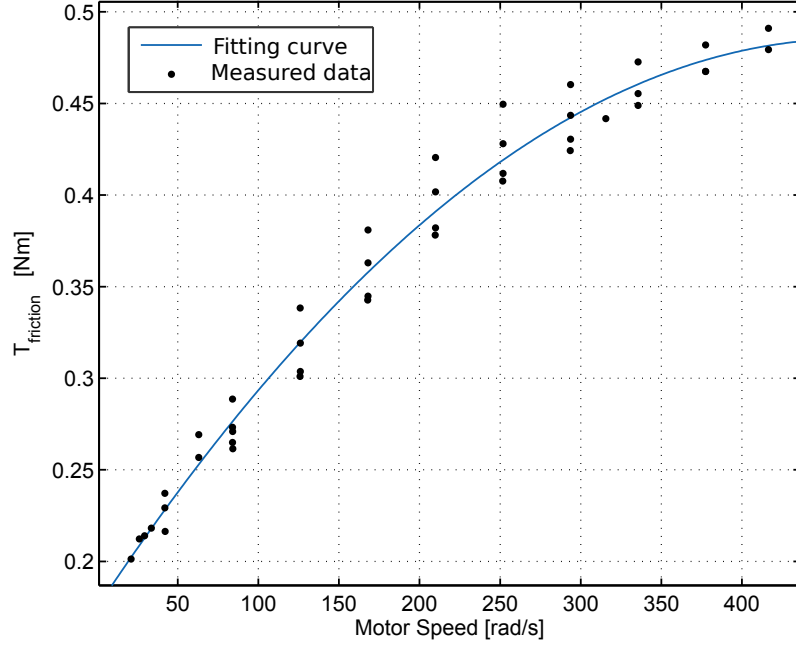


Figure 4.12: Friction torque with respect to motor speed.

sion:

$$E_{LN} = \phi_s p \omega_{gen} \quad [V] \quad (4.10)$$

A test could have been done by measuring the generator mechanical speed and line to neutral open circuit voltage, V_{LN} , since the back-emf is equal to phase voltage, i.e. $V_{LN} = E_{LN}$ under open circuit conditions. However, the generator's neutral point is located in the stator and it is not possible to practically reach that point. Thus, the tests are carried out by measuring line voltages since it is equal to square root of three times the phase voltage ($V_{LL} = \sqrt{3}V_{LN}$, see Equation 3.11). Hence, the flux ϕ_s is calculated as follows:

$$V_{LL} = \sqrt{3}\phi_s p \omega_{gen} \Rightarrow \phi_s = \frac{V_{LL}}{\sqrt{3}p\omega_{gen}} \quad (4.11)$$

As a result, a test was done by running the generator at 31.83 rad/s and RMS line voltage is measured with an oscilloscope and collected data is plotted in Figure 4.13. From the test result, flux is calculated; $\phi_s = 0.1069$.

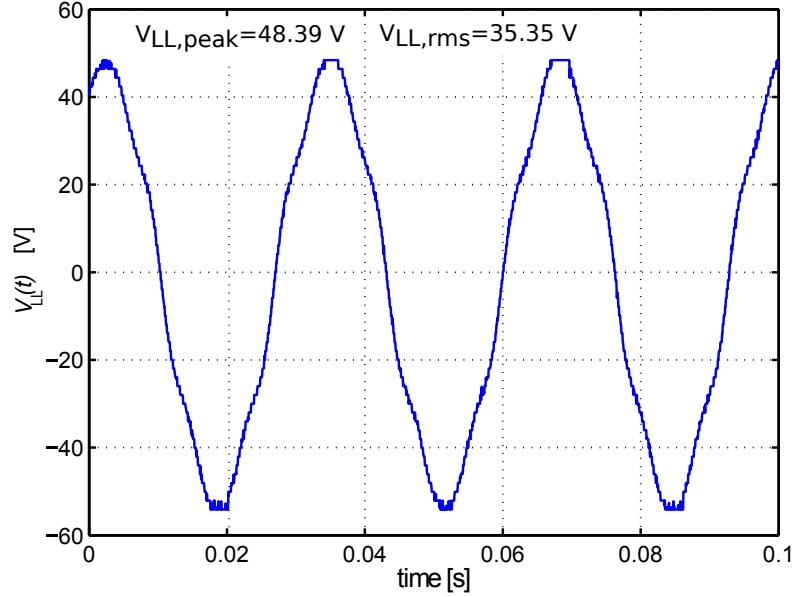


Figure 4.13: Measured open circuit line voltage of PMSG under $\omega_{gen} = 31.83 \text{ rad/s}$.

Once the constant value ϕ_s is estimated, several tests can be done by drawing dc current and compare the resultant line voltage and phase current with the non-ideal PMSG-rectifier model presented in Section 3.2. Following subsection contains that study results.

4.3.4.1 Validation of non-ideal PMSG-rectifier model

In order to validate the non-ideal PMSG-rectifier model and its dc equivalent model, several tests were done by running the generator at different speeds and drawing different dc currents. The list of experiments is provided in Table 4.2.

Test No	ω_{gen}	I_{dc}
Test 1.1	31.83 rad/s	1 A
Test 1.2		3 A
Test 1.3		5 A
Test 2.1	21.22 rad/s	1 A
Test 2.2		3 A
Test 2.3		5 A

Table 4.2: Validation test numbers and their contents for non-ideal PMSG-rectifier model

To compare the results of the non-ideal PMSG-rectifier model and the real PMSG-rectifier performance, PMSG line voltages were measured via the oscilloscope. Additionally, the phase current was measured by a contact-less current probe (HEWLETT PACKARD 1146A AC/DC Current Probe) and saved via the oscilloscope. Then, the THD of the measured line voltage and phase currents were calculated to compare them with PMSG-rectifier model simulation results. Sample results Test 1.2 are plotted in Figure 4.14 with the results of the non-ideal PMSG-rectifier

model simulation, which was carried out under the same conditions. Additionally, the THD results for both the simulation and the experiment are depicted in Figure 4.15.

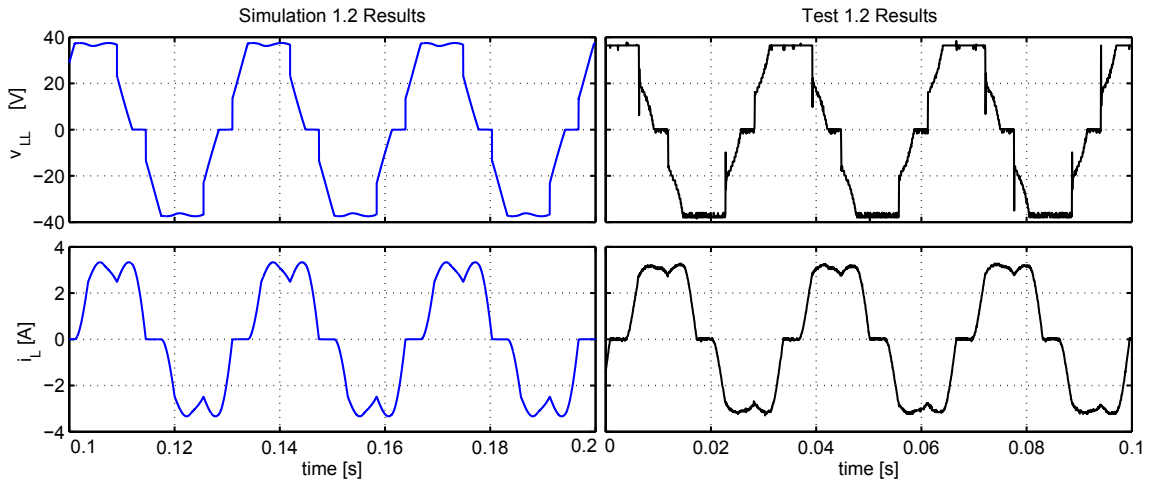


Figure 4.14: line voltage and phase current of the model simulation (left) and Test 2.1 (right). The PMSG runs at $\omega_{gen} = 31.83$ rad/s and 3 A is drawn by dc load.

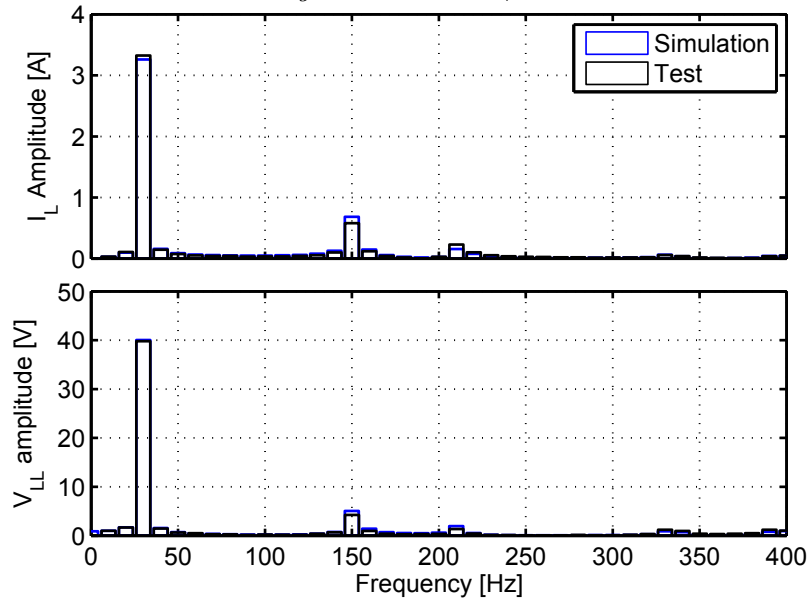


Figure 4.15: Frequency spectrum of the signals that are plotted in Figure 4.14

As it can be seen from both Figure 4.14 and 4.15 results, experimental results agree well with the non-ideal PMSG-rectifier model simulation. Furthermore, the results for the THD of the line voltage and the phase current are compared in Table 4.3.

According to the results in Table 4.3, the most significant deviation (44.39 %) appears on Test 2.1 phase current values. It indicates that, the phase current in the simulation is less sinusoidal than the experiments. A reason of this would be the measurement error, since the contact-less magnetic sensor is used; the sensor

Test No	Phase current THD %			Line voltage THD %		
	Experiment	Simulation	Deviation %	Experiment	Simulation	Deviation %
1.1	36.82	39.66	7.71	8.98	8.53	-5.01
1.2	20.60	22.66	10	14.17	16.38	15.84
1.3	14.48	15.46	6.77	20.88	22.72	8.81
2.1	28.81	41.6	44.39	8.73	9.42	7.90
2.2	20.12	21.27	5.71	14.84	17.83	20.15
2.3	13.03	12.61	-3.22	22.75	25.04	10.06

Table 4.3: Line voltage and phase current THD% results of experiment and simulation. To calculate the deviations, experimental results are selected as base point.

may smooth the sharp transitions of a square-like signal and make the oscilloscope display a sinusoidal-like signal that has less THD.

4.3.4.2 Validation of simplified dc model

Induced potential at the generator windings takes its maximum value under open circuit operation. Once the current is drawn by load, voltage drops due to the line resistance, armature reaction in the generator, overlapping current in the rectifier during commutation intervals and diode internal resistance. Consequently, the dc load voltage is a function of the generator speed and the dc load current. In order to validate the non-ideal PMSG-rectifier model and simplified dc model, experimentally obtained dc output voltage values are compared under the same test conditions which are given in Table 4.2. The dc voltage values from the experiments, simulated non-ideal PMSG-rectifier model and simplified dc model are listed in Table 4.4. Note that the dc voltage of the simplified dc model was numerically calculated from Equation 3.29.

Test No	Resultant load voltage, V_{dc}			Deviation % (Numerical to Experimen)
	Experimen	Simulation of non-ideal PMSG-rectifier	Numerical calculation of simplified dc model	
1.1	42.64	42.41	43.61	2.27
1.2	35.10	35.34	35.87	2.19
1.3	28.26	28.97	27.94	-1.13
2.1	26.98	26.8	27.58	2.22
2.2	20.27	20.28	20.49	1.08
2.3	14.23	14.46	13.25	-6.89

Table 4.4: Obtained dc load voltage from the real PMSG-rectifier, non-ideal PMSG-rectifier simulation model and numerical model. Deviation % column shows the percentage deviations of numerically calculated voltage to experimentally measured ones.

According to the results in Table 4.4, deviation between the simulated model and experimental results are below 1 percent. The deviation between the numerically calculated and experimental measured values are listed in Table 4.4 under the right-most column. According to the values under the deviation column, it can be said

that simplified dc model is satisfactory.

Since controlling the generator speed is a way to control the VAWT for maximum power generation, Equation 3.29 is useful to estimate the generator speed by measuring the dc load current and voltage, instead of using a speed sensor. More tests were done to evaluate the accuracy of numerically calculated dc voltage under different generator speed and dc load current, and results are plotted in Figure 4.16.

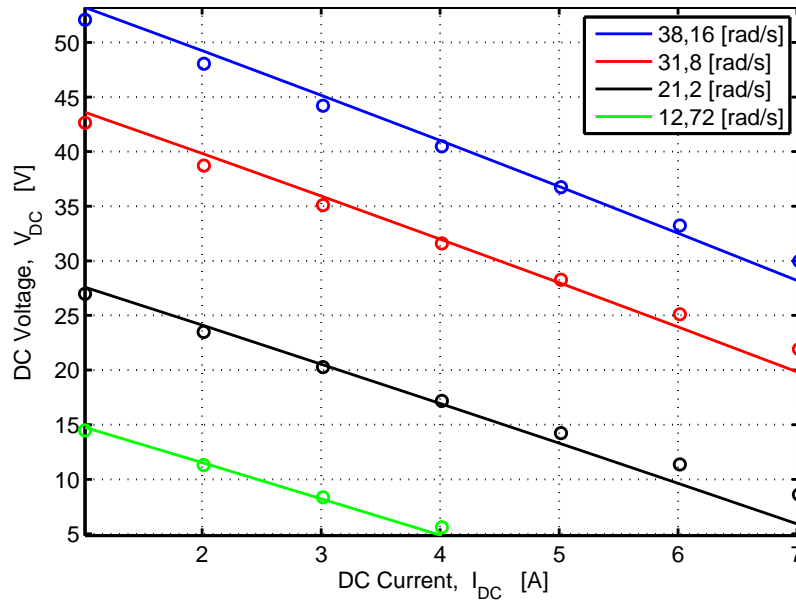


Figure 4.16: DC voltages with respect to the load current under different speed of PMSG. Solid lines represent the numerically calculated values by using DC equivalent model, the circles show the obtained test results and each color represents the correspondence working speed of the PMSG.

4.3.4.3 Torque constant of PMSG

it is necessary to estimate the generator torque which is proportional to the dc load current by a factor, namely the torque constant (K_t), as given by:

$$T_{gen} = K_t I_{dc} \quad [Nm] \quad (4.12)$$

In order to estimate the torque constant, the motor driven generator was loaded by drawing various dc currents, and measuring the corresponding motor torque. The torque loaded by the generator value was estimated from the difference of the motor torque and the torque required for friction. This test was repeated several times before and after running the motor, gear box and generator under high speed and load to sample data at different temperatures. As a result, the estimated PMSG torque values are plotted with respect to the dc current in Figure 4.17 and almost

a linear relationship is obtained.

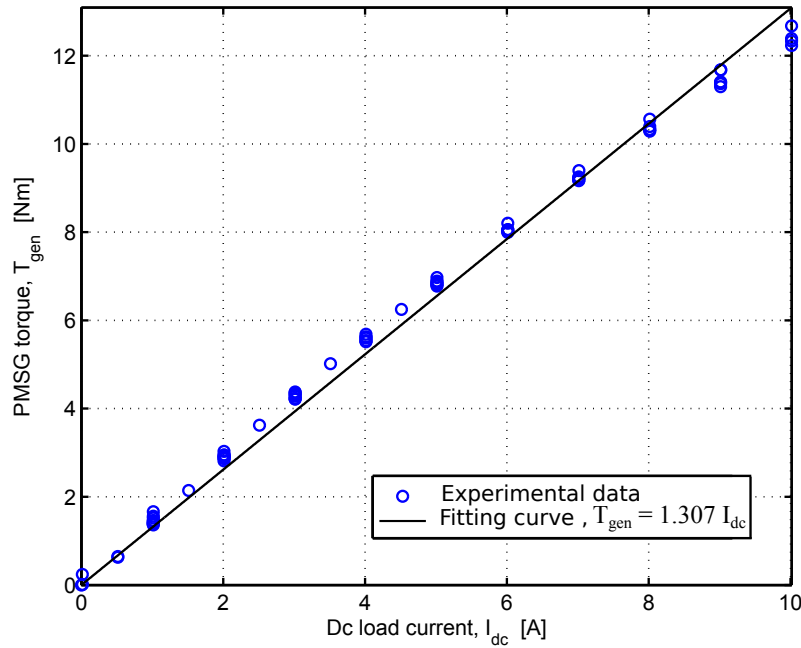


Figure 4.17: Estimated generator torque values with respect to the dc load current.

The validated parameters from experimental results are summarized in Table 4.5.

Parameter	Value	Used in/for calculation of ...
Number of pole pairs, p	6	$\omega_e = p\omega_{gen}$, and in simplified dc model
Equivalent inertia, J_e	$4.88 \times 10^{-4} \text{ kg.m}^2$	VAWT inertia emulation
Friction torque, $T_f(\omega_m)$	$T_f(\omega_m) = -1.418 \times 10^{-6}\omega_m^2 \dots$ $+1.327 \times 10^{-3}\omega_m + 0.175 \text{ Nm}$	VAWT inertia emulation, torque constant estimation
Line resistance, R_s	1.6 Ω	simplified dc model
Line inductance L_s	4.6 mH	
Flux, ϕ_s	0.1069 V.s/rad	open circuit line/phase voltage, and simplified dc model
Torque constant, K_t	1.307 Nm/A	$T_{gen} = K_t I_{dc}$
Threshold voltage for each diode, V_{th} [47]	0.77 V	Simplified dc model

Simplified dc model dc output voltage equation

$$V_{dc} = \sqrt{E_{sdc}^2 - (p\omega_{gen}L_{dc}I_{dc})^2} - (R_{dc} + R_{over})I_{dc} - 2V_{th}$$

for R_{dc} , L_{dc} and R_{over} , see Table 3.4

Table 4.5: Estimated and measured parameters of the PMSG and rectifier.

4.4 Inertia emulation

In this section, a methodology is presented for emulating the inertia of the actual VAWT rotor in the simulator. The objective is to emulate the inertia of the real VAWT rotor by using the similarity between the real system and the HIL system dynamics.

4.4.1 VAWT dynamic equations

The rotor dynamics of the VAWT system in Figure 4.1(a) is given by:

$$J_r \frac{d\omega_r}{dt} = T_{wind} - T_{gen} - T_{rf} \quad [Nm] \quad (4.13)$$

where J_r is the equivalent inertia of the rotor, T_{gen} is the generator torque on the rotor. T_{rf} is the friction of the rotor torque in the actual VAWT system, and it is assumed to be proportional to ω_r by a coefficient B as follows:

$$T_{rf} = B\omega_r \quad [Nm] \quad (4.14)$$

4.4.2 VAWT simulator dynamic equations

The same dynamic behavior that is modeled by Equation 4.13 can be mimicked by the equation of motion at the motor side in the VAWT simulator (see Figure 4.1(b)) for which the equation of motion reads:

$$J_m \frac{d\omega_m}{dt} = T_m - T_{load} \quad [Nm] \quad (4.15)$$

where T_m is the motor torque, ω_m is the rotational speed of the motor, J_m is the equivalent inertia at the motor side of the gear box. T_{load} is given in Equation 4.1, and it is re-called below with the motor-generator speed relation:

$$T_{load} = \frac{T_{gen}}{\Gamma} + T_{hf} \quad [Nm] \quad (4.16)$$

$$\omega_{gen} = \frac{\omega_m}{\Gamma} \quad [rad/s] \quad (4.17)$$

where T_{gen} is the generator torque, Γ is the gear ratio and T_{hf} is the friction torque, which corresponds to the overall friction in the VAWT simulator drive train including the gear box, generator and the motor. Assuming that the VAWT does not have a gear box and the generator is directly coupled to the rotor, the rotational speed of the actual VAWT rotor is the same as the rotational speed of the generator in the VAWT simulator, i.e. $\omega_r = \omega_{gen}$. Thus, the behavior of the VAWT system can be mimicked by the HIL simulator with the appropriate motor torque T_m , which is

applied as a reference torque in the HIL simulator and calculated from Equations 4.13, 4.14, 4.15, 4.16 and 4.17 as follows:

$$T_m = T_{load} + \frac{J_m \Gamma}{J_r} (T_{wind} - T_{gen} - T_{rf}) \quad [Nm] \quad (4.18)$$

The block diagrams of the VAWT system and the HIL system are given in Figure 4.18 where the motor is the actuator and used for mimicking the rotor dynamics in the HIL system. As it is shown in Figure 4.18 and from Equation 4.18, the load

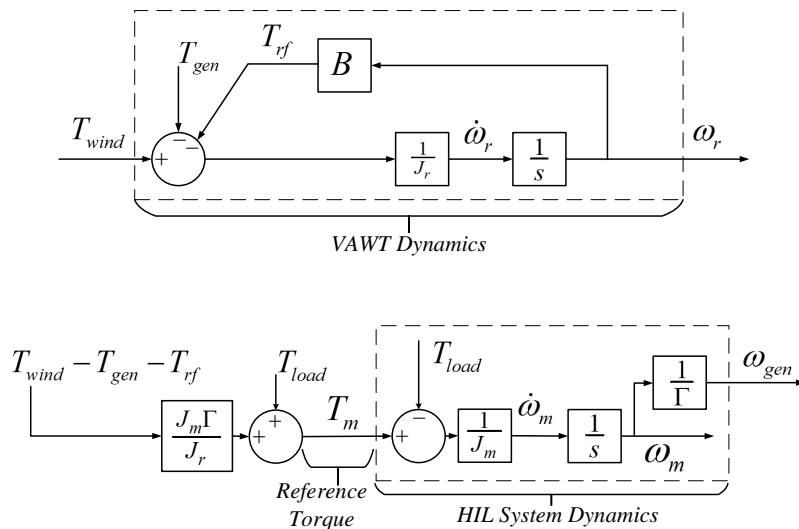


Figure 4.18: Block diagram of the VAWT dynamics, HIL System and reference motor torque calculation.

torque (T_{load}) is employed in the reference motor torque calculation, and it is calculated by using the generator torque (T_{gen}) and friction torque (T_{hf}) as in Equation 4.16. Consequently, if the generator and friction torques in the HIL system are known, a perfect cancellation of T_{load} can be achieved. Thus, the generator angular velocity, ω_{gen} , behaves in the same way as it does in the VAWT system. However, neither the generator nor the friction torques are easy to obtain precisely. For permanent magnet synchronous machines, there is a cogging torque, furthermore, the relation between the current and torque is not purely linear [36]. Furthermore, the nonlinear friction torque may lead to difficulties. Compensation for the friction torque can be achieved by model-based or non-model based methods as they are described in [49]. In the non-model-based compensation approach, the friction torque is treated as a disturbance for the system and can be compensated by the disturbance observer (DO) [50]. Derivatives of the angular velocity can be filtered in the DO to eliminate the noise, which affects the derivatives dramatically. A high gain low pass filter (LPF) provides a fast disturbance rejection performance. However, the motor in the VAWT simulator has a resolver to measure the speed, and it has

relatively large noise especially in the low speed operating ranges. This large noise amplitudes necessitate using a LPF with a low gain, and it introduces a delay in the system, which distorts the characteristics of the system. Hence, the disturbance torque cannot be fully compensated robustly. Several approaches to deal with this problem are proposed in literature: rapid disturbance changes in DO structures are discussed and a virtual plant model-based control is proposed to deal with disturbance torques in [51]; in addition to a virtual-plant disturbance compensator a friction-model-based feed-forward compensator is proposed in [52].

In this study, not only the friction torque, but also the deviations from the linear relationship between the torque and the current on the generator side and all other external effects are treated as disturbances. First, the friction torque model was obtained by fitting a curve to the load-free motor torque and speed measurements (see Figure 4.12). Then, the generator torque constant (K_t) was obtained (see Figure 4.17). Moreover, a virtual-plant model was used to obtain an error between the actual speed and the speed in the virtual-plant model. This error was used to generate the disturbance compensation torque by a proportional-integral (PI) based controller as shown with block diagrams in Figure 4.19, where the friction torque and the generator torque are calculated by a linear relationship while the deviations are handled by the disturbance compensation torque, T_{comp} . Especially for low speeds and high torques and during the start-up of the VAWT simulator, deviations are relatively higher than the nominal operation point of the motor, generator and gear box. The disturbance torque compensator (T_{comp}) ensures that the VAWT simulator mimics the VAWT system dynamics successfully.

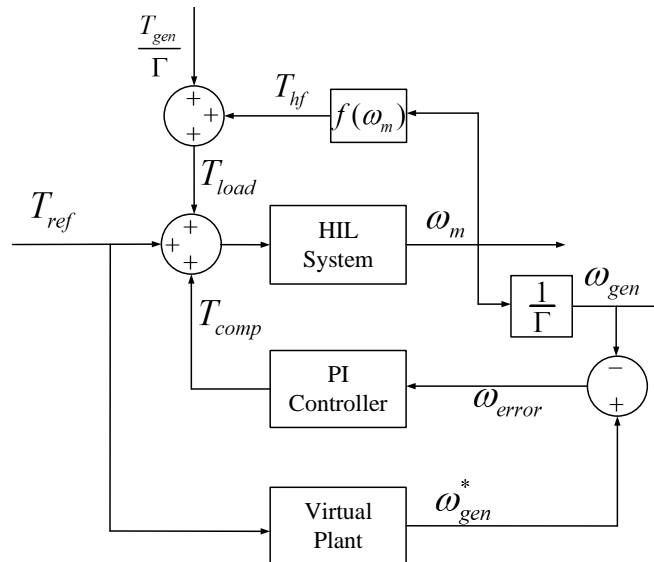


Figure 4.19: Model following controller with a PI based disturbance compensator structure in the HIL system.

As it is previously explained in Subsection 4.2.3.3 and shown in Figure 4.5, the

generator torque is set to a value proportional to the speed, $T_{gen} = 0.1\omega_{gen}$ with the purpose of observing the dynamic effects only. In Figure 4.22, the top plot shows the

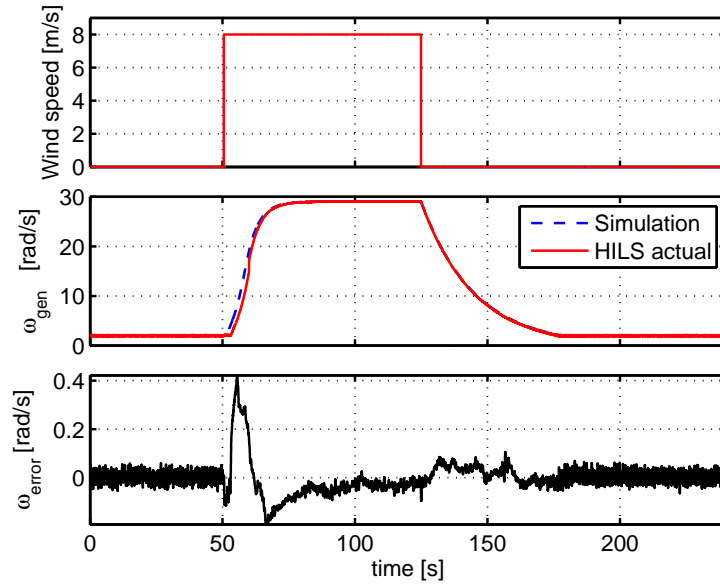


Figure 4.22: The comparison of HIL and numerical simulations rotational speed responses with 8 m/s step up and down speed. The initial speed of the VAWT rotor was set to 2 rad/s.

wind speed; the middle plot shows the generator speed obtained from the numerical and HIL simulation; the bottom plot shows the error in the speed, which is the difference between the speeds of the virtual plant and the measured speed in the HIL simulation. Results confirm that the VAWT simulator is capable of emulating the rotor inertia and mimics the overall VAWT system. Parameters of the PI controller are listed in Table 4.6.

Parameter	Value
Proportional gain, K_p	0.05
Integral gain, K_i	0.02

Table 4.6: Parameters of the PI-controller that is used to generate the disturbance torque compensator.

Chapter 5

Control

5.1 Introduction

Based on the $TSR - C_p$ curve of the studied VAWT (in Figure 2.2) which has an optimal TSR value that results in maximum aerodynamic power ($P_{wind,max}$) obtained from the VAWT, one can aim to find the maximum value of the power coefficient $C_{p,max}$, that corresponds to maximum aerodynamic power. However, the maximum electrical output power may not be maximized when the power losses are considered in the electromechanical part of the system. The aerodynamic power efficiency and the generator efficiency change with respect to torque and speed. Therefore, the control algorithm must ensure that the overall system operates at the optimum point.

The losses in electric machines can be divided into four categories; copper, core, friction and windage losses. Copper and core losses are the major sources of power loss in electrical machines. The copper loss is caused by the electrical resistances of the stator windings in the generator, and it is proportional to the square of the current. Since the electromagnetic torque in the PMSG is a function of the phase current in the generator, copper loss can be assumed to be proportional to the square of the torque. In addition to the copper loss, the core loss includes a hysteresis and eddy current loss which are proportional to the electrical frequency, and hence to the rotational speed. The friction at the bearing and rotor windage are relatively much smaller than copper and core losses, and have a smaller share in the overall power loss.

The total loss in the power and the active power output can be calculated by means of an elaborate model of the PMSG that considers the effects of the power converter. However, the complexity of such a model is outside the scope of this work, and the simplified dc model, which is presented in Section 3.2 is used to estimate the maximum available electrical output power in the VAWT system.

The dc load voltage (V_{dc}) is a function of the generator speed (ω_{gen}) and the dc load current (I_{dc}) as presented in Equation 3.29. Therefore, for each torque and speed pair, there is a unique pair of load current and voltage, I_{dc} and V_{dc} . The output power can be calculated by using the simplified dc model:

$$P_{out} = P_{dc} = V_{dc}I_{dc} \quad [W] \quad (5.1)$$

As an example, the wind power and the resultant wind torque curves are plotted in Figure 5.1 for the velocity of the wind equals to 8 m/s.

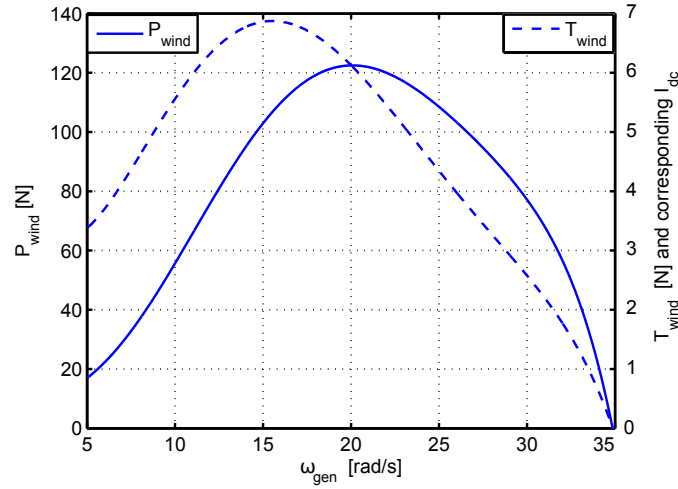


Figure 5.1: Wind power and resultant torque for 8 m/s wind speed at steady state. Left and right y-axis represent the wind power and torque respectively

In steady state, the rotor rotates with a constant speed and the wind torque is equal to the generator torque, $T_{wind} = T_{gen}$. This generator torque corresponds to a dc load current that is calculated from Equation 4.12. So, each operating point on the wind power curve corresponds to a current and rotor speed. The corresponding dc load current was calculated and plotted with respect to the rotor speed, and it is shown in Figure 5.2. Furthermore, the dc load voltage, which is a function of the dc current and the generator speed is also plotted in Figure 5.2.

Finally, the resultant output power (P_{dc}) was calculated from Equation 5.1 and it is depicted in Figure 5.3 with the wind power curve with respect to the rotor speed and 8 m/s wind speed. As it can be seen in Figure 5.3, the maximum output power ($P_{dc,max}$) realizes for different speed than the maximum wind power ($P_{wind,max}$). It is because the loss is relatively high in the low-speed/high-torque operating region for the PMSG, and hence $P_{dc,max}$ attains a maximum value for higher rotor speeds than the speed that corresponds to $P_{wind,max}$. Losses and the efficiency characteristics result in lower power output than the maximum available wind power.

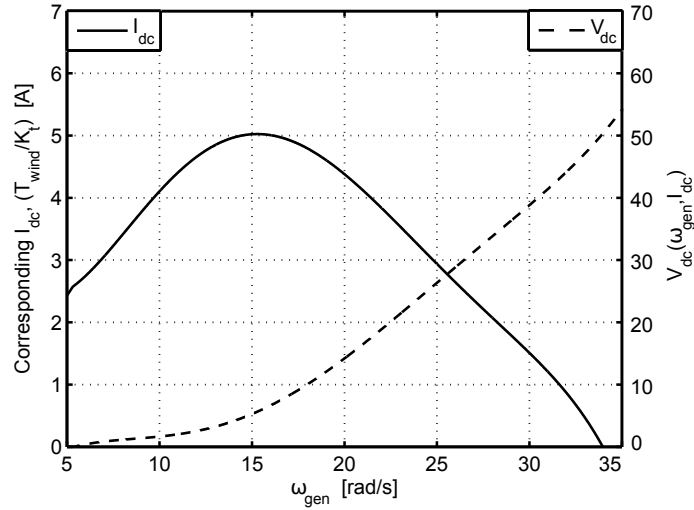


Figure 5.2: Corresponding dc load current and voltage under 8 m/s wind speed at steady state. Left and right y-axis represent the dc load current and voltage respectively.

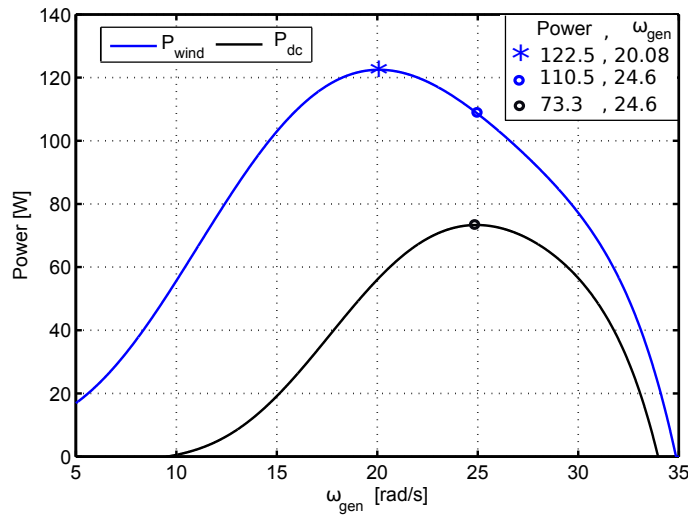


Figure 5.3: Wind power P_{wind} and electrical output power P_{dc} with respect to the rotor speed for 8 m/s wind speed.

Power curves for wind speeds varying between 1 and 14 m/s are plotted in Figure 5.4. A polynomial curve-fit for values of maximum power output varying with the wind speed is given by Equation 5.3.

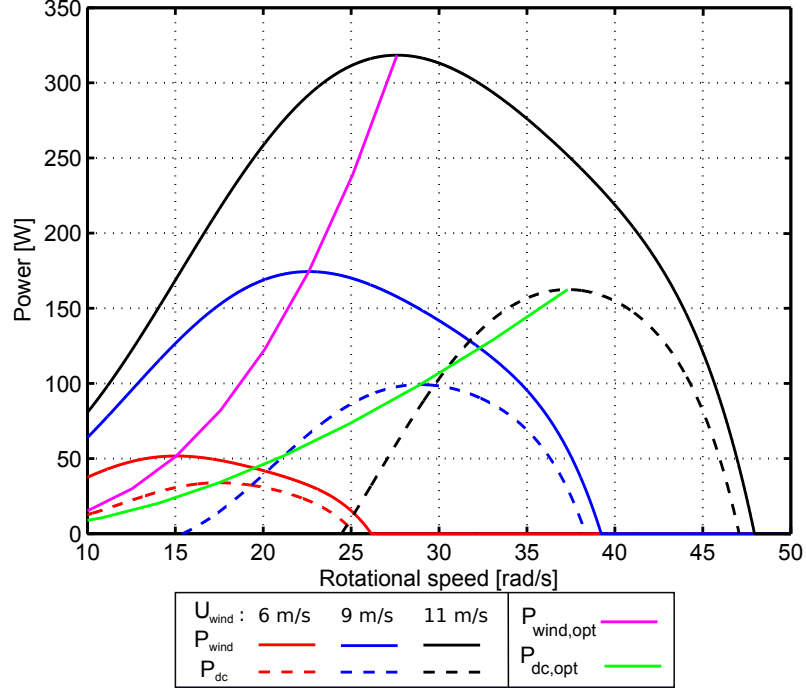


Figure 5.4: Wind power P_{wind} and electrical output power P_{dc} with respect to the rotational speed for three different wind speeds. $P_{wind,opt}$ and $P_{dc,opt}$ are the functions of wind speed that gives the maximum value of the wind and electrical output power respectively.

$$P_{wind,opt} = C_{p,max} R L \rho U_{wind}^3 = 0.2392 U_{wind}^3 \quad [W] \quad (5.2)$$

$$P_{dc,opt} = -0.004938 U_{wind}^4 + 0.1498 U_{wind}^3 + 0.3791 U_{wind}^2 - 0.9769 U_{wind} + 0.2355 \quad [W] \quad (5.3)$$

The relationship for the maximum power output as a function of the wind speed is used for the comparison of control algorithms, which is presented in the next section.

5.2 Control methods

Two types of control are studied: the maximum power point tracking (MPPT) and a simple non-linear control (SNC). One of the main objective of this thesis is to have a simple and low cost VAWT system, the MPPT approach offers a simple control that does not rely on wind or rotor speed measurements, which may increase the cost and reduce the reliability. Moreover, the MPPT algorithm is independent of the aerodynamic characteristics of the VAWT. As an alternative to MPPT, a simple non-linear control method developed in [53] was also studied here; the method relies on a simple model and the characteristics of the VAWT system.

5.2.1 Maximum power point tracking (MPPT)

In order to operate the system at the maximum power point, a control method was implemented based on the incremental MPPT algorithm [26], [31]. This type of MPPT algorithm does not require measurements of the wind velocity and the rotor speed. Incremental search for the optimum power output is based on the voltage and current measurements as it is described in [32]. The MPPT algorithm relies on the fact that the power output does not vary with voltage at the maximum point; i.e the derivative of the power with respect to the voltage is zero as it is expressed in Equation 5.4. The power output is plotted with respect to the dc output voltage for three different wind speeds in Figure 5.5

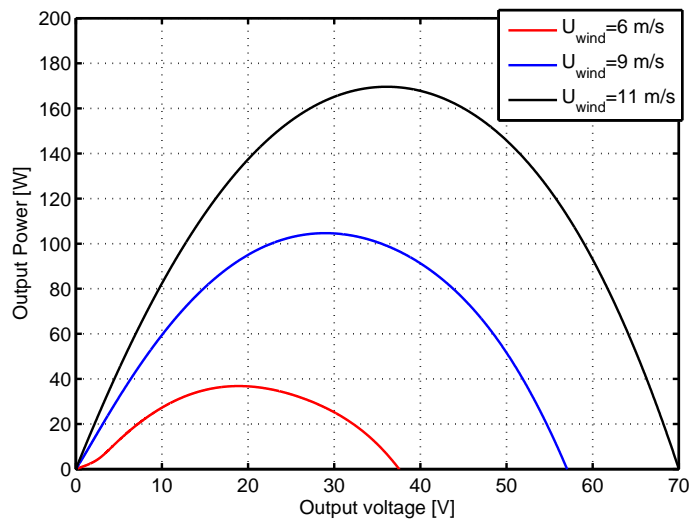


Figure 5.5: The output power (P_{dc}) with respect to dc voltage for 6, 9, 11 m/s wind speeds in steady-state.

$$\frac{dP_{dc}}{dV_{dc}} = \frac{d(V_{dc}I_{dc})}{dV_{dc}} = I_{dc} + V_{dc} \frac{dI_{dc}}{dV_{dc}} = 0 \Rightarrow \frac{dV_{dc}}{dI_{dc}} + \frac{V_{dc}}{I_{dc}} = 0 \quad (5.4)$$

According to Equation 5.4, relative change in the voltage must be positive if the relative change in current is negative at the maximum power point or vice versa. Therefore, the MPPT algorithm incrementally varies the current and compares with the change in the voltage to obtain the maximum power. The flowchart of the MPPT algorithm is presented in Figure 5.6.

The algorithm starts with measuring the dc voltage and the current, then it calculates the change in the voltage for a pre-set increment, $K > 0$, in the current. If the change in the voltage is positive, it continues to increase the current until the voltage change is zero or negative, otherwise it decreases the current until the maximum power is reached. The sampling period of the control unit, T_c , is an important parameter that influences the performance of the algorithm significantly.

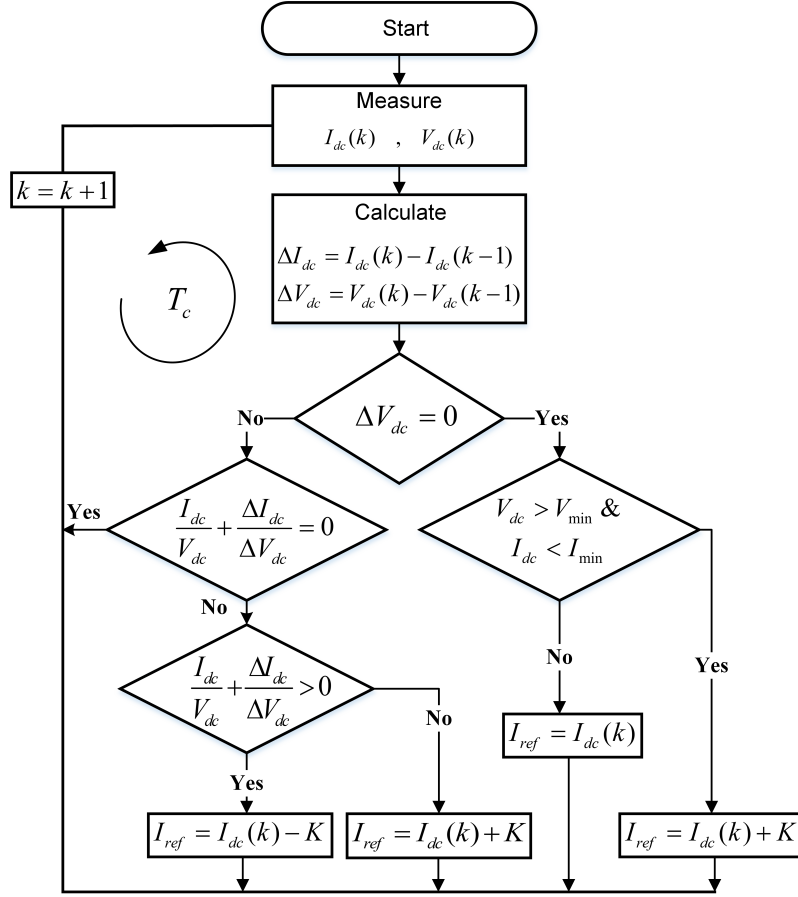


Figure 5.6: Flow chart of the MPPT algorithm.

A small value of T_c may cause the false detection of tracking direction, and a high value of T_c does not allow tracking the changes in the wind velocity appropriately. Furthermore, the size of the current increments affects the MPPT performance and determines the shape of the oscillations that appear in steady state around the maximum power point [26, 31, 54]. There is a trade-off between the amplitude of the oscillation around the optimum value and the convergence speed to the optimal value, i.e increasing K yields a slower convergence but the oscillations around the optimum value tend to be of higher amplitudes; decreasing the value of K reduce the convergence rate and the oscillations around the optimum value. Therefore, the step size of the current (K) and the sampling period (T_c) need to be tuned to obtain fast response and small fluctuations around the optimum operating conditions. For that purpose, a parametric study on the values K and T_c is presented in Section 6.1.1.

5.2.2 Simple non-linear control

This method controls the dc current by measuring the wind speed. To apply this control method, the power curve of the VAWT, characteristics of the generator and

power converter need to be known in order to generate a reference load current that keeps the rotor speed at the optimal level. In other words, system parameters need to be known with respect to the wind speed input.

Since the output power is the product of the dc voltage and the current, their optimal values for each wind speed input can be specified as it has been done for the optimal dc power, $P_{dc,opt}$ in Section 5.1 (see Equation 5.3). In the same manner, the optimal output voltage is expressed as a function of the wind speed with a polynomial fit as follows:

$$V_{dc,opt} = -0.001901U_{wind}^3 + 0.06806U_{wind}^2 + 2.736U_{wind} + -0.4088 \quad [V] \quad (5.5)$$

In this algorithm, the VAWT operating region is divided into 4 subregions depending on the dc voltage:

$$I_{dc} = \begin{cases} I_{dc,min}, & V_{dc} \leq V_{dc,min} \\ I_{dc,ref} - \frac{I_{dc,ref}}{V_{dc,ref} - V_{dc,min}}e, & V_{dc,min} < V_{dc} \leq V_{dc,ref} \\ I_{dc,ref} + \frac{I_{dc,ref}}{V_{dc,ref} - V_{dc,max}}e, & V_{dc,ref} < V_{dc} \leq V_{dc,max} \\ I_{dc,max}, & V_{dc} > V_{dc,max} \end{cases} \quad (5.6)$$

where, $e = V_{dc,ref} - V_{dc}$ is the error, i.e the difference between the reference dc voltage and instantaneous dc voltage. $I_{dc,max}$ is the maximum allowable current that can be drawn. Lastly, $V_{dc,min}$ and $V_{dc,max}$ are the limits of the output voltage that need to be tuned for optimal energy output. The proposed algorithm draws $I_{dc,min}$ if the dc load voltage is below the lower limit, and maximum current if the dc voltage is above the upper limit. A unity gain proportional control is applied when the dc voltage is between the limits.

The limits can be specified by considering the VAWT system output power characteristics and current-voltage constraints of the components:

- Cut-in wind speed can be defined as considering the maximum output power that will be sufficient to operate the system. As a result, cut-in wind speed was specified as 4 m/s since the maximum output power was calculated from Equation 5.3, and it is below 10 W this wind speed.
- If Equation 5.5 is solved for $U_{wind} = 4$ m/s, it can be seen that optimal dc voltage is 11.68 V. The minimum dc voltage value can be selected below 11.68 V, and it was specified by a parametric study discussed in future Section 6.2.1.
- If Equation 3.29 is solved for $U_{wind} = 12$ m/s that is the cut-out wind speed for the VAWT (see Table 3.3), it can be seen that the optimal output voltage is 38.95 V. The upper boundary needs to be selected over this voltage, and

it was specified by a parametric study discussed in upcoming Section 6.2.1. Note that the voltage boundary cannot be chosen over 60 V since it is the maximum allowable voltage for the electronic load.

- Lastly, $I_{dc,min}$ and $I_{dc,max}$ can be specified by solving the Equation 5.6 at the boundaries $V_{dc} = V_{dc,min}$ and $V_{dc} = V_{dc,max}$ respectively.

Chapter 6

Results

In this chapter, the applied MPPT and simple nonlinear control method results are presented. The step size of the MPPT and its sampling period are important parameters since they influence the resultant power output and its convergence ratio and oscillation. Similarly, the limits of the dc output voltage and sampling period of the simple nonlinear control method influence the total energy output of the system. Thus, parametric studies were done for both methods to analyze the effects of the parameters on the output power. The MPPT method and its parametric study results are given in Section 6.1 ; the simple non-linear control method and its parametric study results are given in Section 6.2; a comparison between two control methods is given in Section 6.3. Lastly, the generator parameters and their influence on the overall system efficiency are discussed in Section 6.4

6.1 Maximum power point tracking

The sampling time of the control unit (T_c) and the step size of the current (K) are the control variables in the MPPT algorithm, which is outlined in Figure 5.6. Fluctuations in the current and voltage near the optimal point are strongly influenced by the values of T_c and K . The value of the current step size affects the amplitude of the fluctuations around the maximum power point even at steady-state. A step-wise varying wind speed is constructed from 4 consequent step-up and down velocity profiles as shown in Figure 6.1. In order to observe the oscillations at steady state, the duration of constant wind speed time is kept sufficiently long. Finally, the wind velocity profile given in Figure 6.1 was applied in the HIL simulation by keeping one of the MPPT control variables (T_s or K) as a constant and changing the other, and vice versa.

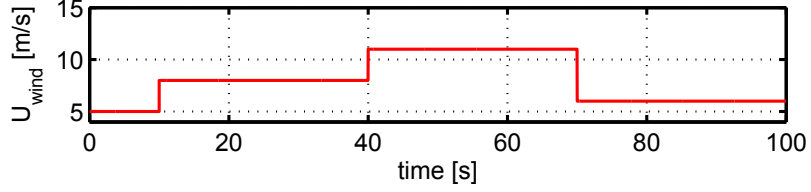


Figure 6.1: Applied wind velocity profile for parametric study of the MPPT. First ten seconds the wind speed is 5 m/s, then it steps up to 8 m/s, 11 m/s and down to 6 m/s in every 30 seconds respectively.

6.1.1 Parametric study

The first experiment was carried out by setting the current step size to 0.1 A and the sampling time to 0.1 s since the programmable electronic load can handle the writing-query-reading sequences the fastest in 0.1 s in safe as it is discussed in Subsection 4.2.3.6. According to [26], the rotor inertia affects the time constant of the system and has an effect on specifying the sampling time of the control unit. The first experiment of the parametric study was labeled as mppt.1 while the other following experiments were named as mppt.2, 3 and so on.

Experiment no	Sampling period	Current step size	Energy
mppt.1	0.1 s	0.1 A	7.515 kJ
mppt.2		0.2 A	7.102 kJ
mppt.3		0.5 A	7.035 kJ
mppt.4	0.2 s	0.1 A	7.750 kJ
mppt.5		0.2 A	7.786 kJ
mppt.6		0.5 A	8.017 kJ
mppt.7		0.8 A	8.045 kJ
mppt.8		1.0 A	8.013 kJ
mppt.9	0.5 s	0.5 A	6.552 kJ
mppt.10		0.8 A	6.363 kJ

Table 6.1: Influence of the control unit sampling time and current step size to energy output in HIL simulation in which mppt control unit operates.

The results in Table 6.1 are interpreted below with a clause for each experiment group.

- For mppt.1, 2 and 3: increasing the current step size decreases the obtained energy output. Thereby, pushing the current step size further than 0.5 A in case of $T_c = 0.1$ s was found unnecessary.
- For mppt.4, 5, 6, 7 and 8: an increase in the current step size generally tends to elevate the obtained energy output. This effect is more apparent in the results mppt.7, 6 and 8, which yield the first, second and third best energy outputs respectively. These values would have been slightly changed if the experiments were repeated under the same conditions since variations in the

noise and friction affect the output power, and it results in slightly different energy output calculated over the duration of the experiment, which is 100 seconds. However, it has been seen that mppt.6, 7 and 8 always outperform the others with respect to energy output. Furthermore, when the experiments are repeated, the energy output difference between mppt.6, 7 and 8 changes by 10 to 40 joules due to aforementioned reasons. Although all three configurations ensue very close energy outputs, mppt.7 seems to be the most favorable for the MPPT implementation (see Table 6.1). Nevertheless, mppt.6, 7 and 8 power outputs with respect to time were depicted to closely examine their behavior. In this way, a selection can be done by considering the tracking-oscillation of the power output represented in Figure 6.2.

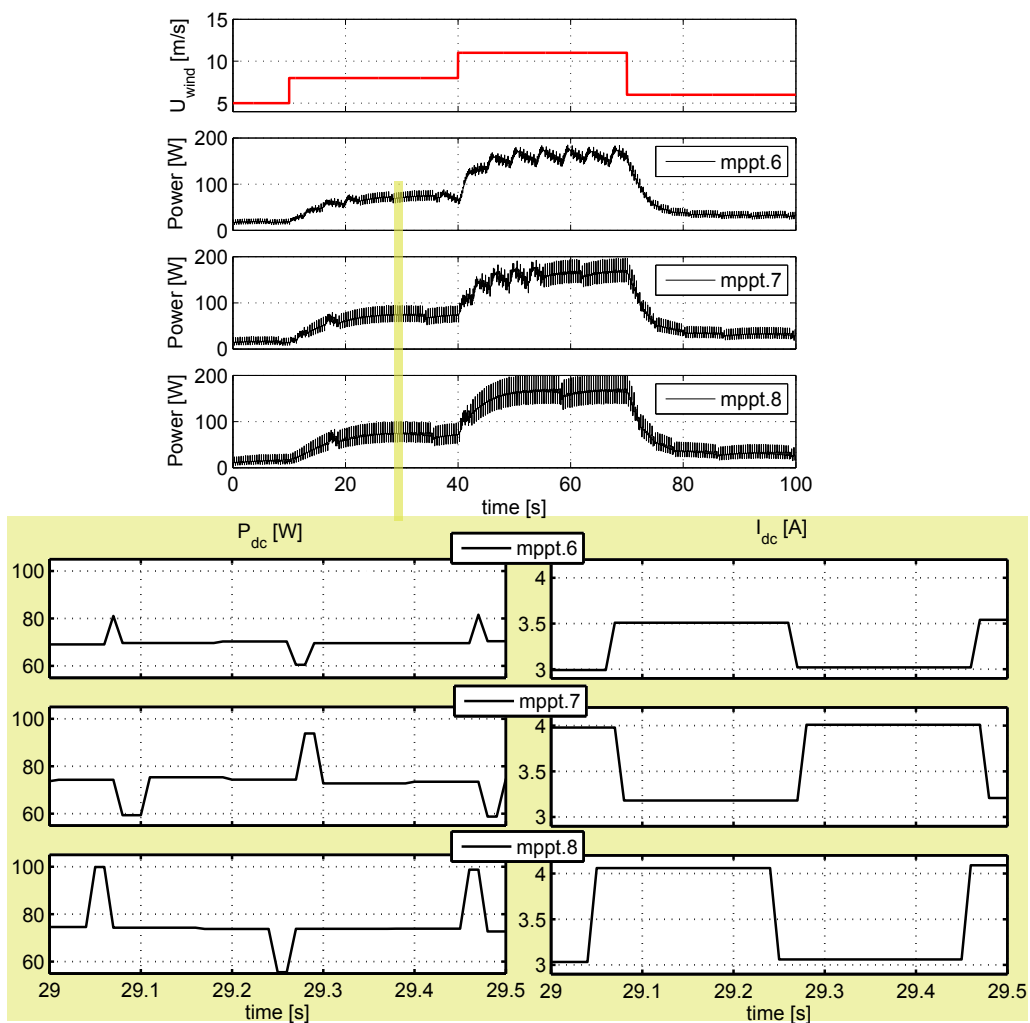


Figure 6.2: Output power results of experiment mppt.6, 7 and 8. The power and the current values are depicted with respect to the time over a shorter time in bottom left and right plots respectively.

As it can be seen from Figure 6.2, the behavior of the power output for the same wind velocity profile is more or less the same. However, higher current

step size results in higher oscillation around the maximum power point, and oscillations around the optimum point is unavoidable with the constant step size controlled variable. Once the controlled parameter, namely, the dc-load current (I_{dc}) converges to the neighborhood of the optimal point, it starts to oscillate around it, and it causes a fluctuating output power. The amplitude of the output power for mppt.6, 7 and 8 are 20, 34 and 44 Watts respectively. As a result, mppt.6 was preferred since it operates with the lowest fluctuation amplitude compared to mppt.7 and 8.

- For mppt.9 and 10: sampling period of the control unit is 0.5 s and it goes without saying that this results slow down the maximum power point tracking, and the total obtained energy underperforms with these parameters.

6.1.2 HIL simulation results for MPPT

Firstly, the MPPT algorithm has been tested in the HIL simulation for step up, down and sinusoidal wind velocity profiles. An arbitrary wind profile was formed as depicted in Figure 6.3. This wind velocity profile is a combination of step up, down and sinusoidal functions in sequence and wind velocity values with their durations are listed in Table 6.2. HIL simulation results for this wind profile was divided into two sections for interpretation: the first section is the step-up and down in the wind velocity; and the second one is between the 180th and 300th seconds of the simulation time as it consists of sinusoidal wind velocity with two different frequency. Results of these sections are presented in Section 6.1.2.1 and 6.1.2.2 separately. Lastly, the MPPT algorithm was tested with a realistic wind profile for which the results are presented in Section 6.1.2.3.

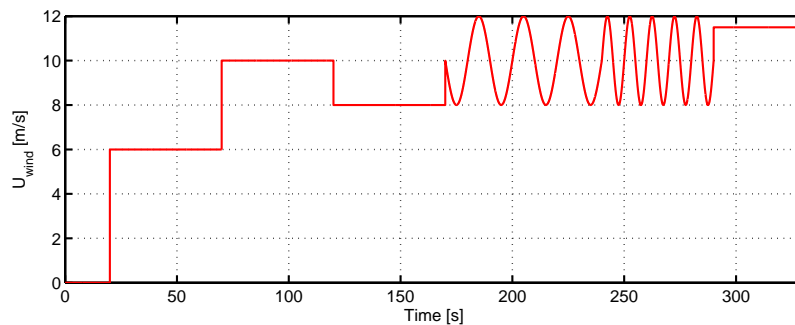


Figure 6.3: Applied wind velocity for testing the MPPT algorithm in HIL simulation.

In all cases the rotational speed of the generator is set to a low value as 2 rad/s initially. When the VAWT simulator is started, generator spins with 2 rad/s even though the wind velocity is to zero. The initial speed is set to such a small value to overcome the static friction or the stall torque of the gear-box during the start-up for all the HIL simulations.

Time [s]	Wind velocity [m/s]
0 - 20	0
20 - 70	6
70 - 120	10
120 - 170	8
170 - 240	$10 + 2 \sin(2\pi 0.05t)$
240 - 290	$10 + 2 \sin(2\pi 0.1t)$
290 - 330	11.5

Table 6.2: Applied wind velocity values and durations for the MPPT algorithm testing in the HIL simulation.

6.1.2.1 Step-response

The MPPT algorithm was tested for a step change in the wind velocity shown in the top plot of Figure 6.4. The values of the wind velocity and durations are the same as given in Table 6.2 in the first 170 seconds. Corresponding plots for the rotor speed (ω_r), electrical output power (P_{dc}), dc current (I_{dc}) and dc voltage (V_{dc}) are also shown in Figure 6.4. The dc power output agrees well with the estimated steady state optimal power ($P_{dc,opt}$) calculated from Equation 5.3. Fluctuations due to the MPPT algorithm are present in both the current and the voltage.

The value of the $P_{dc,opt}$ represents the estimated optimal dc power output and it is a function of the wind speed as it is calculated from Equation 5.3. The measured dc voltage may has slightly different values than the estimated ones from the simplified dc model (voltage differences are in a band of ± 1 volts for the nominal working range of the generator) in Table 4.4. These small deviations also cause deviations in the steady-state optimal dc output power ($P_{dc,opt}$) estimation, since it is the product of the dc voltage and current as shown in Figure 6.4. However, the error in the dc voltage estimation cannot cause large oscillations as we observe here. The existing oscillations are actually because of the controlled parameter, namely the dc current. In the HIL simulation, the MPPT algorithm generates a reference current to track its optimal value. However, tracking the reference current does not stop at the optimum value, and continues with overshoots and undershoots due to the measurement noise and constant step size of the current. See the Figure 6.4, between the 80th and 120th seconds of the experiment, P_{dc} oscillates in sawtooth-shape signal and periodically reaches higher power values than P_{opt} . During this time, the reference current, and also the load torque rises up; this leads to the extracting of the energy stored in the inertia, hence higher instantaneous power outputs than the theoretical maximum values are observed. In other words, if the current would stop at its optimum value in steady state, a constant rotor speed would be obtained. But, since the reference current generated by the MPPT continues to increase after reaching to the maximum point, generator torque acting on the rotor increases and it causes a decrease of the rotor speed. This oscillatory tracking is more visible for the current, rotor speed

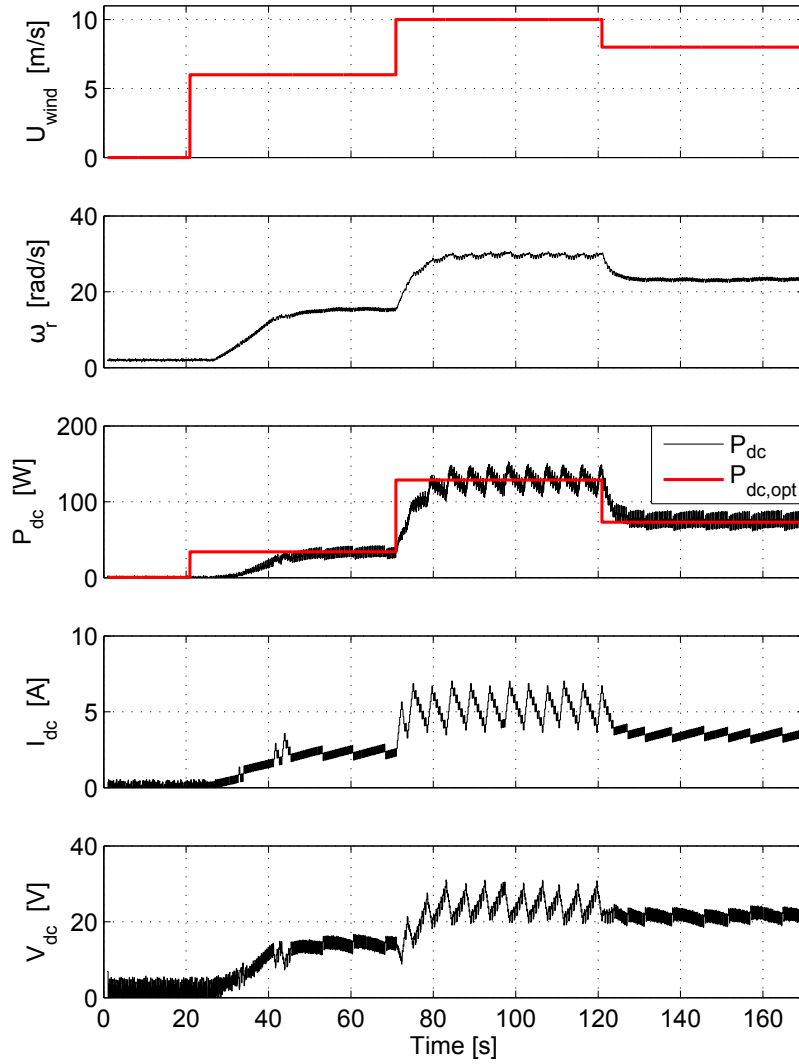


Figure 6.4: HIL simulation results for the step up and down wind velocity.

and output power between the 80th and 120th seconds of the simulation time than the other durations of the experiment.

Lastly, the generator spins at 2 rad/s as the preset initial value. Therefore, the induced voltage in the generator charges the capacitor while the load tries to discharge it during the first 20 seconds of the simulation.

6.1.2.2 Sinusoidal response

The MPPT algorithm was tested for sinusoidal wind velocity with frequencies of 0.1 Hz and 0.05 Hz, and the results are presented in Figure 6.5. The applied wind velocity values and durations are the same as the ones given in Table 6.2 in between 180 and 300 seconds.

The results indicate that the dc output power follows the estimated optimal dc value closely. The MPPT algorithm leads to a phase difference between the wind and power output signals.

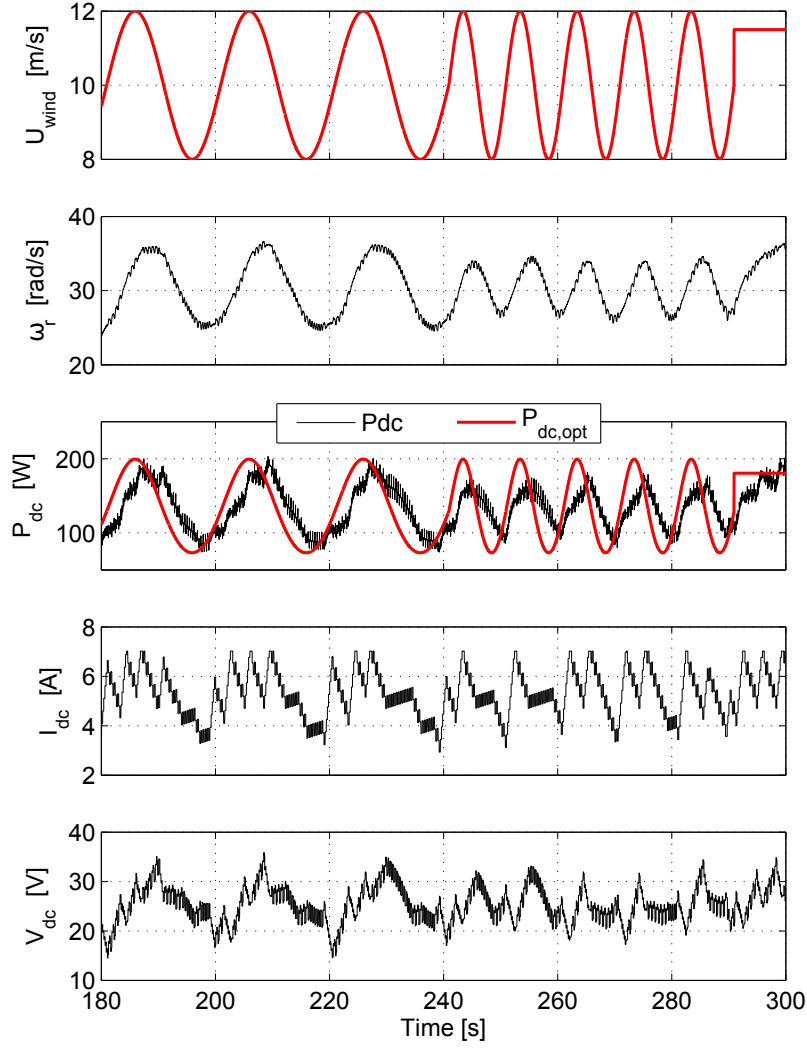


Figure 6.5: HIL simulation results for the sinusoidal wind velocity.

6.1.2.3 Response to realistic wind data

The realistic wind data is taken from Koutroulis and Kalaitzakis's study [55]. The mean value of the wind speed taken from [55] is below 4 m/s. However, the VAWT system in this project was designed to operate at higher wind velocities, and its cut-in and rated wind velocities are 4 m/s and 8 m/s. Furthermore, in [35], the average wind speed is given between 6 and 7 m/s for the place where the real VAWT is established (in Istanbul). Therefore, 2 m/s wind velocity offset was added to the wind data from [55] in order to obtain a reasonable mean value of the wind speed for the designed VAWT. Resulting wind velocity profile with a mean value of 6.34 m/s is shown in Figure 6.6.

According to Figure 6.6, the dc output power follows the estimated optimal dc power with oscillations. As observed in other cases, fluctuations are present in the power output. Taking into account the fact that the realistic wind velocity profile is constructed from many alternating ramp functions, it can be concluded

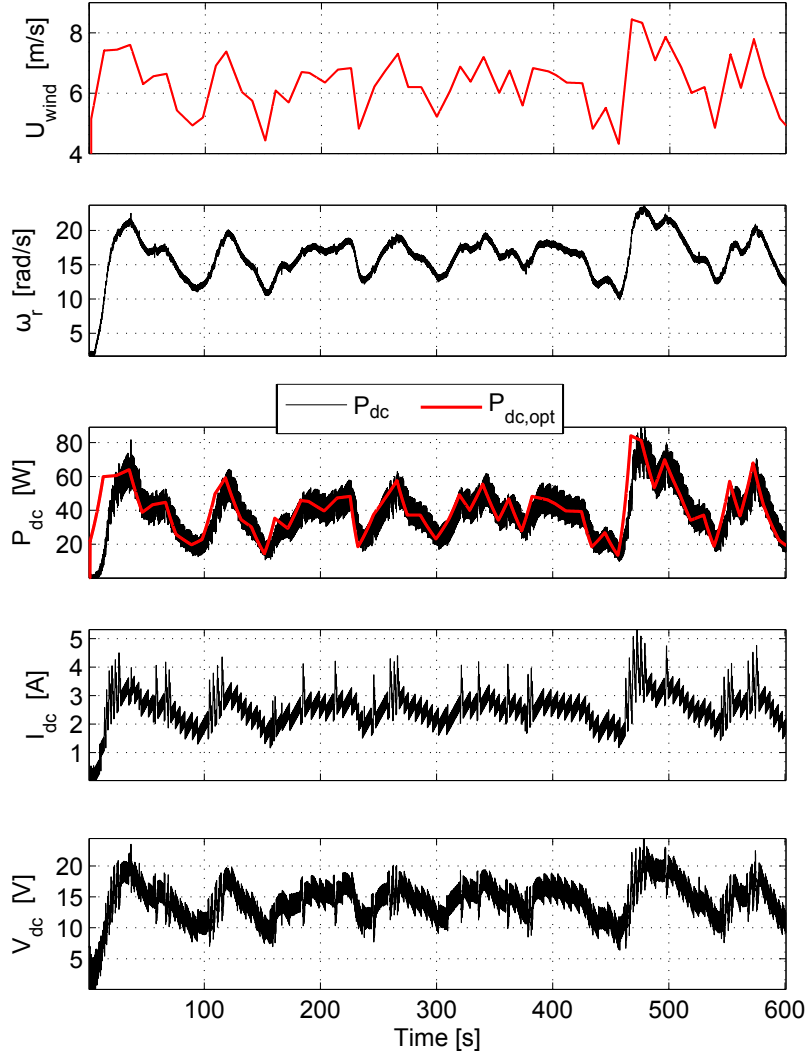


Figure 6.6: HIL simulation results for the realistic wind velocity. Note that the wind velocity starts from 0 m/s.

that MPPT algorithm performs better with ramp-like wind velocity profile in terms of convergence ratio and phase shift as compared to the sinusoidal one.

6.2 Simple nonlinear control

The minimum and maximum value of the dc voltage, $V_{dc,min}$ and $V_{dc,max}$, are the control variables of the simple non-linear control and need to be set to such values that will operate the system with maximum energy output and minimum oscillation. To this end, a step up and down wind velocity profile represented in Figure 6.1 was applied in the HIL simulation by keeping one of the control variables ($V_{dc,min}$ or $V_{dc,max}$) as a constant and changing the other, and vice versa.

6.2.1 Parametric study

The parametric study was carried out by considering the estimated optimum dc voltage values calculated from Equation 5.5 for the cut-in and cut-out wind velocities. Figure 6.7 shows the power plots with respect to the output voltage for the cut-in, cut-out and rated wind velocities, i.e $U_{wind} = 4, 12$ and 8 m/s. The dc voltage and power output were estimated from the simplified dc model with an expected error as depicted in Figure 6.7. The estimated optimum dc voltage values for cut-in

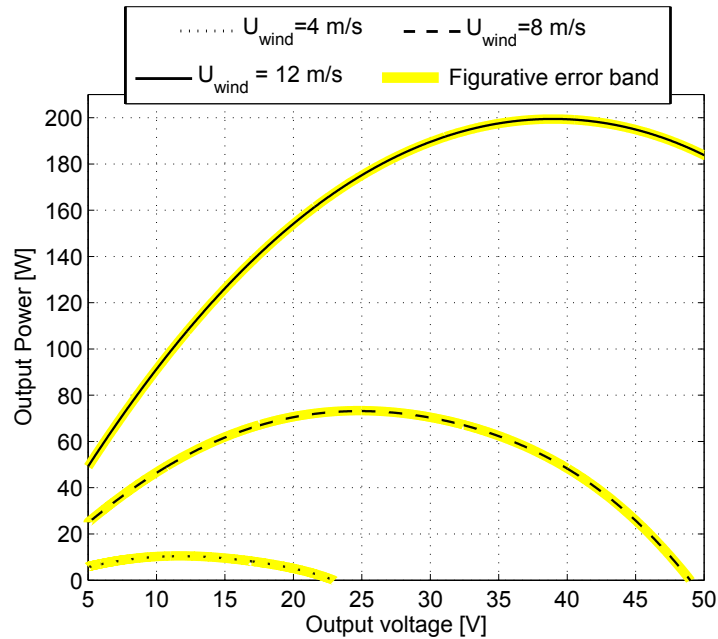


Figure 6.7: The output power curves with respect to the dc load voltage.

and out wind velocities, i.e 4 and 12 m/s, are 11.68 V and 38.95 V respectively. Therefore, the maximum and minimum threshold voltages (V_{min} and V_{max}) as the simple non-linear control variables need to cover this range. The first experiment was carried out for V_{min} and V_{max} values of 5 V and 60 V as denoted with snc.1 in Table 6.3, where the other cases are listed as well.

Experiment no	V_{min}	V_{max}	Energy
snc.1	5 V	60 V	8.490 kJ
snc.2		50 V	8.453 kJ
snc.3		45 V	8.495 kJ
snc.4	10 V	60 V	8.459 kJ
snc.5		50 V	8.451 kJ
snc.6	15 V	60 V	8.419 kJ
snc.7		50 V	8.225 kJ

Table 6.3: Influences of the minimum and maximum voltage threshold values in simple non-linear control to the total energy obtained.

According to Table 6.3, the total energies obtained from experiments are close

to each other. These energy outputs were calculated over 100 s with the applied wind velocity profile given in Figure 6.1. Results for snc.1, 2 and 6 are depicted in Figure 6.8.

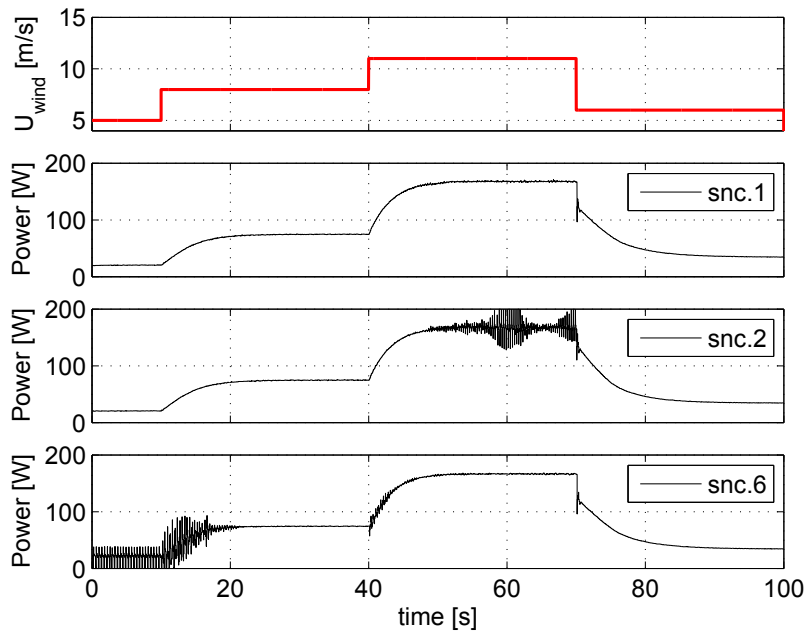


Figure 6.8: Output power results of experiment snc 1,2, and 6.

According to the parametric study, the lowest oscillatory power output was observed for snc.1 which has the lowest V_{min} and highest V_{max} values compared to the others. To account for the fluctuations in Figure 6.8, Equation 5.6 is recalled here with an illustrative power curve shown in Figure 6.9.

Notice that $V_{dc,ref}$ and $P_{dc,opt}$ are represented in Figure 6.9 with a possible error gap ($\pm\epsilon$). Assume that the sampled dc voltage (V_{dc}) is between $V_{dc,ref}$ and $V_{dc,min}$. In this case, V_{dc} needs to be increased to $V_{dc,ref}$ by decreasing the load current (I_{dc}) to generate higher output power. To this end, the controller sets I_{dc} to a value calculated from the controller rule equation, i.e in this case it is: $I_{dc,ref} - \frac{V_{dc,ref} - V_{dc}}{V_{dc,ref} - V_{dc,min}} I_{dc,ref}$. Once the adjusted I_{dc} is less than its reference ($I_{dc,ref}$), the generator speed increases as well as the dc voltage. In consequence of this, V_{dc} gradually gets closer to its reference value. Eventually, when V_{dc} comes up to its reference ($V_{dc} = V_{dc,ref}$), error term becomes zero and the controller sets the I_{dc} to its reference value. In the ideal case, when the reference parameters are estimated with no error, drawing $I_{dc,ref}$ would lead to the obtaining of the exact value of $V_{dc,ref}$, and there would be no oscillation. However, due to the error margin of the simplified dc model, entering I_{ref} as the input yields a voltage marginally different from $V_{dc,ref}$. Therefore, the dc current may not cease at its reference value, and oscillate during the operation. Thereby, the resultant voltage and power keeps oscillating. If the minimum and maximum value of the voltage thresholds ($V_{dc,min}$

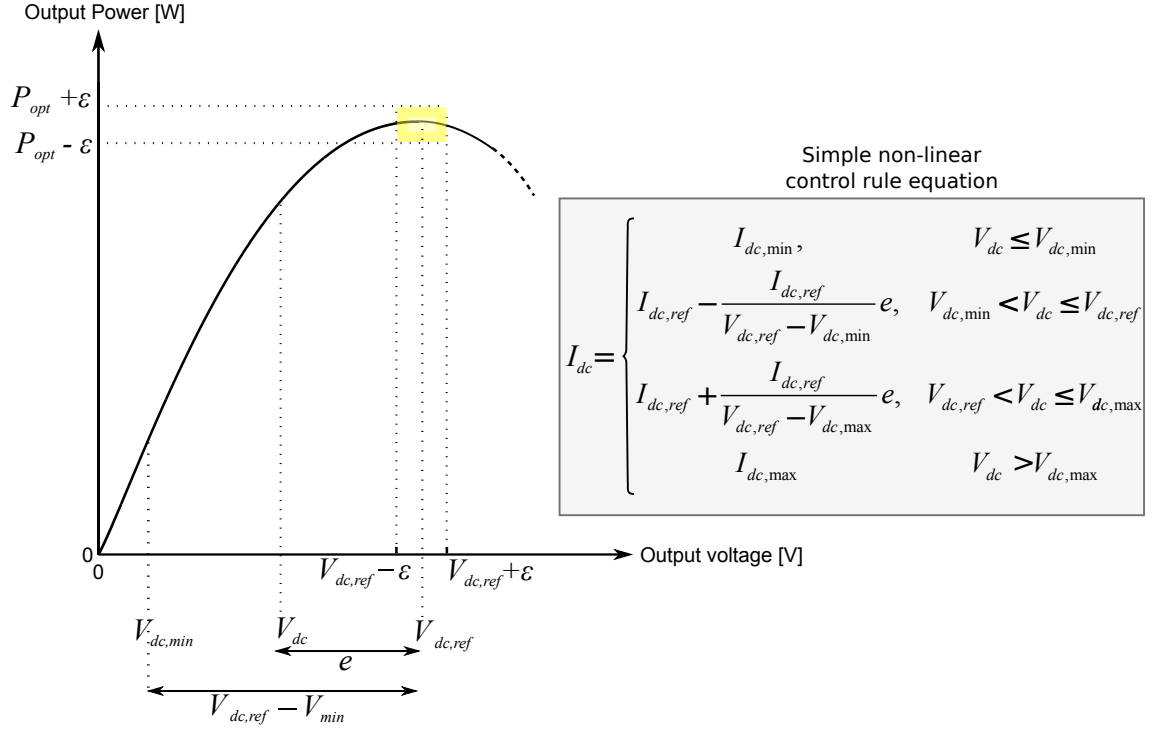


Figure 6.9: Representative power curve illustration and simple non-linear control rule equation for explanation of the output power oscillations due to the estimated voltage and power with a margin of error ϵ .

and $V_{dc,max}$) range is selected relatively high, it may help to suppress the error that comes from the estimated reference value deviations with respect to their right value since $V_{dc,ref} - V_{dc,min}$ or $V_{dc,ref} - V_{dc,max}$ are at the denominator of the controller rule equations (See the Equations 6.1 and 6.2).

$$I_{dc} = I_{dc,ref} - \frac{e}{V_{dc,ref} - V_{dc,min}} I_{dc,ref} \quad (6.1)$$

or

$$= I_{dc,ref} + \frac{e}{V_{dc,ref} - V_{dc,max}} I_{dc,ref} \quad (6.2)$$

As a result, $V_{dc,min}$ and $V_{dc,max}$ values were selected as 5 and 60 V since they suppress the error, that causes oscillation, comes from the reference voltage and current estimation and noise at signal level.

6.2.2 HIL simulation results for simple non-linear control

Under this subsection the power output, rotational speed, dc voltage and current results of the simple non-linear control HIL simulation are investigated closely for step-up and down, sinusoidal and realistic wind velocity.

6.2.2.1 Step response

The simple non-linear control algorithm was tested for a step change wind velocity shown in the top plot of Figure 6.10. The applied wind velocity values and durations are the same as given in Table 6.2 in the first 170 seconds. Corresponding plots for the generator (VAWT rotor) speed (ω_r), electrical output power (P_{dc}), dc load current (I_{dc}) and dc voltage (V_{dc}) are also shown in Figure 6.10.

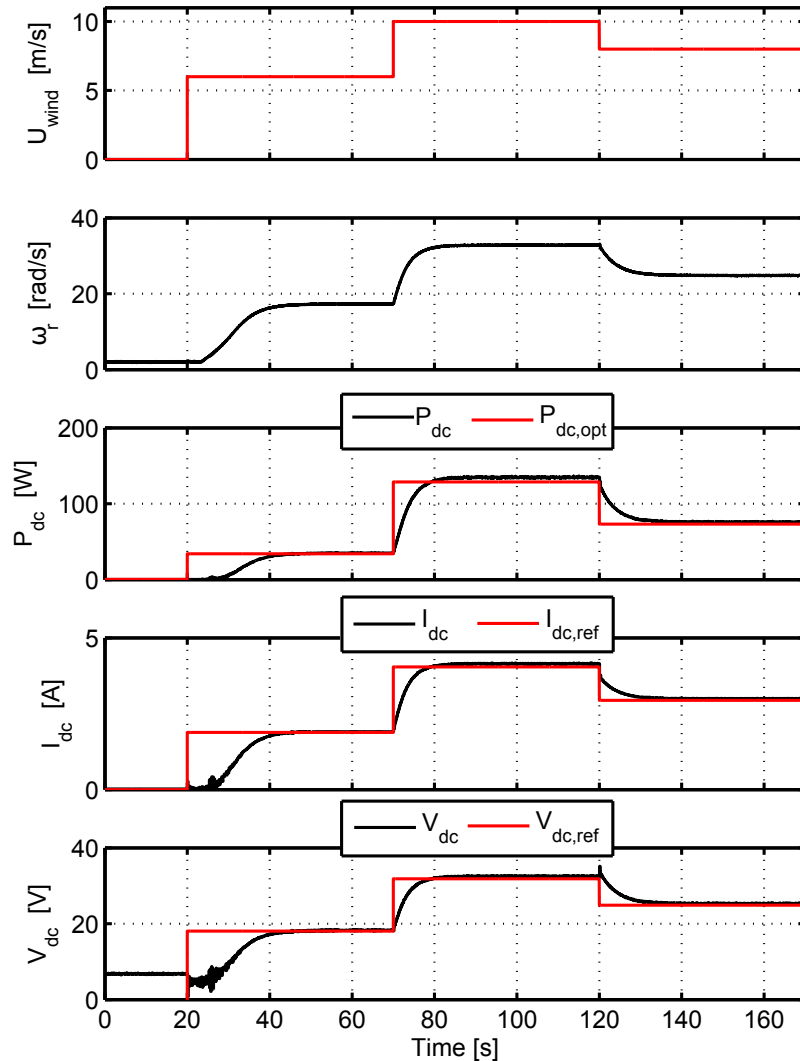


Figure 6.10: HIL simulation results for the step up and down wind velocity.

According to Figure 6.10, the dc output power trajectory agrees well with the estimated steady state optimal power ($P_{dc,opt}$) calculated from Equation 5.3. For the step wind speed change from zero to 6 m/s, the rotor speed starts to increase and reaches up to 17 rad/s in 20 seconds. For 6 m/s wind speed, there is no oscillation observed and obtained output power agrees well with the estimated optimal power behavior in steady state. Furthermore, for 11 m/s wind speed (between 80th and 120th seconds), P_{dc} is observed higher than the estimated optimal dc power ($P_{dc,opt}$), because of the error margins of the used simplified dc model and equations derived

from the model. However, this error margin is acceptable and the results are satisfactory. Furthermore, except the start-up, there is no oscillation on both current and voltage, and hence the resultant power. Lastly, the wind speed steps down to 8 m/s from 11 m/s at 120th second, and rotor speed drops from 32.8 to 24.8 rad/s in 15 seconds, and output power agrees well with the estimated power for 8 m/s wind speed as well.

As previously mentioned, the generator spins at 2 *rad/s* as the set initial speed due to aforementioned reasons in Subsection 6.1.2. Thereby, the induced voltage in the generator keeps the capacitor voltage just below 7 V during first 20 seconds. Thus, the dc voltage value, which would be zero with the zero wind speed and non-spinning VAWT rotor in real situation, can be disregarded by keeping the initial speed of the VAWT simulator in mind.

6.2.2.2 Sinusoidal response

The simple non-linear control was tested for sinusoidal wind velocity with frequencies of 0.1 Hz and 0.05 Hz, and the results are presented in Figure 6.11. The applied wind velocity and durations are the same as given in Table 6.2 in between 180th and 300th seconds.

The results indicate that the dc output power and numerically estimated optimal dc power (P_{dc} and $P_{dc,opt}$) agree well. The controller algorithm leads to a power generation with a phase difference between the wind and power output signals. Especially for the wind velocity with 0.05 Hz frequency applied at between 180th and 240th seconds, dc power shape is a upper clipped sinusoidal-like signal. It is because of the nature of the equations of the controller: imagine the dc reference voltage ($V_{dc,ref}$) is higher than the sampled dc voltage (V_{dc}) and a constant value of the reference current is generated. The controller makes the load draw a lower current than the $I_{dc,ref}$ and increases gradually up to $I_{dc,ref}$. In this case, it is possible to see the gradual increase of the current and voltage. When it comes to periodic signals, this would be different. See the controller law equation (Equation 5.6) and consider the cases that V_{dc} is between V_{min} and V_{max} and higher or lower than V_{ref} . In that cases, $I_{dc,ref}$ is calculated from the following equations:

$$V_{dc,min} < V_{dc} \leq V_{dc,ref} \Rightarrow I_{dc} = I_{dc,ref} - \frac{e}{V_{dc,ref} - V_{dc,min}} I_{dc,ref} \quad (6.3)$$

$$V_{dc,ref} < V_{dc} \leq V_{dc,max} \Rightarrow I_{dc} = I_{dc,ref} + \frac{e}{V_{dc,ref} - V_{dc,max}} I_{dc,ref} \quad (6.4)$$

Occasionally, it is possible to see the calculated I_{dc} value is constant when $V_{dc,ref}$ is higher than V_{dc} , and both $I_{dc,ref}$ and $V_{dc,ref} - V_{dc}$ decrease. It is also possible to see

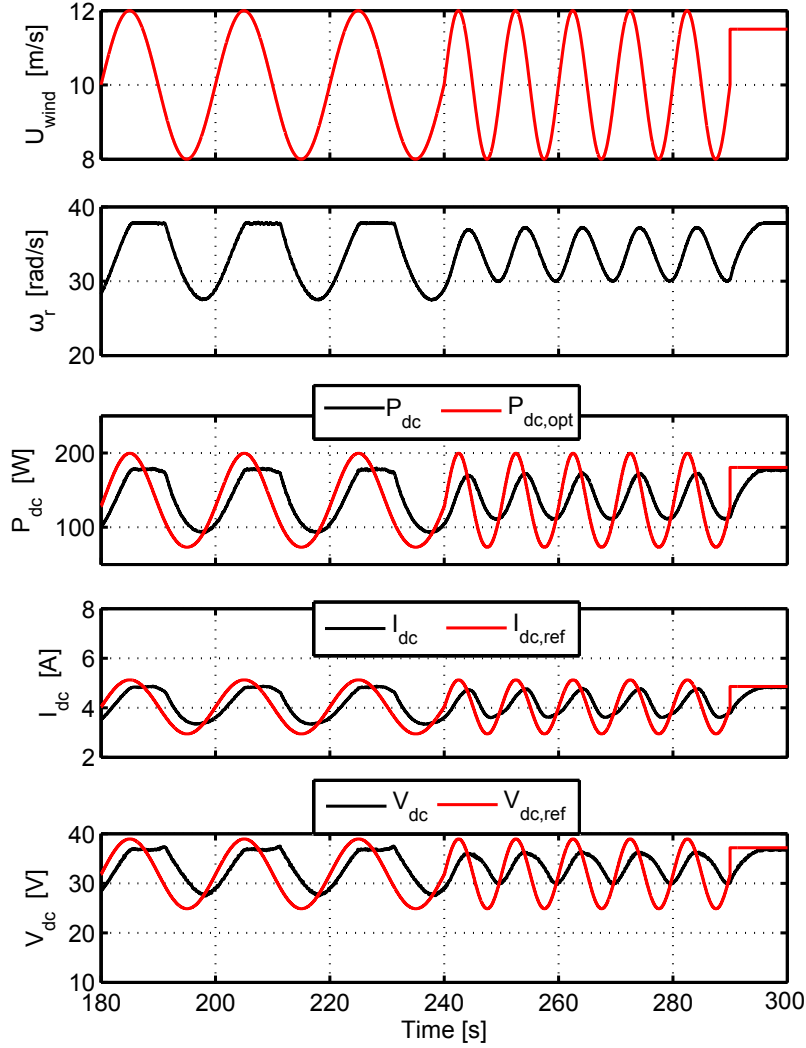


Figure 6.11: HIL simulation results for the sinusoidal wind velocity.

the calculated I_{dc} value keeps constant or slightly change when V_{dc} is higher than $V_{dc,ref}$, and both $I_{dc,ref}$ and $V_{dc,ref}$ decrease.

6.2.2.3 Response to realistic wind data

The same wind profile as used in Subsection 6.1.2.3 is used for testing the performance of the simple non-linear control performance for the realistic wind profile.

According to Figure 6.12 results, the obtained dc output power agrees well without oscillating with the estimated optimal dc power. Except the sharp changes on the wind velocity, the output power meritoriously follows the estimated steady state optimal power curve, and it does not oscillate. Taking into account the fact that the realistic wind velocity profile is constructed from many alternating ramp functions, it can be concluded that simple non-linear control algorithm performs better with ramp-like wind velocity profile as compared to the sinusoidal one. When the wind

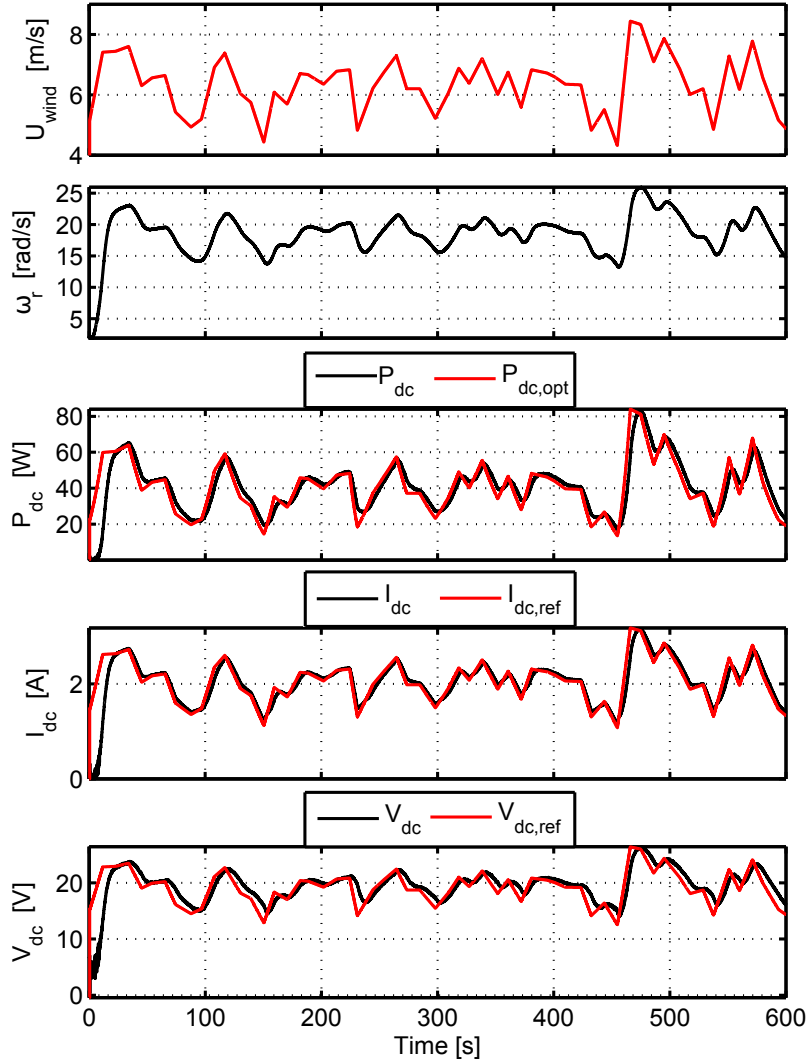


Figure 6.12: HIL simulation results for the realistic wind velocity. Note that the wind velocity starts from 0 m/s .

profile and out-performance of the simple non-linear control is considered, it can be concluded that it is the best result obtained so far among the control methods and wind profiles.

6.3 Comparison of the control methods

In this subsection, the total obtained energy outputs of both control methods are compared. The power trajectory of the both methods around the optimum power are able to distinguished better on the same figure. The results are depicted in Figure 6.13. The left hand side plots are same as the plots given in Figures 6.4 - 6.6 and 6.10 - 6.12. Energy outputs were calculated over each HIL simulation with the step, sinusoidal and realistic wind velocities, and they are also depicted with respect to time at the right-hand side of Figure 6.13. Further, they are listed in Table 6.4

and a comparison factor was introduced as the ratio of the total calculated energies, i.e MPPT to SNC, for the each wind type.

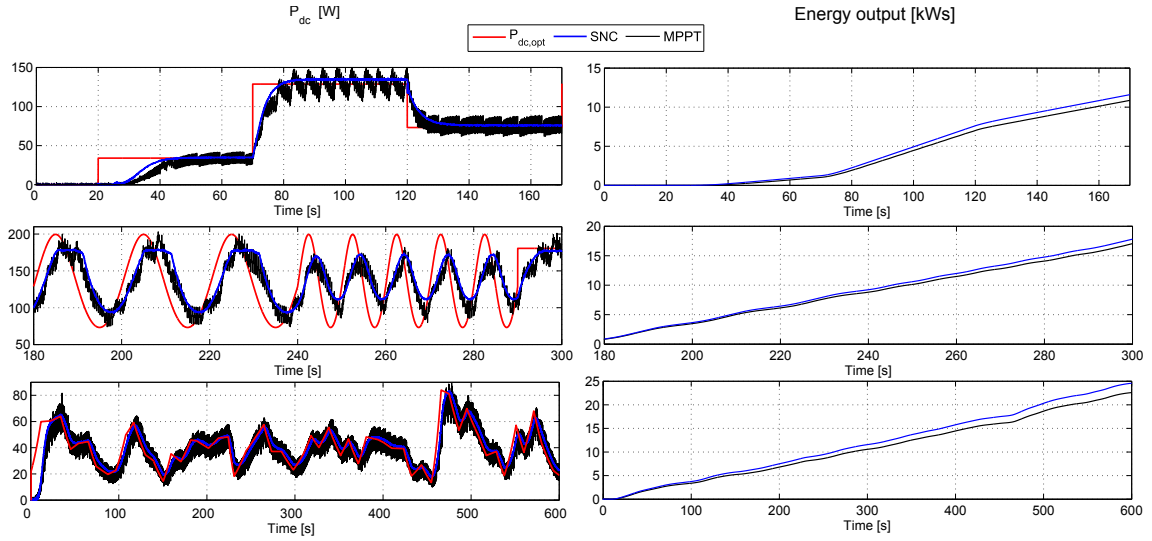


Figure 6.13: Comparison of the MPPT and simple non-linear control (snc) results. The output power the step, sinusoidal and realistic wind profile are at the left-hand side from top to bottom respectively. The corresponding energy outputs are at the right side of each plot.

Wind profile	Total energy kJ		Comparison factor $\frac{MPPT}{SNC}$
	MPPT	SNC	
Step up-down	10.869	11.599	0.94
Sinusoidal	17.047	17.807	0.96
Realistic	22.597	24.584	0.92

Table 6.4: The total obtained energy output for step up and down, sinusoidal and realistic wind profile.

According to Figure 6.13 and Table 6.4, the SNC outruns the MPPT especially for the realistic wind characteristic. MPPT applied VAWT system power output inconveniently oscillates around the optimum power point. Notwithstanding this, the SNC applied VAWT system output power has no oscillation. Besides the disadvantageous effects of the power oscillations on the total obtained energy output, it also introduces harmonic components in the micro-grid current and decreases the power quality. In this study, the VAWT system modeled with only a dc load, however micro-grid inclusive VAWT systems are widely used especially in distributed power generation system, and the oscillating power characteristic naturally reflects in ac side, i.e in grid current, and increases THD [54], [56]. Moreover, oscillations also cause mechanical vibrations in the rotor and this can reduce the life span and downtime of the mechanical components.

6.4 Effects of the generator parameters on the performance

Writing a separate discussion section concerning the generator parameters found to be necessary because of the importance of its effect on the system efficiency. The discussion starts with the following question:

- What if the generator parameters such as torque constant, back-emf constant or pole numbers could be changed?

Before starting the discussion, the PMSG-rectifier structure was considered even simpler, i.e a dc machine model that only have a line resistance which is presented in Figure 6.14. Furthermore, the electrical variables coupled with mechanical ones are included in Figure 6.14. For the equations refer to Table 3.4 and 4.5. According

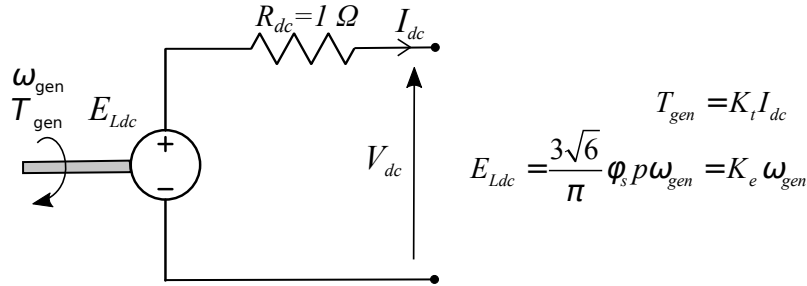


Figure 6.14: Simplified dc model with neglected phase inductance in generator, diode overlapping currents and threshold voltage in rectifier. Only the phase resistance is included.

to [36], the torque constant (K_t) and back-emf constant (K_e) are equal in metric unit system and constant. If the model introduced in Figure 6.14 is used and power output is calculated for 8 m/s wind speed, the results in Figure 6.15 are obtained. As it can be seen from Figure 6.15, the wind torque is relatively high at the low operation speed region. Since the rotor speed is constant in steady state and $T_{gen} = T_{wind}$, dc current can be calculated by using the torque constant ($I_{dc} = \frac{T_{gen}}{K_t}$). Consequently, high operating torque can result in drawing high current through the generator. Copper losses are proportional to the square of current drawn, i.e $P_{loss,Cu} = I_{dc}^2 R_{dc}$. If a generator with the same power and line resistance but with doubled back-emf constant, in other words a generator with higher rated voltage and thereby a lower rated current, is employed, copper losses decrease and thus higher useful power is generated. This behavior is depicted also in Figure 6.15 by doubling the value of K_e . Notice the decrease and increase in I_{dc} and P_{dc} given with dashed lines in Figure 6.15.

Additional to this analysis, in the same manner, the flux parameter and torque constant values that are used for the simplified dc model of the PMSG-rectifier used

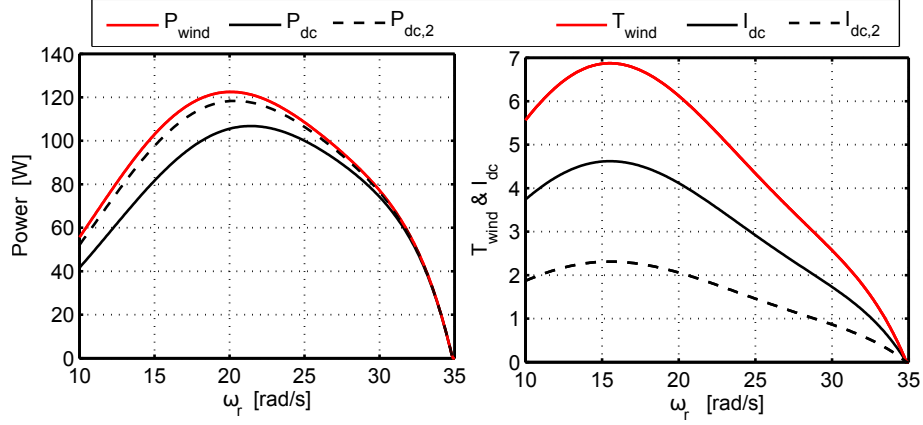


Figure 6.15: The wind power and torque, dc power and current of the VAWT system with only R_{dc} regarded dc model for 8 m/s wind speed. The left hand side plots represent the wind power (P_{wind}), output power under normal condition (P_{dc}) and when the back-emf constant is doubled ($P_{dc,2}$). The right hand side plots represent the wind torque (P_{win}), dc current under normal condition (I_{dc}) and when the back-emf constant is doubled ($I_{dc,2}$).

in the HIL simulation can be manipulated. Imagine a generator with the same rated power, rated speed, line resistance and inductance but doubled rated voltage, i.e flux ϕ_s is doubled. The wind power is the same for 8 m/s wind speed, but output power would be different than the one previously depicted in Figure 5.3. Figure 6.16 shows the wind power (P_{wind}), output power under normal condition (P_{dc}) and when the flux is doubled ($P_{dc,2}$) for 8 m/s wind speed.

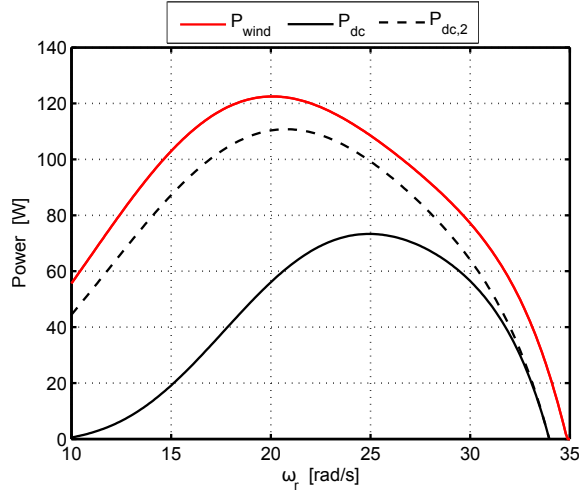


Figure 6.16: The wind power (P_{wind}), output power under normal condition (P_{dc}) and when the back-emf constant is doubled ($P_{dc,2}$).

In Figure 6.16, P_{dc} is 73.3 W, whereas $P_{dc,2}$ is 110.8 W. There is an 51.2 % increase in the output power since the current drawn from the generator is decreased as well as the resistive losses. Now the question is:

- Does the higher rated voltage design generator always result less loss in the system?

Even though it is obvious that the system needs a generator with less rated current which results in less copper losses, it is not enough to conclude in an absolute judgment, because many factors in the simplified dc model, especially the iron losses, are disregarded. An overview of the iron loss models are presented in [57]. In electrical machines, the variation of magnetic flux density in stator core causes eddy current and hysteresis loss. The eddy current occurs and flows in the stator iron due to the variations of the magnetic flux over time. The hysteresis loss take a place due to the magnetization of the iron differs from the demagnetization, and consequently the stator iron laminations lose energy equal to the surface area of the hysteresis loop in each cycle. Both the eddy and hysteresis losses are dissipated as a heat. Lastly, the excess losses model is used to model the losses that are not caused by hysteresis and eddy currents. As a summary, the iron loss model is separated into three loss types and it is actually an empirical approach, endeavouring to relate the different physical effects due to flux density and its frequency in electromagnetic design [57], [58]. Thus, a more detailed study needs to be done to analyse different generators which has various rated voltages but same power. The generator design procedure examples for wind turbines can be find in [58] ,[59] and for low speed direct drive application in [60].

6.4.1 Ideal generator parameters

A generator with less line resistance and inductance value yields less voltage drops. Moreover, a generator designed with higher stator diameter and thinner stator iron lamination has less iron losses compared to the one used in the VAWT simulator. Furthermore, the rate of heat transfer through the PMSG surface can be increased by increasing the outer diameter of the stator, and it is in behalf of the magnets and copper wires since the high temperature can demagnetize the magnets and damage the copper insulation. As a result, a bulky and oversize generator, of course, would result in a better performance in terms of power loss and cooling. However, the discussion in Section 6.4 does not approach the topic in this respect, instead, it will try to answer:

- Which parameters are of interest while selecting the right generator for the designed VAWT?
- What are the initial parameters that can be looked for a candidate generator that is employed in the VAWT system.

Average losses for 6 different generators which are designed for 50 kW direct driven vertical axis wind turbine and have different rated voltage but same power level are evaluated and generators are compared in [59], and varied parameters of these 6 generators are quoted from [59] and listed in Table 6.5. Moreover, average losses and losses at rated voltage for these 6 generators are represented in Figure 6.17 with respect to their rated voltage.

Characteristics	Generator no					
	1	2	3	4	5	6
Line voltage (V) RMS	134	200	286	334	400	800
Current (A) RMS	215.4	144.3	100.9	86.4	72.2	36.1
Rotational speed (r/min)	66	64.61	63.75	63.52	63	64.13
Number of poles	20	26	32	34	40	58
Stator inner diameter (mm)	910	1010	1060	1090	1150	1300
Stator outer diameter (mm)	1106	1176	1206	1228	1277	1402
Generator length (mm)	343	358	393	412	410	487
Total weight (kg)	1177	1088	1039	1057	986	960

Table 6.5: Varied parameters of 6 different generator design [59]

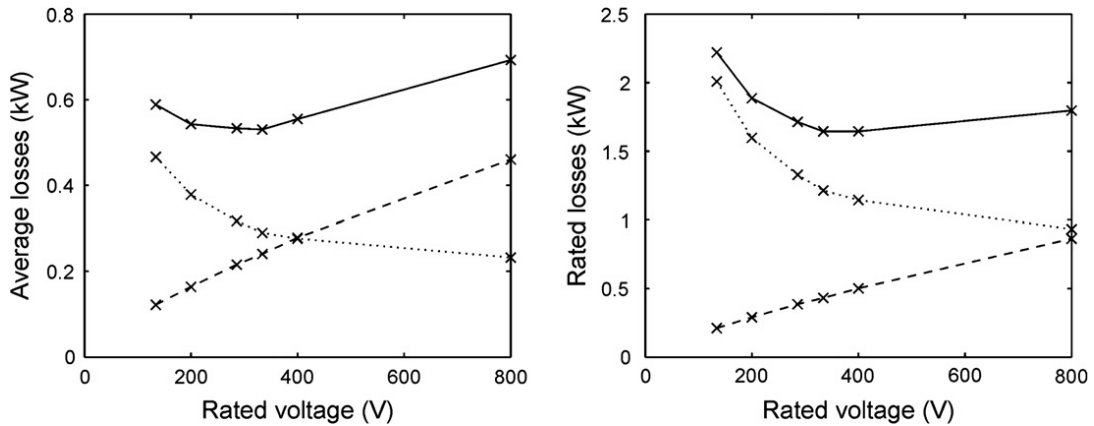


Figure 6.17: Average losses and losses at the rated power are at the left and right hand sides of the figure respectively. The solid lines represent the total losses, the dashed lines represents the iron losses and the dotted lines represents the copper losses [59].

According to Figure 6.17, the iron losses almost rise linearly with the rated voltage. Besides, the copper losses attain relatively low values for a higher rated voltage. In Figure 6.17 taken from [59], both average losses and losses at rated conditions are depicted to evaluate the contribution of the loss type (iron and copper) in total power loss from different perspectives. See the distribution of the losses under the rated power conditions; most of the losses are contributed by the copper losses. However, the contribution of the iron losses appears much higher in average the loss evaluation since the generator does not always operate at rated torque and speed value, but often in partial loads.

Other notable parameters of the generators in Table 6.5 are the number of poles, size and the total weight. As the rated voltage increase, the size of the generator increase. However, the total weight becomes lighter. This is due to an increase on the number of poles and this phenomenon is explained well in [60]; indeed, the less active weighed designs can be achieved for the same required nominal torque level by designs with high number of poles. See Figure 6.18, the flux density in the air-gap of the both machines are equivalent but the flux from one pole to the other are lower. This situation enables to design the stator with thinner yoke and teeth size without any risk of the iron saturation since the flux is diminished with a higher pole number design. In [61], the weight reduction is considered as the most important advantage and reason for preference of designs with high pole numbers.

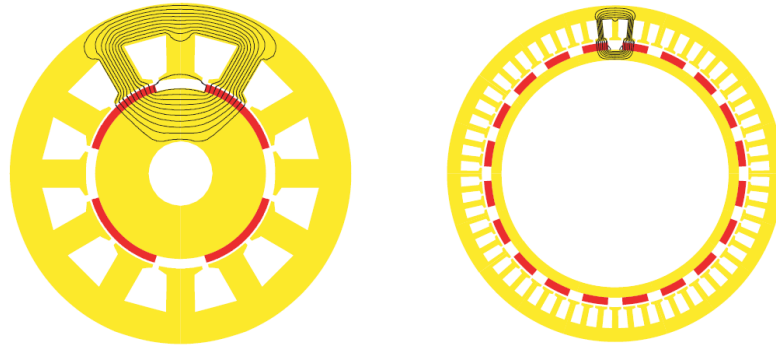


Figure 6.18: 4-pole PM machine (left) and 20-poe PM machine (right) [60]

As a conclusion, higher number of poles and hence higher size but lower active weight of generator which operates in low-speed with relatively high output voltage would result better performance in the studied VAWT system. In the following subsection, sample generators found in the market with such parameters aforementioned above are presented and a benchmark results.

6.4.2 Performance comparison

For the performance comparison, candidate generators were researched to compare with the studied VAWT system ratings. The power ratings of the cited and previously mentioned works are relatively high compared to the studied VAWT system. As a summary, the designed or used generators are 12 kW in [58] and [62], 20 kW in [63], 50 kW in [59] and 225 kW in [64]. Besides these, the on-line documentation of the direct drive generators, torque generators, PMSG and so on were searched from manufacturers web-page. The most suitable ones for a comparison are selected: Alxion STK Wind and Water Turbines Alternators, 145STK2M [65]. Their characteristics such as torque, speed, efficiency, phase RMS current, line to line RMS voltage at rated power, phase resistance, inductance, rotor inertia, cable diameter

are given in its data-sheet [66]. Furthermore, operating power, voltage, torque and efficiency curves with respect to the speed are given in [67]. In the technical manual of 145STK2M generator, specifications are given for two different rated speeds as they are listed in Table 6.6.

Alxion Generator Parameters	145STK2M	
	Alxion-1	Alxion-2
Rated speed [rpm]	650	1500
Rated power [W]	571	1752
Input torque at rated speed [Nm]	11.2	13.9
Efficiency at rated power	75	81
Current at rated power [A]	1.4	4.3
Voltage at no load (back emf) [V]	365	393
Phase resistance [Omega]	19.8	4.53
Phase inductance [mH]	105	24
Number of pole pairs	6	6

Table 6.6: Alxion generator, 145STK2M parameters [66].

The simplified dc model requires 6 parameters to estimate the voltage drops on the PMSG-rectifier structure; which are the phase resistance, inductance, number of pole pairs, diode threshold voltage, back-emf constant and torque constant. To be able to compare the performance of the Alxion generators with the present one by using the developed simple dc model, values such as torque constant (K_t), back-emf constant (K_e) are calculated from the parameters given in Table 6.6 and listed in Table 6.7 with the parameters of the present generator used in the VAWT simulator.

Generator parameters		Generators		
		Alxion-1	Alxion-2	Present one
Back-emf constant	$K_e = \frac{V_{dc}}{\omega_{gen}}$ [V s/rad]	7.24	3.14	1.49
Torque constant	$K_t = \frac{T_{gen}}{I_{dc}}$ [Nm/A]	6.23	2.52	1.31
Phase resistance	R_s [Ω]	19.8	4.53	1.6
Phase inductance	L_s [mH]	105	24	4.6
Number of poles	p	6	6	6

Table 6.7: Transformed Alxion parameters and present generator parameters that are used in the simplified dc model for performance comparison. (For transformation details, see Table 4.5 and 3.4).

According to Table 6.7, it can be seen that both Alxion generators have higher back-emf constants. Especially Axion-1 has relatively high back-emf and torque constant which means the VAWT can be loaded by drawing relatively low current. However, Alxion-1's phase resistance is the highest one. Previously calculated wind and output dc power for 8 m/s wind speed is calculated by using Alxion-1 and 2 parameters. Results are depicted in Figure 6.19.

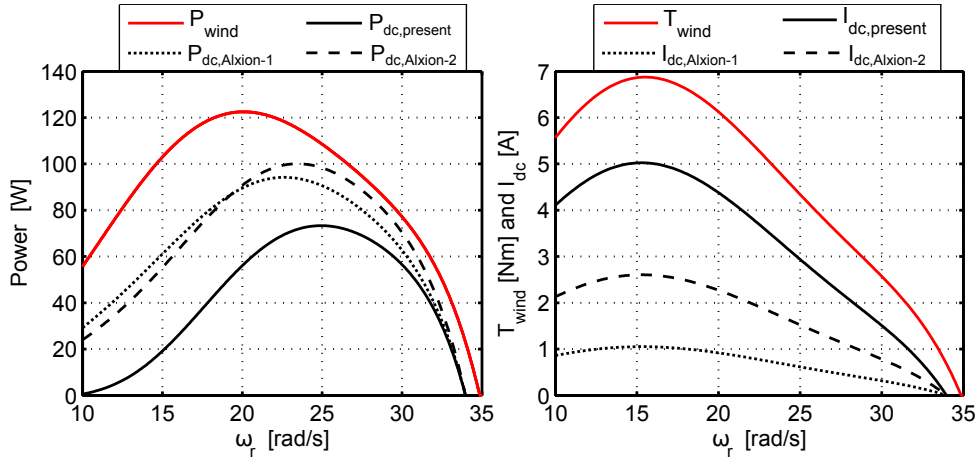


Figure 6.19: The wind power and torque, dc power and current of the VAWT system with the parameters of present, Alxion-1 and Alxion-2 generators.

According to Figure 6.19, the same amount of torque can be generated with much smaller currents, when the present generator is replaced either with Alxion-1 or Alxion-2. Amongst the three generators compared in Table 6.7, Alxion-1 requires the least amount of current to deliver the same torque, which suggests that Alxion-1 would suffer less from resistive losses, that are scaled with the square of the current, and thus deliver a greater power output. However, when the power outputs are compared, it is observed that Alxion-2 manages to catch up with Alxion-1 thanks to its much lower phase resistance, which is around one quarter of the resistance listed for Alxion-2 and hence sufficiently low to compensate for the double amount of current drawn. Peak power outputs achieved by the present generator, Alxion-1 and Alxion-2 are 73.3, 95.25 and 102.53 Watts respectively.

Theoretically, the higher area of the copper, the less resistance. In other words, the equivalent phase resistance of the wires filling the slots in the stator can be decreased by increasing the slot areas, i.e the outer diameter of the stator, for the resistance is inversely proportional to the copper area. The relatively high resistance value of Alxion-1 can be decreased by this approach, and a low resistance-high torque constant generator can be designed as an ideal generator candidate. Due to the decrease in the resistance, the system suffers less amount of copper losses. Contribution of the increased area to the system further manifests in the dissipation of this lost energy from the surface in form of heat, since the conductive heat transfer rate is scaled with the surface area. However, the disadvantages of such generators are being larger than the conventional ones and being hard to obtain since the electrical machines tend to be designed for achieving higher speeds and having smaller dimensions. However, the weight and size of the generator are of less interests in VAWT applications since they can site on the ground in VAWT systems. As a conclusion, the generator needs to be optimized considering the efficiency in

the operation region of the VAWT, instead of aiming to dis-burden the weight or minimizing the size. This way, a VAWT design that operates with high torque does not suffer from high amount of the loss. However, the generator can be costly.

Alternatively, the VAWT design can be changed in order to attain the maximum value of the power coefficient (C_p) at higher tip-speed ratio(λ). This means that increasing the optimum value of the tip-speed ratio elevates the optimum operation speed since $\lambda = \frac{\omega_r R}{U_{wind}}$, and higher the rotor speeds result in lower the torques for a certain amount of power. Eventually, a cheaper conventional generator could be selected for the VAWT system. In wind turbines, the torque on the rotor is proportional to the solidity that is described in [1], and it is the ratio of the blade area to the swept area. Especially in VAWTs, high solidity leads to attaining a C_p curve in relatively low tip-speed ratio regions (See Figure 1.3). According to [1], designs of lower solidity are favored for their economical advantages. Moreover, according to [68], high solidity designs are used in such applications where high torque and low speed are needed; for example water pumping. On the other hand, for electrical power production applications, low solidity designs that are operated at low torques are preferred.

Chapter 7

Conclusion and future works

In this thesis, a framework was developed to carry out hardware-in-the-loop simulations for a small scale VAWT that is suitable to be used in rural areas. The VAWT dynamics are mimicked and its inertia is emulated by a proposed method in Section 4.4. In the VAWT simulator, the deviations from the PMSG torque constant, estimated friction torque and all other external effects are treated as disturbance torques, and they are compensated for.

For the compensation torque generation, the friction torque is estimated by a curve fitted polynomial that was previously acquired from the experimental data. The PMSG torque constant is also estimated from a curve fitted linear function from previously acquired experimental data. The polynomial for the friction calculation and the torque constant are used in the model based feed-forward control. A virtual model is introduced to obtain an error between the actual and virtual-plant speeds. This error is used to generate a disturbance compensation torque by a PI controller. In other words, the PI controller handles the deviations of the estimated generator torque, friction torque and the external disturbance torques. With the proposed method, the VAWT simulator is capable of emulating the VAWT rotor inertia. This method can also be used in servomechanisms utilized in industrial applications, where there are uncertain effects of the inertia, friction and loads, e.g Computer-numerical-control (CNC) machine applications.

The same framework was used to specify the PMSG characteristics over a wide range of the speed and torque, since the data supplied by the manufacturer contains just the nominal power and speed.

A communication protocol was implemented to communicate with the electronic load to draw a current at desired value. By this way, the torque of the PMSG is controlled.

After ensuring that the VAWT simulator is successfully able to mimic the dynamics of the VAWT, control designs were implemented and tested. Firstly, a parametric study was carried out to tune the MPPT algorithm variables. In order to realize the

maximum output power value which is less than the aerodynamic power due to the friction losses and the losses of PMSG-rectifier structure, a simplified dc model is used to estimate the voltage drops and calculate the output power for steady state. The same simplified dc model is used to estimate the optimal voltage and current values for wind speeds varying between 0 and 14 m/s. These optimal values are used as reference values in the SNC algorithm. The SNC algorithm variables were also tuned by making a parametric study. Both control methods result in following the optimum power point trajectory well. The SNC outperforms the MPPT results in terms of the energy and convergence speed. Moreover, the SNC method does not cause oscillations at the output power which are observed when the MPPT is applied in the HILS. The oscillations at the dc power give rise to distortions in the current of the micro-grid. Therefore, the SNC method would be preferred for high efficiency, less oscillations and smooth power. On the other hand, the MPPT performance can be improved by applying adaptive iterations in order to accelerate the convergence speed and mitigate the oscillations around the optimum power. The MPPT outperforms the SNC method in terms of reliability since the SNC performance is strongly related with the acquired data from the anemometer. Furthermore, for the SNC, a misestimation of the VAWT system characteristics causes under-performance in efficiency and oscillatory power. As a result, the MPPT method can be preferred if the VAWT characteristics are unknown and mechanical sensor-less control is desired; the SNC method can be preferred if the system characteristics are well known, wind speed is measurable with high accuracy and efficient-smooth power output is desired.

The passive rectification creates non-sinusoidal waveforms which increase the THD, and the harmonic components cause additional losses which are dissipated in form of heat and reduce the PMSG efficiency. However, 3-phase diode-rectifiers are robust and cheap. Moreover, they do not need to be controlled. These advantages make the use of diode rectifiers suitable especially for the small-scale WECS in rural areas where high reliability and downtime are demanded.

The PMSG parameters strongly influence the system efficiency, and its operating region needs to agree well with the designed VAWT for high efficiency output power. H-rotor darrieus type VAWTs have high solidity, and hence they operate in high-torque and low-speed regions. A discussion was made for suitable generator parameters, and it is concluded that a PMSG with high pole numbers, torque constant and large diameter is applicable for the VAWT used in this study.

As future work, the following things can be done:

- Active rectification can be done to mitigate the harmonic content in the PMSG current and voltage waveforms.

- The presented MPPT algorithm can be improved. Adaptive iteration based MPPT algorithm can be developed to decrease the oscillations around optimum power. Moreover, the response time of the system under sudden changes of the wind can be decreased with adaptive iterations.
- The presented SNC algorithm can be improved in such a way that the upper and lower voltage boundaries can be updated during the operation for each wind speed. To this end, an accurate model of the overall system (including the complex electromechanical model with the transient effects, and noises) needs to be developed to be able to run an optimization simulation that determines the optimum boundaries for the maximum energy output.
- Further control methods such as model predictive control can be applied in the VAWT simulator, and their performances can be compared with the MPPT and SNC.
- A suitable PMSG can be selected based on the discussion presented in Section 6.4 from the market, or it can be designed and manufactured.
- A dc/dc converter, a battery charger unit and an inverter can be designed to be implemented in the VAWT system. The designs can be tested in the VAWT simulator.
- A performance-cost optimization can be done by evaluating the performance and solidity of the VAWT rotor since the less torque allows finding a cheaper PMSG design widely available in the market, and decreases the overall cost of the system. However, changing the VAWT design can cause a decrease in the aerodynamic efficiency. This performance and cost changes can be investigated in detail to propose the highest ratio of *energy/cost*.

Bibliography

- [1] A. V. Da Rosa, *Fundamentals of renewable energy processes*. Academic Press, 2012.
- [2] E. Hau and H. von Renouard, *Wind Turbines: Fundamentals, Technologies, Application, Economics*. SpringerLink : Bücher, Springer Berlin Heidelberg, 2013.
- [3] C. Kost, J. Mayer, J. Thomsen, N. Hartmann, C. Senkpiel, S. Philipps, S. Nold, S. Lude, N. Saad, and T. Schlegl, “Levelized cost of electricity renewable energy technologies,” *Fraunhofer Institute for Solar Energy Systems ISE*, 2013.
- [4] M. R. Patel, *Wind and solar power systems: design, analysis, and operation*. CRC press, 2005.
- [5] R. E. Wilson and P. B. Lissaman, “Applied aerodynamics of wind power machines,” tech. rep., Oregon State Univ., Corvallis (USA), 1974.
- [6] H. Riegler, “Hawt versus vawt: Small vawts find a clear niche,” *Refocus*, vol. 4, no. 4, pp. 44–46, 2003.
- [7] S. Eriksson, H. Bernhoff, and M. Leijon, “Evaluation of different turbine concepts for wind power,” *Renewable and Sustainable Energy Reviews*, vol. 12, no. 5, pp. 1419–1434, 2008.
- [8] M. Bacic, “On hardware-in-the-loop simulation,” in *Decision and Control, 2005 and 2005 European Control Conference. CDC-ECC’05. 44th IEEE Conference on*, pp. 3194–3198, IEEE, 2005.
- [9] R. Isermann, J. Schaffnit, and S. Sinsel, “Hardware-in-the-loop simulation for the design and testing of engine-control systems,” *Control Engineering Practice*, vol. 7, no. 5, pp. 643–653, 1999.
- [10] D. J. Kempf, L. S. Bonderson, and L. I. Slafer, “Real time simulation for application to abs development,” tech. rep., SAE Technical Paper, 1987.

- [11] J. S. Cole Jr and A. C. Jolly, “Hardware-in-the-loop simulation at the us army missile command,” in *Technologies for Synthetic Environments: Hardware-in-the-Loop Testing*, vol. 2741, pp. 14–19, 1996.
- [12] H. Eguchi and T. Yamashita, “Benefits of hwil simulation to develop guidance and control systems for missiles,” in *AeroSense 2000*, pp. 66–73, International Society for Optics and Photonics, 2000.
- [13] M. B. Evans and L. J. Schilling, *The role of simulation in the development and flight test of the HiMAT vehicle*. National Aeronautics and Space Administration, Ames Research Center, Dryden Flight Research Facility, 1984.
- [14] A. Bouscayrol, “Different types of hardware-in-the-loop simulation for electric drives,” in *Industrial Electronics, 2008. ISIE 2008. IEEE International Symposium on*, pp. 2146–2151, IEEE, 2008.
- [15] B. Lu, A. Monti, R. Dougal, *et al.*, “Real-time hardware-in-the-loop testing during design of power electronics controls,” in *Industrial Electronics Society, 2003. IECON’03. The 29th Annual Conference of the IEEE*, vol. 2, pp. 1840–1845, IEEE, 2003.
- [16] M. Steurer, F. Bogdan, W. Ren, M. Sloderbeck, and S. Woodruff, “Controller and power hardware-in-loop methods for accelerating renewable energy integration,” in *Power Engineering Society General Meeting, 2007. IEEE*, pp. 1–4, IEEE, 2007.
- [17] T. Hardy and W. Jewell, “Hardware-in-the-loop wind turbine simulation platform for a laboratory feeder model,” *Sustainable Energy, IEEE Transactions on*, vol. 5, no. 3, pp. 1003–1009, 2014.
- [18] B. Neammanee, S. Sirisumrannukul, and S. Chatratana, “Development of a wind turbine simulator for wind generator testing,” *International Energy Journal*, vol. 8, no. 1, pp. 21–28, 2007.
- [19] N. Muntean, L. Tutelea, D. Petrila, and O. Pelan, “Hardware in the loop wind turbine emulator,” in *Electrical Machines and Power Electronics and 2011 Electromotion Joint Conference (ACEMP), 2011 International Aegean Conference on*, pp. 53–58, IEEE, 2011.
- [20] H. Li, M. Steurer, K. Shi, S. Woodruff, and D. Zhang, “Development of a unified design, test, and research platform for wind energy systems based on hardware-in-the-loop real-time simulation,” *Industrial Electronics, IEEE Transactions on*, vol. 53, no. 4, pp. 1144–1151, 2006.

- [21] S.-H. SOng, B.-C. Jeong, H.-I. Lee, J.-J. Kim, J.-H. Oh, and G. Venkataraman, “Emulation of output characteristics of rotor blades using a hardware-in-loop wind turbine simulator,” in *Applied Power Electronics Conference and Exposition, 2005. APEC 2005. Twentieth Annual IEEE*, vol. 3, pp. 1791–1796, IEEE, 2005.
- [22] I. Munteanu, A. I. Bratcu, S. Bacha, D. Roye, and J. Guiraud, “Hardware-in-the-loop-based simulator for a class of variable-speed wind energy conversion systems: Design and performance assessment,” *Energy Conversion, IEEE Transactions on*, vol. 25, no. 2, pp. 564–576, 2010.
- [23] I. Munteanu, A. I. Bratcu, N.-A. Cutululis, and E. Ceanga, *Optimal control of wind energy systems: towards a global approach*. Springer Science & Business Media, 2008.
- [24] F. D. Bianchi, H. De Battista, and R. J. Mantz, *Wind turbine control systems: principles, modelling and gain scheduling design*. Springer Science & Business Media, 2006.
- [25] Y. Xia, K. H. Ahmed, and B. W. Williams, “A new maximum power point tracking technique for permanent magnet synchronous generator based wind energy conversion system,” *Power Electronics, IEEE Transactions on*, vol. 26, no. 12, pp. 3609–3620, 2011.
- [26] R. Kot, M. Rolak, and M. Malinowski, “Comparison of maximum peak power tracking algorithms for a small wind turbine,” *Mathematics and Computers in Simulation*, vol. 91, pp. 29–40, 2013.
- [27] A. M. De Broe, S. Drouilhet, and V. Gevorgian, “A peak power tracker for small wind turbines in battery charging applications,” *Energy conversion, iee transactions on*, vol. 14, no. 4, pp. 1630–1635, 1999.
- [28] M. Singh and A. Chandra, “Power maximization and voltage sag/swell ride-through capability of pmsg based variable speed wind energy conversion system,” in *Industrial Electronics, 2008. IECON 2008. 34th Annual Conference of IEEE*, pp. 2206–2211, IEEE, 2008.
- [29] R. Esmaili, L. Xu, and D. Nichols, “A new control method of permanent magnet generator for maximum power tracking in wind turbine application,” in *Power Engineering Society General Meeting, 2005. IEEE*, pp. 2090–2095, IEEE, 2005.
- [30] M. Drugă, C. Nichita, G. Barakat, B. Dakyo, and E. Ceangă, “A peak power tracking wind system operating with a controlled load structure for stand-alone

- applications,” in *Power Electronics and Applications, 2009. EPE'09. 13th European Conference on*, pp. 1–9, IEEE, 2009.
- [31] S. Chun and A. Kwasinski, “Analysis of classical root-finding methods applied to digital maximum power point tracking for sustainable photovoltaic energy generation,” *Power Electronics, IEEE Transactions on*, vol. 26, no. 12, pp. 3730–3743, 2011.
- [32] S. H. Hosseini, A. Farakhor, and S. K. Haghghian, “Novel algorithm of maximum power point tracking (mppt) for variable speed pmsg wind generation systems through model predictive control,” in *Electrical and Electronics Engineering (ELECO), 2013 8th International Conference on*, pp. 243–247, IEEE, 2013.
- [33] K.-Y. Lo, Y.-M. Chen, and Y.-R. Chang, “Mppt battery charger for stand-alone wind power system,” *Power Electronics, IEEE Transactions on*, vol. 26, no. 6, pp. 1631–1638, 2011.
- [34] M. Narayana, G. Putrus, M. Jovanovic, P. S. Leung, and S. McDonald, “Generic maximum power point tracking controller for small-scale wind turbines,” *Renewable Energy*, vol. 44, pp. 72–79, 2012.
- [35] “Ruzgar enerji potansiyel atlası.”
- [36] D. Lin, P. Zhou, and Z. Cendes, “In-depth study of the torque constant for permanent-magnet machines,” *Magnetics, IEEE Transactions on*, vol. 45, no. 12, pp. 5383–5387, 2009.
- [37] N. Mohan and T. M. Undeland, *Power electronics: converters, applications, and design*. John Wiley & Sons, 2007.
- [38] C. Alexander and M. Sadiku, *Fundamentals of Electric Circuits*. McGraw-Hill Higher Education, 2007.
- [39] T. Wildi, *Electrical Machines, Drives and Power Systems: Pearson New International Edition*. Pearson Education Limited, 2013.
- [40] H. Rashid, *Power Electronics: Circuits, Devices, and Applications*. Pearson/Prentice Hall, 2004.
- [41] T. M. H. Nicky, K. Tan, and S. Islam, “Mitigation of harmonics in wind turbine driven variable speed permanent magnet synchronous generators,” in *Power Engineering Conference, 2005. IPEC 2005. The 7th International*, pp. 1159–1164, IEEE, 2005.

- [42] S. Hansen, L. Asiminoaei, and F. Blaabjerg, “Simple and advanced methods for calculating six-pulse diode rectifier line-side harmonics,” in *Industry Applications Conference, 2003. 38th IAS Annual Meeting. Conference Record of the*, vol. 3, pp. 2056–2062, IEEE, 2003.
- [43] A. Urtasun, P. Sanchis, I. San Martín, J. López, and L. Marroyo, “Modeling of small wind turbines based on pmsg with diode bridge for sensorless maximum power tracking,” *Renewable energy*, vol. 55, pp. 138–149, 2013.
- [44] F. D. Adegas, J. A. V. Alé, F. S. dos Reis, G. C. da Silva Simioni, and R. Tonkoski, “Maximum power point tracker for small wind turbines including harmonic mitigation,” in *2006 European Wind Energy Conference and Exhibition*, pp. 1–10, 2006.
- [45] B. Sareni, A. Abdelli, X. Roboam, and D.-H. Tran, “Model simplification and optimization of a passive wind turbine generator,” *Renewable Energy*, vol. 34, no. 12, pp. 2640–2650, 2009.
- [46] D.-H. Tran, B. Sareni, X. Roboam, and C. Espanet, “Integrated optimal design of a passive wind turbine system: an experimental validation,” *Sustainable Energy, IEEE Transactions on*, vol. 1, no. 1, pp. 48–56, 2010.
- [47] *IXYs VUO160-12NO7 Datasheet*.
- [48] *USER’S GUIDE Adilent Technologies DC Electronic Loads Models N3300A-N3307A*.
- [49] M.-C. Tsai, I.-F. Chiu, and M.-Y. Cheng, “Design and implementation of command and friction feedforward control for cnc motion controllers,” in *Control Theory and Applications, IEE Proceedings-*, vol. 151, pp. 13–20, IET, 2004.
- [50] D. Stajić, N. Perić, and J. Deur, “Friction compensation methods in position and speed control systems,” in *Industrial Electronics, 1999. ISIE’99. Proceedings of the IEEE International Symposium on*, vol. 3, pp. 1261–1266, IEEE, 1999.
- [51] C. O. Saglam, E. Baran, A. O. Nergiz, A. Sabanovic, *et al.*, “Model following control with discrete time smc for time-delayed bilateral control systems,” in *Mechatronics (ICM), 2011 IEEE International Conference on*, pp. 997–1002, IEEE, 2011.
- [52] J.-C. Wu, K.-H. Su, and M.-Y. Cheng, “Friction and disturbance compensation for speed control of servo control systems,” in *IECON 2010-36th Annual Conference on IEEE Industrial Electronics Society*, pp. 1890–1895, IEEE, 2010.

- [53] A. O. O. S. Y. A. Sinlak, C. Kaleli, “Simple control design for a small vertical axis wind turbine,” in *Accepted to Otomatik Kontrol Türk Milli Komitesi Ulusal Toplantısı*, TOK, 2015.
- [54] L. Belhadji, S. Bacha, I. Munteanu, A. Rumeau, and D. Roye, “Adaptive mppt applied to variable-speed microhydropower plant,” *Energy Conversion, IEEE Transactions on*, vol. 28, no. 1, pp. 34–43, 2013.
- [55] E. Koutroulis and K. Kalaitzakis, “Design of a maximum power tracking system for wind-energy-conversion applications,” *Industrial Electronics, IEEE Transactions on*, vol. 53, no. 2, pp. 486–494, 2006.
- [56] A. Darwish, A. Abdelsalam, A. M. Massoud, and S. Ahmed, “Single phase grid connected current source inverter: Mitigation of oscillating power effect on the grid current,” in *Renewable Power Generation (RPG 2011), IET Conference on*, pp. 1–7, IET, 2011.
- [57] A. Krings and J. Soulard, “Overview and comparison of iron loss models for electrical machines,” in *5th International Conference and Exhibition on Ecological Vehicles and Renewable Energies (EVER 10), Monte-Carlo, MONACO, MAR 25-28, 2010*, 2010.
- [58] F. Bülow, “A generator perspective on vertical axis wind turbines,” 2013.
- [59] S. Eriksson and H. Bernhoff, “Loss evaluation and design optimisation for direct driven permanent magnet synchronous generators for wind power,” *Applied Energy*, vol. 88, no. 1, pp. 265–271, 2011.
- [60] F. Meier, “Permanent-magnet synchronous machines with non-overlapping concentrated windings for low-speed direct-drive applications,” 2008.
- [61] E. Moe and P. Midford, *The Political Economy of Renewable Energy and Energy Security: Common Challenges and National Responses in Japan, China and Northern Europe*. Energy, Climate and the Environment, Palgrave Macmillan, 2014.
- [62] N. Madani, “Design of a permanent magnet synchronous generator for a vertical axis wind turbine,” 2011.
- [63] W. Wu, V. Ramsden, T. Crawford, and G. Hill, “A low speed, high-torque, direct-drive permanent magnet generator for wind turbines,” in *Industry Applications Conference, 2000. Conference Record of the 2000 IEEE*, vol. 1, pp. 147–154, IEEE, 2000.

- [64] S. Eriksson, H. Bernhoff, and M. Leijon, “A 225 kw direct driven pm generator adapted to a vertical axis wind turbine,” *Advances in Power Electronics*, vol. 2011, 2011.
- [65] “Alxion, stk wind and water turbines alternators, url: <http://www.alxion.com/products/stk-alternators/>.”
- [66] *Technical characteristics ALXION 145 STK alternator* , url: <http://www.alxion.com/wp-content/uploads/2011/10/82.pdf>.
- [67] “Technical characteristics alxion 145 stk alternator, operating curves, url: <http://www.alxion.com/wp-content/uploads/2011/10/145atk2m.pdf>.”
- [68] R. Howell, N. Qin, J. Edwards, and N. Durrani, “Wind tunnel and numerical study of a small vertical axis wind turbine,” *Renewable energy*, vol. 35, no. 2, pp. 412–422, 2010.